THE DESIGN AND TESTING OF A POWER AUGMENTED WIND TURBINE SYSTEM FOR URBAN HIGH RISE APPLICATION

PAN KOK CHEN

FACULTY OF ENGINEERING

UNIVERSITY OF MALAYA

KUALA LUMPUR

2012

THE DESIGN AND TESTING OF A POWER AUGMENTED WIND TURBINE SYSTEM FOR URBAN HIGH RISE APPLICATION

PAN KOK CHEN

DISSERTATION SUBMITTED IN PARTIAL FULFILLMENT OF THE REQUIREMENTS FOR THE DEGREE OF MASTER OF ENGINEERING SCIENCE

FACULTY OF ENGINEERING

UNIVERSITY OF MALAYA

KUALA LUMPUR

2012

UNIVERSITI MALAYA

ORIGINAL LITERARY WORK DECLARATION

Name of Candidate**: PAN KOK CHEN**

(I.C/Passport No:

Registration/Matric No: **KGA080091**

Name of Degree: **Master of Engineering Science**

Title of ~~Project Paper/Research Report~~/Dissertation/~~Thesis~~ ("this Work"):

The design and testing of a power augmented wind turbine system for urban high rise application

Field of Study: **Mechanical Engineering (Renewable Energy)**

I do solemnly and sincerely declare that:

(1) I am the sole author/writer of this Work;

(2) This Work is original;

(3) Any use of any work in which copyright exists was done by way of fair dealing and for permitted purposes and any excerpt or extract from, or reference to or reproduction of any copyright work has been disclosed expressly and sufficiently and the title of the Work and its authorship have been acknowledged in this Work;

(4) I do not have any actual knowledge nor ought I reasonably to know that the making of this work constitutes an infringement of any copyright work;

(5) I hereby assign all and every rights in the copyright to this Work to the University of Malaya ("UM"), who henceforth shall be owner of the copyright in this Work and that any reproduction or use in any form or by any means whatsoever is prohibited without the written consent of UM having been first had and obtained;

(6) I am fully aware that if in the course of making this Work I have infringed any copyright whether intentionally or otherwise, I may be subject to legal action or any other action as may be determined by UM.

Candidate's Signature Date

Subscribed and solemnly declared before,

Witness's Signature Date

Name:

Designation:

Abstract

The utilization of renewable energy such as wind energy and solar energy is receiving great attention due to the elevated price of fossil fuels in the international market as well as adverse environmental problems from the process of power generation. On-site generation is becoming more widespread for dwelling places, for example, photovoltaic panels, micro-CHP (Combined Heat and Power) and micro-wind. For on-site generation, building integrated wind turbines and solar energy systems serve as attractive opportunities. Retro-fitting high-rise building would be a feasible choice for on-site wind turbine integration since no huge capital investment is involved. However, urban areas generally have weak and turbulent wind conditions due to the presence of high rise buildings. On the other hand, concerns such as visual impact, acoustic pollution, structural issues, safety problems, blade failures and electromagnetic interference need to be addressed. The wind energy generation systems for urban regions on-site generation need to overcome these disadvantages. In this study; an innovative, omni-directional-guide-vane (ODGV) which enhances the performance of a VAWT (vertical axis wind turbine) is introduced. The shrouded design of the ODGV can minimize the public concerns of installing a high-speed rotating wind turbine for on-site power generation and it is aesthetically friendly to an existing building. Through wind tunnel experiment, the ODGV capable to improve the power output of a model drag type VAWT (height = 250 mm, diameter = 500 mm) for 51%, 40%, 30%, and 25% at wind speed 3 m/s, 4.5 m/s, 6.0 m/s and 7.5 m/s respectively. An extended CFD (Computational Fluid Dynamics) study of the ODGV on lift type VAWT has shown encouraging results. The CFD study was to compare the effect of the ODGV on the lift type VAWT by re-simulating the experiment of a single bladed (NACA 0015 airfoil) VAWT published by the Sandia Lab. The simulation boundary conditions are identical to the

Sandia Lab experimental conditions at tip speed ratio, TSR=2.5 and TSR=5. The turbulence model used is shear stress transport (SST) k-ω. From the simulated results, with the employment of the ODGV, it is shown that the torque output of the NACA 0015-airfoil, single bladed VAWT has been increased by 57% and 35% at TSR=2.5 and TSR=5 respectively. As a conclusion, the ODGV wind power generation system improves the power output performance of a VAWT (both drag type and lift type) and it has great potential to be sited in urban areas for on-site and grid-connected power generation.

Abstrak

Penggunaan tenaga boleh diperbaharui seperti tenaga angin dan tenaga solar menerima perhatian yang besar kerana harga yang tinggi bahan api fosil di pasaran antarabangsa serta masalah alam sekitar yang buruk dari proses penjanaan kuasa. Generasi di tapak ini menjadi lebih meluas bagi tempat kediaman, sebagai contoh, panel photovoltaic, mikro-CHP (gabungan Haba dan Tenaga) dan mikro-angin. Bagi generasi di tapak, membina turbin angin yang bersepadu dan sistem tenaga solar berkhidmat sebagai peluang menarik. Retro-pemasangan bangunan bertingkat tinggi akan menjadi pilihan yang sesuai untuk integrasi turbin angin di lokasi sejak tiada pelaburan modal yang besar terlibat. Walau bagaimanapun, kawasan bandar umumnya mempunyai keadaan angin yang lemah dan bergelora kerana kehadiran bangunan tinggi. Sebaliknya, kebimbangan seperti kesan visual, pencemaran akustik, isu-isu struktur, masalah keselamatan, kegagalan bilah dan gangguan elektromagnetik perlu ditangani. Sistem angin penjanaan tenaga untuk kawasan-kawasan bandar di tapak generasi perlu untuk mengatasi kelemahan ini. Dalam kajian ini; inovatif, omni-directional-guide-vane (ODGV), yang meningkatkan prestasi VAWT (turbin angin paksi menegak) diperkenalkan. Reka bentuk ODGV yang selubung boleh mengurangkan kebimbangan orang ramai memasang turbin angin berputar kelajuan tinggi untuk penjanaan kuasa di tapak dan estetika mesra kepada sebuah bangunan yang sedia ada. Melalui eksperimen terowong angin, ODGV mampu untuk meningkatkan output kuasa model VAWT jenis seratan (ketinggian = 250 mm, diameter = 500 mm) sebanyak 51%, 40%, 30%, dan 25% pada kelajuan angin 3 m/s , 4.5 m/s, 6.0 m/s dan 7.5 m/s masing-masing. Sebagai lanjutan, CFD (Dinamik Bendalir Komputeran) kajian ODGV pada VAWT jenis lif telah menunjukkan hasil yang menggalakkan. Kajian CFD adalah untuk membandingkan kesan ODGV terhadap VAWT jenis lif dengan cara simulasi semula

eksperimen berbilah tunggal (NACA 0015 airfoil) VAWT yang diterbitkan oleh Sandia National Laboratory. Keadaan-keadaan sempadan simulasi adalah serupa dengan keadaan eksperimen Sandia National Laboratory pada nisbah tip kelajuan, TSR = 2.5 dan TSR = 5.1. Model gelora yang digunakan adalah Shear Stress Transport (SST) k-ω.Daripada keputusan simulasi, dengan ODGV, ia menunjukkan bahawa output tork NACA 0015-lelayang, tunggal VAWT berbilah telah meningkat sebanyak 57% dan 35% pada TSR = 2.5 dan TSR = 5.1 masing-masing. Sebagai kesimpulan, sistem penjanaan kuasa angin ODGV meningkatkan prestasi kuasa keluaran sebuah VAWT (kedua-dua jenis seretan dan jenis lif) dan ia mempunyai potensi besar yang akan didirikan di kawasan bandar untuk penjanaan kuasa di tapak dan juga disambungkan dengan rangkaian listrik.

Acknowledgement

First of all, the author would like to express gratefulness and thanks so much to project supervisor Dr. Chong Wen Tong, lecturer of Department of Mechanical Engineering, University of Malaya, for giving this opportunity to carry out this project. The author would like to thank the University of Malaya for the assistance provided the research grant allocated to further develop this project. Special credit also goes to Mr. Ahmad Fazlizan for his help to accomplish this project.

Table of Contents

List of Figures

List of Tables

Nomenclature

AoA, α	Angle of attack, °
θ	Azimuth angle, °
σ	Solidity
CHP	Combined heat and power
c	Chord length, m
C_d	Drag coefficient
C_l	Lift coefficient
C_p	Power coefficient
C_τ	Torque coefficient
CFD	Computational fluid dynamics
D	Diameter of the rotor, m
E	Energy, J
F	Force, N
F_d	Drag force, N
$\vec{F}$	External body force, N
F_n	Normal force, N
F_t	Tangential force, N
G_k	Generation of turbulence kinetic energy due to the mean velocity gradients
G_ω	Generation of ω
H	Height of rotor, m
HAWT	Horizontal axis wind turbine
I	Unit tensor

k	Turbulent kinetic energy
L	Span of blade, m
$\dot{m}$	Mass flow rate, kg/s
NACA	National Advisory Committee for Aeronautics
N	Number of blades
ODGV	Omni-directional-guide-vane
PAGV	Power augmentation guide vane
P	Power, W
p	Static pressure, Pa
P_{ext}	Power extracted by rotor, W
P_s	Power extracted by the wind-blown surface, W
$P_{s_{avg}}$	Average power extraction, W
$\rho\vec{g}$	Gravitational body force, N
ρ	Density, kg/m^3
R	Radius of turbine, m
TSR	Tip speed ratio
τ	Torque, Nm
ω	Angular velocity, rad/s
VAWT	Vertical axis wind turbine
V_o	Initial velocity, m/s
V_a	Induced flow velocity, m/s
V_c	Chordal velocity component, m/s
V_{in}	Inletl velocity, m/s
V_n	Normal velocity component, m/s

V_∞	Free stream velocity, m/s
V_s	Velocity of the wind-blown surface moves, m/s
v_1	Upstream wind speed or velocity at point 1, m/s
v_2	Downstream wind speed or velocity at point 2, m/s
ω	Specific dissipation rate
W	Local relative flow velocity, m/s
λ	Tip speed ratio
S	Wind-blown surface, m^2
SIMPLE	Semi-Implicit Method for Pressure Linked Equations
S_k, S_ω	User defined source terms
S_m	Source term
$\bar{\bar{T}}$	Stress tensor
t	Time, s
Γ_k	Effective diffusivity of k
Γ_ω	Effective diffusivity of ω
μ	Molecular viscosity, kg/ms
Y_k	Dissipation of k due to turbulence
Y_ω	Dissipation of ω due to turbulence

CHAPTER 1: Introduction

1.1 Introduction

The utilization of renewable energy such as wind energy and solar energy is receiving great attention due to the elevated price of fossil fuels in the international market as well as adverse environmental problems from the process of power generation. There is an obligation for us to adopt these available sustainable green technologies into our dwelling places.

On-site generation is becoming more widespread for dwelling places, for example, photovoltaic panels, micro-CHP (Combined Heat and Power) and micro-wind (Wright and Firth, 2007). Knight (2004) also reported that there is a great potential to site wind energy generators in urban areas and the research works currently undertaken were led by the European Union. For on-site generation, building integrated wind turbines and solar energy systems serve as attractive opportunities.

Also, from the demonstrative study for the wind and solar power hybrid system conducted at Ashikaga Institute of Technology in Japan, it was confirmed that there is a complementary relationship between wind and solar energy after one year of operation of the system (Kimura *et al*., 1996). Eke *et al*. (2005) also reported that the cost of the hybrid system was found to be less than the individual photovoltaic and wind systems.

1.2 Wind power generation

Energy available in wind is basically the energy of large masses of air moving over the earth's surface. Blades of wind turbine receive this kinetic energy, which is then transformed to mechanical or electrical forms, depending on end use. The efficiency of converting wind to other useful energy forms greatly depends on the efficiency with which rotor interacts with the wind stream which would be discussed in section 2.0 and 2.1.

There are two types of wind turbines used today based on the direction of the rotating shaft (axis) which are horizontal axis wind turbines (HAWT) and Vertical Axis Wind Turbine (VAWT). HAWT have their axis of rotation horizontal to the ground and almost parallel to the wind stream. HAWT have some distinct advantages such as low cut-in wind speed and easy furling. Basically, HAWT show relatively high power coefficient. However, the generator and gearbox of these turbines are to be placed over the tower which makes its design more complex and expensive. Another disadvantage is the need of the tail or yaw drive to orient the turbine towards wind.

For VAWT, it is vertical to the ground and almost perpendicular to the wind direction. The VAWT can receive wind from any direction and thus the complicated yaw devices can be eliminated. The generator and gearbox of such system can be housed at the ground level, so this will makes the tower design simpler and more economical. Moreover the maintenance of these turbines can be done at the ground level. However, the major disadvantage of some VAWT is they are usually not self-starting and they need additional mechanisms to 'push' and rotate the turbine, but it can be achieved by used of on-grid motor (Sandia National Laboratories, 1974).

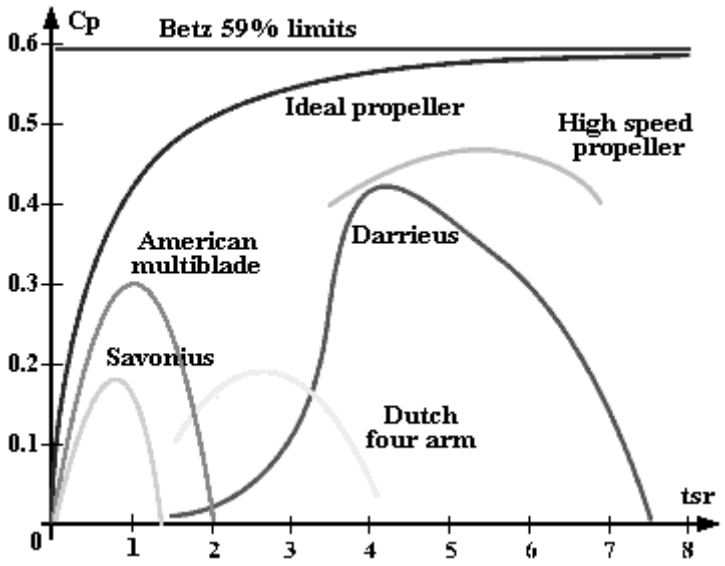

Figure 1.1: The efficiency of various types of wind turbine over tip speed ratio (TSR) (Hau, 2006)

Figure 1.1 shows the efficiency of various types of wind turbine over tip speed ratio (TSR). Noted the theoretical efficiency of wind turbine is limited to 59.3% which is called, Bet'z limit. (See details in section 2.1)

1.3 Building integrations wind energy collection systems

Generally, there are three options available that enable integration of wind energy collection systems into urban environments (Campbell *et al*., 2001):

1. Sitting stand alone wind turbines in urban locations
2. Retro-fitting wind turbines onto existing buildings
3. Fully integrated wind turbines together with architectural form.

Considering the limitation of land in urban areas and the existence of high rise buildings, the first option would be difficult to implement successfully. Moreover, the weak and turbulent wind conditions due to the terrain of the urban area (Knight, 2004) are not suitable for optimum wind turbine operation. It may also give rise to issues or

concerns such as visual impact, acoustic pollution, structural issues, safety problems, blade failures and electromagnetic interference (Oppenheim *et al*., 2004).

Regarding the second option, at present, horizontal and vertical axis small-scale micro-wind turbines are commercially available (Bahaj *et al*., 2007) (Dayan, 2006). Thus, small-scale turbines are easily viable as a building retrofit solution. However, such small-scale wind turbines for building integration may not always be aesthetically pleasing and also hazardous due to turbine blade failures.

The option of a fully integrated solution can be seen implemented in the World Trade Centre of Bahrain (http://www.bahrainwtc.com, 29/09/10). It is a high-rise building that integrates building augmented design incorporated with three horizontal axis wind turbines of 29 m diameter. The building is architecturally innovative, but in reality, this kind of building augmented wind turbine is not always feasible since it involves huge initial costs and a well-defined construction plan. Therefore, the promotion of the wind energy generating system would be slow due to long capital payback period.

Among three mentioned choices, retro-fitting high-rise building would be a feasible choice for on-site wind turbine integration since no huge capital investment is involved. However, urban areas generally have weak and turbulent wind conditions due to the presence of high rise buildings as well as concerns mentioned previously. Thus, wind energy generation systems for urban regions need to overcome these disadvantages.

At the mean time, weak wind region such as Malaysia also experiences low speed winds over the year and most of the areas in the mainland experience low (V_∞< 4 m/s for more than 80% of total hours) and unsteady wind speeds (Soo, 2008). As a result, most of the existing wind turbines are not suitable for Malaysian applications since they are designed for high wind speeds.

Müller *et al.* (2009) have presented, as shown in Figure 1.2, technically and architecturally, the adaption of drag type VAWT for building integration based on a ducted wind turbine system. Grant *et al*. (2008) have also reported that ducted wind turbine which was attached to the roof of a building has the significant potential for retrofitting onto the existing building with minimum visual impact.

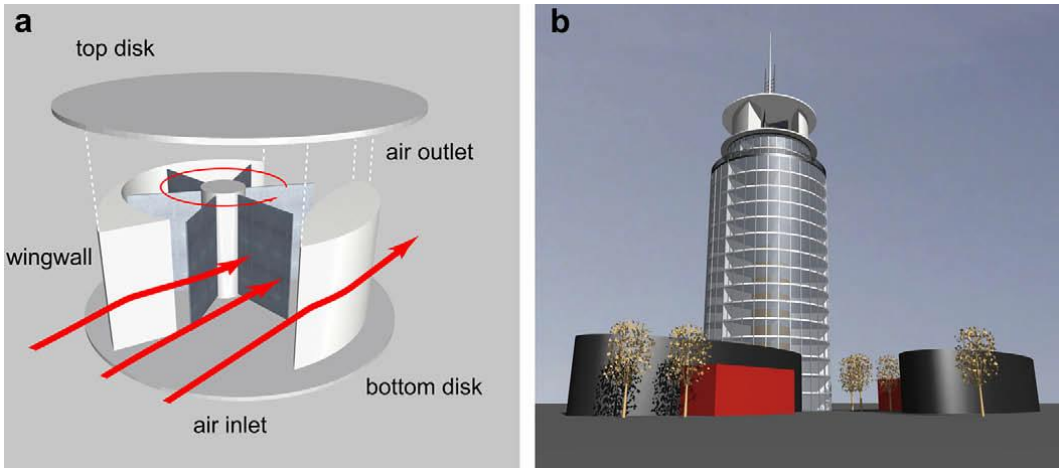

Figure 1.2: Artist's impression of the integration of a large-scale resistance type vertical axis wind turbine. (a) Basic design concept. (b) Integration into a high-rise building. (Müller *et al.*, 2009)

Chong *et al*. (2009) has proposed an innovative system that integrates several green and renewable energy harvesting technologies (wind-solar hybrid energy generation system and rain water collector), Power Augmentation Guide Vane, PAGV, for use on high rise buildings, as shown in Figure 1.3. The system is designed to address

the weak wind and turbulence conditions in urban areas which are not suitable for wind turbine operation. The PAGV preferable couples with vertical axis wind turbine (VAWT).

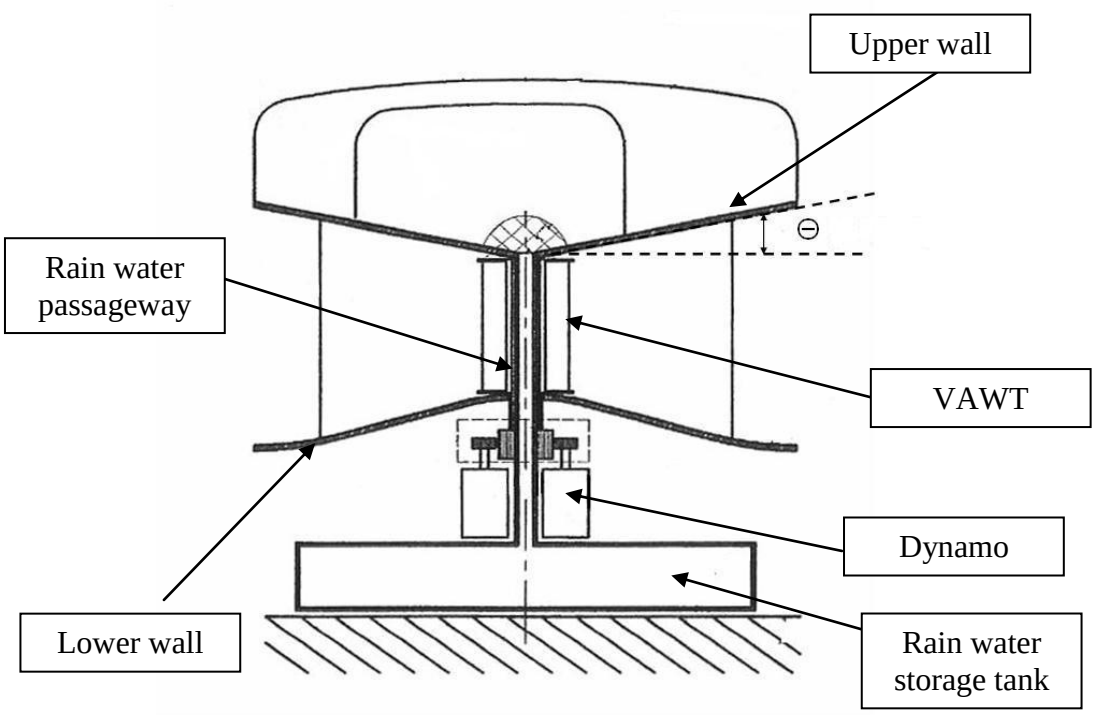

Figure 1.3**:** Section of the PAGV which contains rain water collection system, VAWT and dynamo (Chong *et al.* (2009))

It is reported that vertical axis wind turbine (VAWT) possesses great advantages and is particularly suitable to be built in a turbulent environment (Knight, 2004). VAWT possesses great advantages and is particularly suitable to be built in the turbulent environment (Mertens *et al*., 2003), (Eriksson *et al*., 2008). Moreover, VAWT could be considered for on-site wind energy generation due to relatively uncomplicated design as well as simplicity in fabrication.

The PAGV has the capability to accelerate the on-coming wind to improve starting characteristic for the wind turbine. The system is also designed to provide optimum surface area for solar panel installation on top of the harvester (outer surface of the PAGV upper wall) to generate extra energy from the sunlight. Additionally, rain

water can be collected through the flow paths formed by multi-sector arrangement of the inclined solar panels. The rain water flows towards the center of the system and the collected rain water can be stored in a storage tank for various purposes. The system is designed to complement the building architecture with minimal visual impact so as to overcome the issue concerning public acceptance.

On the other hand, the techno-economic analysis has been carried out on the innovative hybrid renewable energy system with the PAGV (Chong *et al*., 2011). From this study, the technical viability of the system shows that by available technologies of wind turbine and photovoltaic panels, and by taking into account the advantages of the PAGV; this system can cover a significant portion of a building's energy demand and helps to make an independent (or semi independent) building from the urban electricity grid. The importance of the PAGV is determined by comparing the system performance with another system which is technically similar but without the PAGV. Theoretically, there is a 327% increase in energy generation when the PAGV is applied with the PAGV size is 30 m x 14 m whereas the VAWT size is 17 m x 9 m. Figure 1.4 shows the artist's impression of the retrofitting of the PAGV on buildings.

Figure 1.4: Artist's impression of the wind-solar hybrid renewable energy with rain water collection system on buildings (Chong *et al*., 2011)

1.4 Objectives of the study

- To design and build model guide vane for VAWT which is feasible for the study and implementation of wind energy generation in weak wind region and urban area
- To perform simulations and study the effect on application of designed guide vane system on single bladed VAWT

CHAPTER 2: Literature review

As discussed in section 1.1, wind power is the conversion kinetic power from moving wind stream, into a useful form, using wind turbines. The available power from the moving wind stream with velocity, v_1 can be represented as,

$$P = \frac{1}{2}\dot{m}{v_1}^2 \tag{2.1}$$

The mass flow rate, $\dot{m}$ of the wind stream (with density, ρ), $\dot{m}$ across the a cross sectional, A is

$$\dot{m} = \rho A v_1 \tag{2.2}$$

Eq. (2.1) can be rewritten as,

$$P = \frac{1}{2}\rho A {v_1}^3 \tag{2.3}$$

2.1 Derivation of Betz's limit

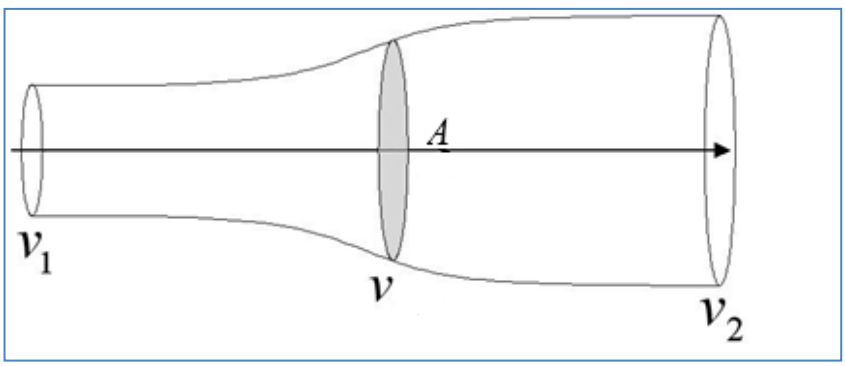

Figure 2.1: Wind stream across a wind turbine with swept area, *A* in a control volume

Now, consider the force exerted on the wind, F by the wind turbine with swept area, A, can be written as,

$$F = m\frac{dv}{dt} \tag{2.4}$$

And, referring to Figure 2.1, v_1 and v_2 is wind speed of upstream and wind speed of downstream of the wind turbine respectively. Hence,

$$F = \dot{m}(v_1 - v_2) \tag{2.5}$$

The power extraction of the wind turbine is dot product of F and v,

$$P_{ext} = F.v \tag{2.6}$$

Substituting Eq. (2.5) into Eq. (2.6), it yields,

$$P_{ext} = \rho A v^2.(v_1 - v_2) \tag{2.7}$$

From Eq. (2.1) and applying principle of conservation of energy,

$$P_{ext} = \frac{\Delta E}{\Delta T}$$

$$P_{ext} = \frac{1}{2}\rho A v({v_1}^2 - {v_2}^2) \tag{2.8}$$

Equating Eq. (2.7) and Eq. (2.8),

$$v = \frac{1}{2}(v_1 + v_2) \tag{2.9}$$

Then, substituting Eq. (2.9) into Eq. (2.8),

$$P_{ext} = \frac{1}{4}\rho A {v_1}^3 \left[1 + \frac{v_2}{v_1} - \left(\frac{v_2}{v_1}\right)^2 - \left(\frac{v_2}{v_1}\right)^3\right] \tag{2.10}$$

The maximum power extraction of a wind turbine can be obtained by differentiating Eq (2.10) respect to $\frac{v_2}{v_1}$, and set the equation to zero. The condition is fulfilled when $\frac{v_2}{v_1}$ is equal to $\frac{1}{3}$. The maximum power extraction equals to

$$P_{ext_{max}} = \frac{1}{2}\rho A {v_1}^3 \left(\frac{16}{27}\right) \tag{2.11}$$

Rearranging Eq (2.11),

$$\left(\frac{P_{ext}}{\frac{1}{2}\rho A {v_1}^3}\right)_{max} = \frac{16}{27}$$

$$C_{p_{max}} = \frac{16}{27} \approx 0.593 \tag{2.12}$$

where C_p is denoted as power coefficient of the wind turbine,

$$C_p = \frac{P_{ext}}{\frac{1}{2}\rho A {v_1}^3} \tag{2.13}$$

The value of $C_{p_{max}}$ is the theoretical power coefficient value that a wind turbine would never exceed, which approximately equals to 0.593. The power coefficient of various types of wind turbines is showed in Figure 1.1.

2.1.1 Tip speed ratio (TSR)

The power coefficient of a wind turbine (no matter of HAWT of VAWT) is always related with parameter, TSR. TSR, λ is an extremely important parameter in designing wind turbine. It is defined as the ratio between tangential velocity of rotor, $R\omega$ and wind speed, V_∞ of wind turbine.

$$\lambda = \frac{R\Omega}{V_\infty} \tag{2.14}$$

where,

Ω = Angular velocity (rad/s)

R = Radius (m)

V_∞ = Free stream wind velocity (m/s)

As shown in Figure 1.1, the wind turbine should be designed according to optimum tip speed ratio in order to produce maximum power output.

2.1.2 Solidity

Solidity (σ) is the ratio of total rotor planform area to total swept area. It is given as:

$$\sigma = \frac{Nc}{R} \tag{2.15}$$

where,

N = Number of blades

c = Chord length (m)

For low solidity wind turbine like Darrieus VAWT, it can produce higher speed and low starting torque. On the other hand, high solidity wind turbine like Savonius wind turbine produces lower speed and higher starting torque.

2.2 General aerodynamic model of drag-type VAWT

Based on the objectives of this study, VAWT to be preferably embed in the PAGV system hence the aerodynamic model of conventional HAWT would not be covered in this report.

A drag-type VAWT rotor converts the kinetic energy from wind to mechanical energy via drag principle with their individual blade. Moving air hits a wind-blown surface, S with drag coefficient of C_d, at velocity, V_o. The power extracted, P_s by the wind-blown surface is calculated by means of the drag force, F_D and the velocity of the wind-blown surface moves, V_s (Figure 2.2).

The power extracted via the drag force principle can be calculated as (Eq. 2.16) (Hau, 2006).

$$P_s = F_D V_s$$

$$P_s = c_d \frac{\rho}{2}(V_o - V_s)^2 S V_s \tag{2.16}$$

(Eq. 2.16) represents the power extraction for a single-bladed drag-type VAWT rotor at, $\theta = 0°$ azimuth angle as per Figure 2.2. If considering different azimuth angles, (Eq. 2.16) should be written in a more general form as (Eq. 2.17).

$$P_s = \overrightarrow{F_d}.\overrightarrow{V_s}$$

$$P_s = c_d \frac{\rho}{2} S\left(\overrightarrow{V_o} - \overrightarrow{V_s}\right)^2 . \overrightarrow{V_s} \tag{2.17}$$

For a single revolution of the blade, the average power extraction $P_{s_{avg}}$ could be obtained by summing up all the P_s at every azimuth angle, as shown in (Eq. 2.18).

$$P_{s_{avg}} = \frac{1}{2\pi} \sum_{\theta=0}^{2\pi} \left\{ c_d \frac{\rho}{2} S\left(\overrightarrow{V_{o\theta}} - \overrightarrow{V_{s\theta}}\right)^2 . \overrightarrow{V_{s\theta}} \right\} \tag{2.18}$$

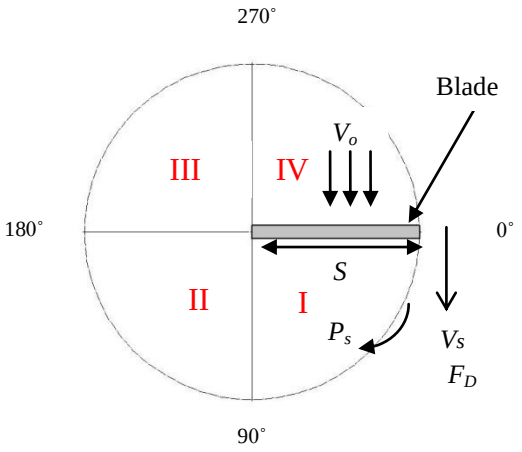

Figure 2.2: Top view of a single-bladed drag-type VAWT and reference azimuth angle

Examining (Eq. 2.18), negative torque of the drag-type would be produced at region from azimuth angle 90˚ to 270˚ (from quadrant II to quadrant III). One can improve the performance of the drag-type VAWT by channeling the free stream, V_o to only region from azimuth angle of 270˚ to 90˚ (from quadrant IV to quadrant I).

The Savonius is basically a drag-type wind turbine with bucket shape. For a 2 bladed Savonius VAWT, the blades are in concave and convex shape, with drag

coefficient at 2.3 and 1.2 respectively for Reynolds' number greater than 10^4 (White, 2005).

2.3 General aerodynamic model of lift-type VAWT

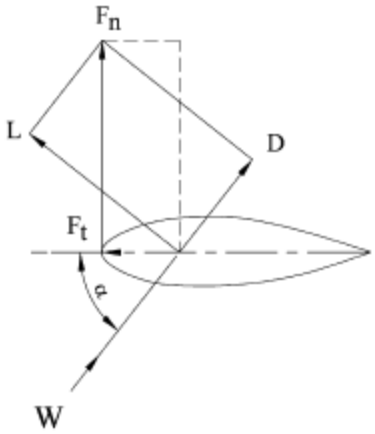

Figure 2.3: Aerodynamic forces acted on an airfoil. (Islam *et al*., 2008)

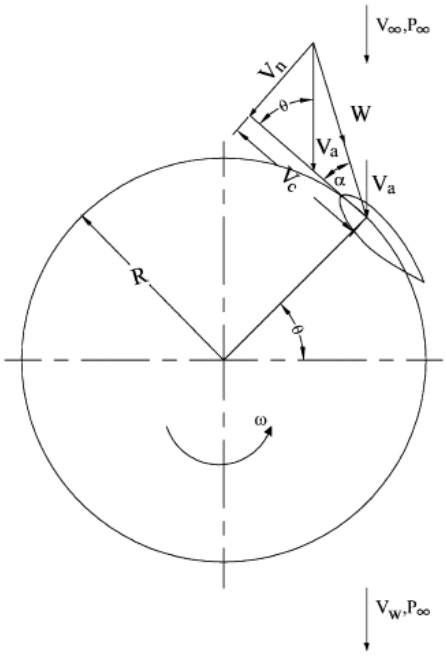

Figure 2.4: Flow velocities of lift-type VAWT. (Islam *et al*., 2008)

When wind is blowing over the airfoil contours of the blade, the pressure difference between the upper and lower surface create aerodynamic lift force and drag

force. The optimal lift force could be obtained if the wind stream “attacks” the airfoil at an optimal angle, so-called angle of attack (AoA), α. Precisely, AoA is the angle between wind stream and chord line of the airfoil.

Lift-type VAWT is a wind turbine which utilize lift force generated from the airfoil geometry wind turbine blades to produce torque hence power. The tangential force is the resolved component of the lift force in chordal direction, as shown in Figure 2.3. Torque, $(F_t \times R)$ drives the wind turbine to spin, following direction of leading edge of the airfoil.

Figure 2.4 shows the flow velocities around a lift-type VAWT. The general aerodynamic of lift-type VAWT is considered as complex and tedious in view of

i. variation of local relative flow velocity, W of VAWT and
ii. rapidly changing of local angle of attack, tangential force and normal force of VAWT
iii. sum of the local torque hence power of the VAWT

2.3.1 Variation of local relative flow velocity, W

The flow velocities in the upstream and downstream sides of the lift-type VAWTs are not constant as seen in Figure. 2.2. From this figure one can observe that the flow is considered to occur in the axial direction. The chordal velocity component V_c and the normal velocity component V_n are, respectively, obtained from the following expressions:

$$V_c = R\Omega + V_a cos\theta \tag{2.19}$$

$$V_n = V_a sin\theta \tag{2.20}$$

Resolving trigonometry in Figure 2.2

$$W = \sqrt{(V_c)^2 + (V_n)^2} \tag{2.21}$$

where,

V_a = induced flow velocity

θ = azimuth angle

2.3.2 Rapidly changing of local angle of attack, tangential force and normal force

Resolving trigonometry in Figure 2.2, the angle of attack, α respect to relative flow velocity, W can be expressed as,

$$\alpha = tan^{-1}\left(\frac{V_n}{V_c}\right)$$

$$\alpha = tan^{-1}\left(\frac{V_a sin\theta}{R\Omega + V_a cos\theta}\right)$$

$$\alpha = tan^{-1}\left(\frac{sin\theta}{\left(\frac{R\Omega}{V_\infty}\right)\left(\frac{V_\infty}{V_a}\right) + cos\theta}\right) \tag{2.22}$$

And, $\lambda = \left(\frac{R\Omega}{V_\infty}\right)$, thus

$$\alpha = tan^{-1}\left(\frac{sin\theta}{(\lambda)\left(\frac{V_\infty}{V_a}\right) + cos\theta}\right) \tag{2.23}$$

As shown in Figure 2.2 (b), the local tangential force and normal force are the difference between the lift force, F_l and drag force, F_d for tangential component and normal component, respectively, which imply that,

$$F_t(\theta) = F_l sin\ \alpha - F_d cos\ \alpha \tag{2.24}$$

$$F_n(\theta) = F_l cos\ \alpha + F_d sin\ \alpha \tag{2.25}$$

where

$$F_l(\theta) = c_l \frac{1}{2} \rho c L W^2 \tag{2.26}$$

$$F_d(\theta) = c_d \frac{1}{2} \rho c L W^2 \tag{2.27}$$

The lift coefficient, c_l and drag coefficient, c_d are determined by different geometry of airfoil of VAWT blade, such as NACA 4-digit airfoil series airfoil and Wortmann's series airfoil. c_l and c_d are empirical data for particular airfoil and L is span length of the blade.

2.3.3 Computation of averaged tangential force and normal force, torque and power

(Eq. 2.24) and (Eq. 2.25) are the local expression of the local tangential force and normal force of a single blade of lift-type VAWT. The computation and expression of the total tangential force for a single revolution of blade is as below,

$$F_{t_{avg}} = \frac{1}{2\pi} \sum_{\theta=0}^{2\pi} F_t(\theta)$$

$$F_{n_{avg}} = \frac{1}{2\pi} \sum_{\theta=0}^{2\pi} F_n(\theta) \tag{2.28}$$

The total torque, τ for lift-type VAWT with N number of blades, is obtained as

$$\tau = NR\ F_{t_{avg}} \tag{2.29}$$

Thus, power of the VAWT can be computed as,

$$P = \tau . \Omega \tag{2.30}$$

2.4 Funneled or shrouded wind power generation system

Over the decades, researchers had studied and reported different designs of ducted or funneled wind turbines which increased the on-coming wind speed hence increasing efficiency and performance of conventional wind turbines and unconventional turbine such as Well Turbine. Govardhan and Dhanasekaran (2001) have shown that the efficiency and starting characteristics of the Wells turbines with guide vanes have improved when compared with the respective turbines without guide vanes.

A lot of research works have been done to improve the performance of horizontal axis wind turbine. Frankovic and Vrsalovic (2001) have designed as a nozzle shaped ring with wings with its lower pressure side pointed towards the centre so that the lift force on each part of the wing is directed radially towards the centre. This induces centrifugal reaction force in the airflow that causes the stream field to expand strongly downstream of the rotor and includes a greater number of streamlines in the active stream in front of the rotor (upstream). Thus the nozzle forces a higher mass flow rate of air through the turbine. The higher mass flow and higher velocity reduction behind the rotor result in a higher energy output from the wind turbine in the nozzle.

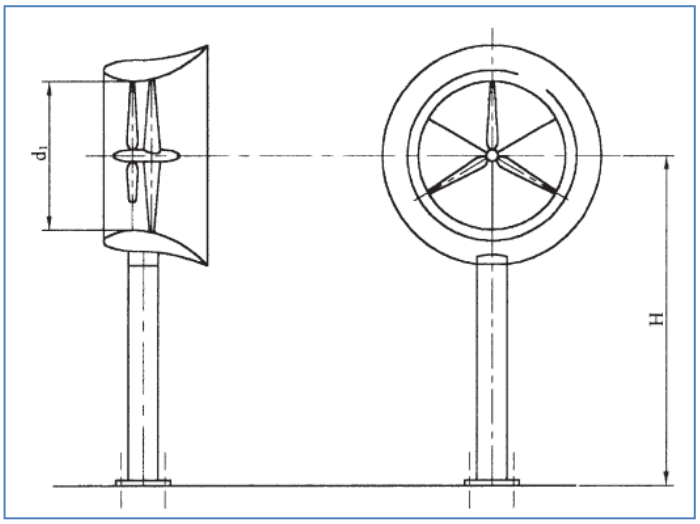

Figure 2.5: Nozzle augmented wind turbine presented by Frankovic and Vrsalovic (2001)

Bet and Grassmann (2003) and Grassmann *et al*. (2003) have reported that by means of employing a wing structure placed at some distance around the turbine, by creating a field of low pressure behind the turbine, the effect of air flow is slowed down and widened hence the corresponding loss in efficiency can be avoided. The wing structure can successfully increase the power of a wind turbine by a factor of 2.0.

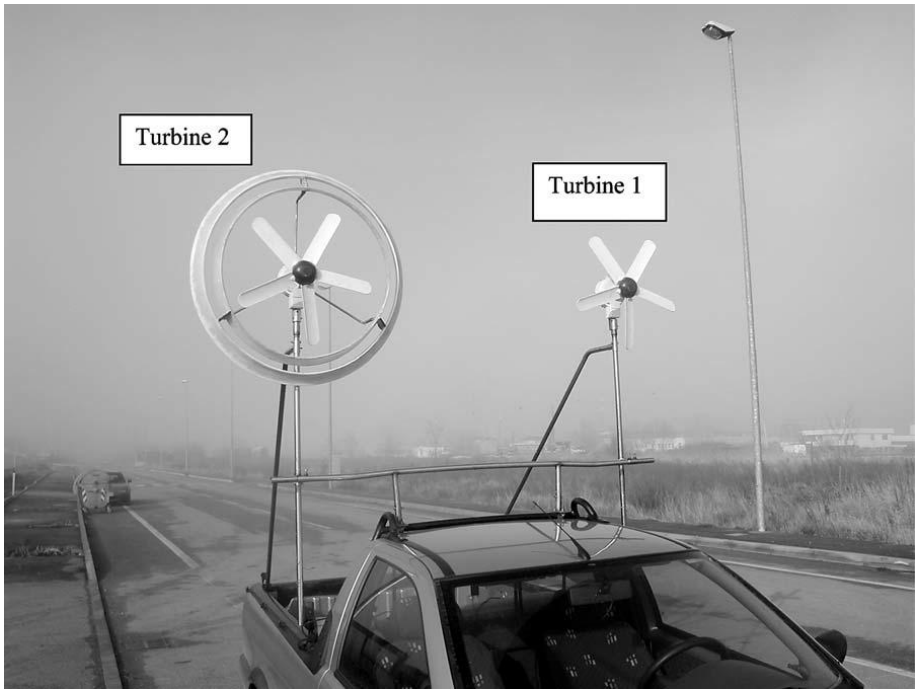

Figure 2.6: Prototype shrouded turbine (turbine 2) by Grassmann *et al*. (2003)

Matsushima *et al*. (2005) has designed frustum-shaped diffuser for horizontal wind turbine.The effect the diffuser's shape had on the wind speed was analyzed by simulation and showed that the wind speed in the diffuser was greatly influenced by the length and expansion angle of the diffuser, and maximum wind speed increased 1.7 times with the selection of the appropriate diffuser shape. Real field tests was conducted by using a real examination device with a diffuser and confirmed that the output power of the wind power generator increased by up to 2.4 times compared to that of a conventional turbine. The only weakness is the performance increment is limited to constant direction only.

Figure 2.7: External view of field trial device installed at test site by Matsushima *et al*. (2005)

A similar designed of diffuser shrouded for HAWT has been studied, designed and presented by Ohya *et al*. (2008). The diffuser design is flanged diffuser design

which the flange design can create low pressure at the rear of the HAWT hence more wind stream could be drawn to the HAWT. As a result of the study, a shrouded wind turbine equipped with a flanged diffuser has been developed, and demonstrated power augmentation for a given turbine diameter and wind speed by a factor of about 4–5 compared to a standard (bare) wind turbine.

Figure 2.8: Prototype wind turbine with a flanged diffuser shroud developed by Ohya *et al*. (2005)

Wang *et al.* (2008) have indicated that by using a scoop, energy capture of wind turbine can be improved at lower wind speeds. By using a scoop, it improves the power output of the Rutland 913 horizontal wind turbine by accelerating the airflow in the cylindrical section. The scoop can perform better, providing a 2.2 times increase in mechanical energy than without a scoop.

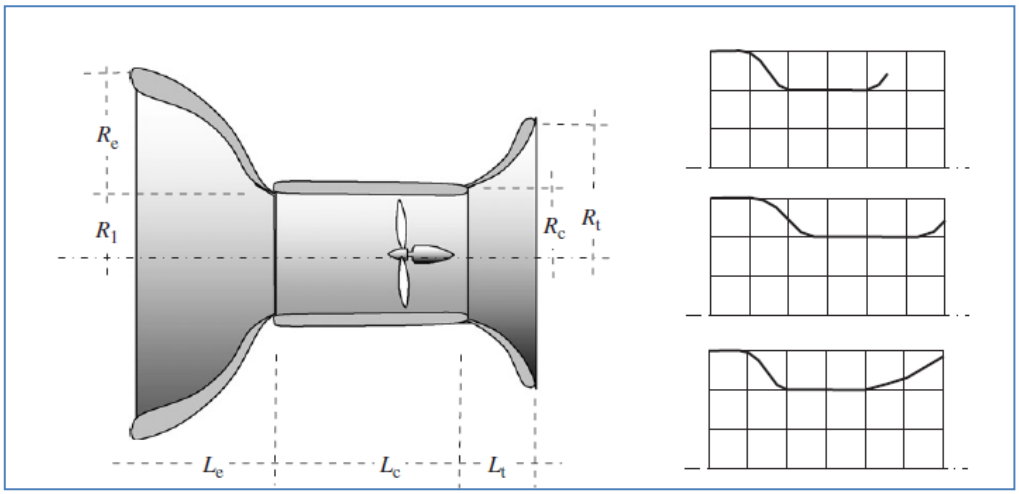

Figure 2.9: Scoop profile and location of HAWT in the HAWT proposed Wang *et al*.(2008)

Hu and Cheng (2008) also presented a bucket-shape ducted wind turbine and tested in the field. According to them, the bucket ducted shape increases the wind speed inside the duct and substantially enhances the efficiency of the wind turbine. The bucket-shape ducted turbine did improve the flow around the generator and thus increased its power extraction efficiency by about 80%.

Figure 2.10: The bucket-shape ducted wind turbine system developed by Hu and Cheng (2008)

In Japan, a study was conducted by Takao *et al.* (2008), which has shown that by adopting the guide vane row, the power coefficient of straight-bladed vertical axis wind (NACA 0015 airfoil) turbine (VAWT) was 1.5 times higher than a wind turbine which has no guide vane.

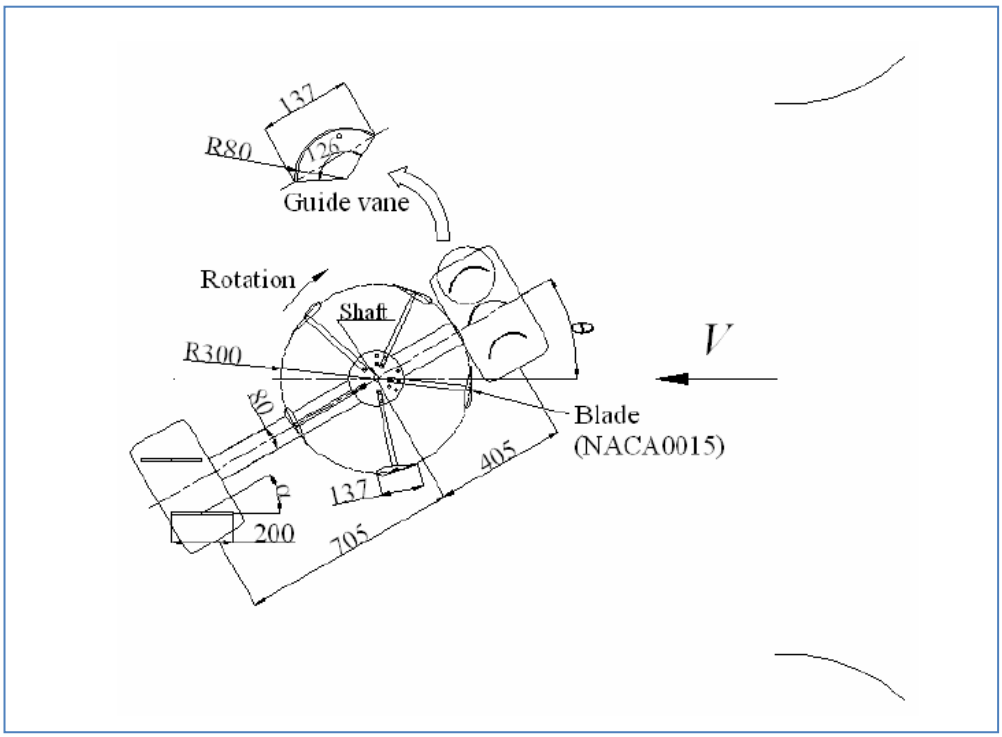

Figure 2.11: Guide vane row proposed by Takao *et al.* (2008)

As for the drag type wind turbine, (Irabu and Roy, 2007) employed a rectangular guide-box tunnel to adjust the inlet mass flow rate and improve the output power of the Savonius rotor. The power coefficient of the Savonius rotor was increased about 1.23 times and 1.5 times for a two bladed rotor and a three-bladed rotor respectively.

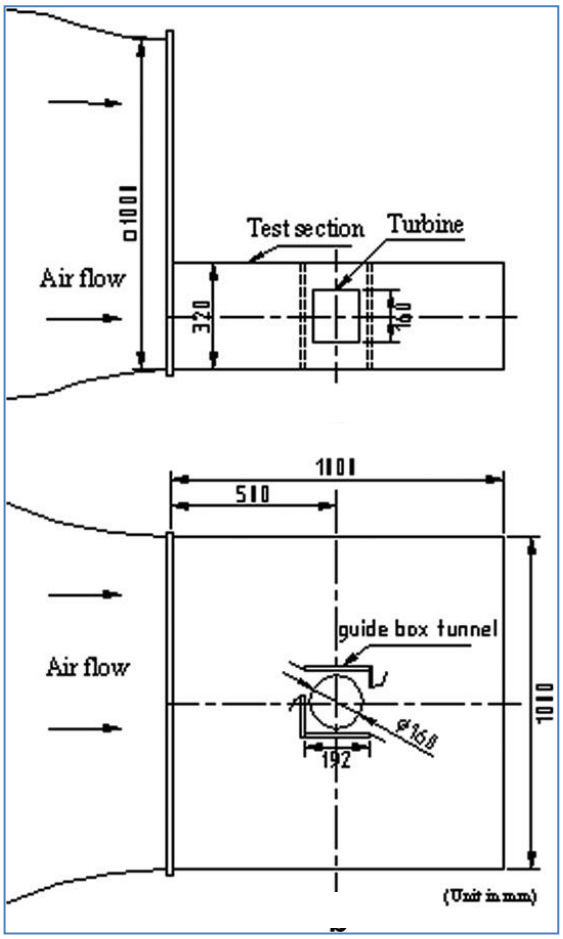

Figure 2.12: Schematic view of experimental apparatus with guide box tunnel (Irabu and Roy, 2007)

Altan and Atilgan (2010) also showed that the introduction of a curtain arrangement placed in front of a Savonius rotor prevents negative torque opposite the rotor rotation, and the maximum power coefficient of the Savonius wind rotor is increased to approximately 38.5%.

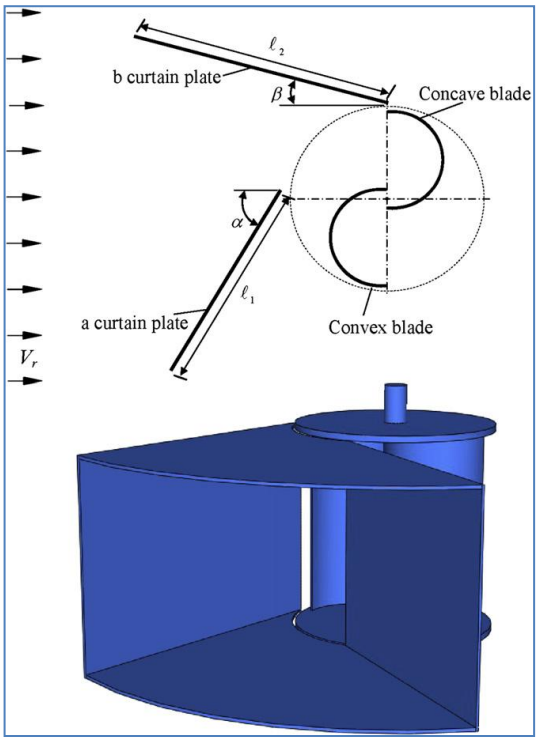

Figure 2.13: Curtain design for Savonius rotor proposed by Altan and Atilgan (2010)

Müller *et al.* (2009) have made a box shape funnel model to increase the theoretical efficiency of a drag type rotor to approximately 48%. The design was tested in an initial experiment, and it was shown that efficiency higher than 40% can be achieved.

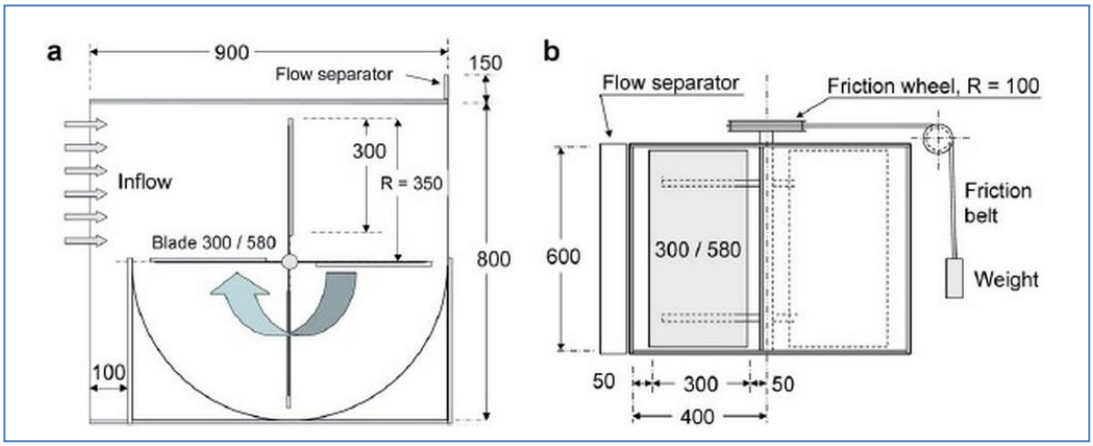

Figure 2.14: A box shape funnel which increase the performance of drag type VAWT (Müller *et al.*, 2009)

CHAPTER 3: Methodology

3.1 The design of guide vane

In this project, the main aim is to study and design guide vane which applicable for the VAWT (both drag type and lift type) while maintaining the capability of the PAGV to serve as hybrid-renewable energy generation in urban area.

Also, as mentioned in section in section 2.2, the performance of the drag-type VAWT can be improved by channeling the free stream, V_o to only region from azimuth angle of 270˚ to 90˚ (quadrant IV and I), as indicated in Figure 2.2. At the same time, the design of the guide vane should maintain the major advantage of VAWT which it can capture wind energy from omni-direction.

By considering the two major factors as mentioned above, the guide vane has been designed as shown in Figure 3.1. Examining Figure 3.1, section A-A, considering the drag-type VAWT (with diameter 500 mm) is rotating in counter-clockwise direction and wind stream is flowing from the azimuth angle of 270˚, the wind stream is being channeled to quadrant IV and near to the location of the tip of drag-type VAWT, which in this case, $R \approx 250\ mm$. Also, the wind stream has been diverted from preventing to enter zone, quadrant II and III, which would produce negative torque relative to the direction of rotation of the VAWT.

The author would like to call the design of the guide vane as Omni-Directional Guide Vane (ODGV) as the circular patterned design has been applied to capture wind energy from four main directions (from azimuth angle of 270˚, 0˚, 90˚ and 180˚).

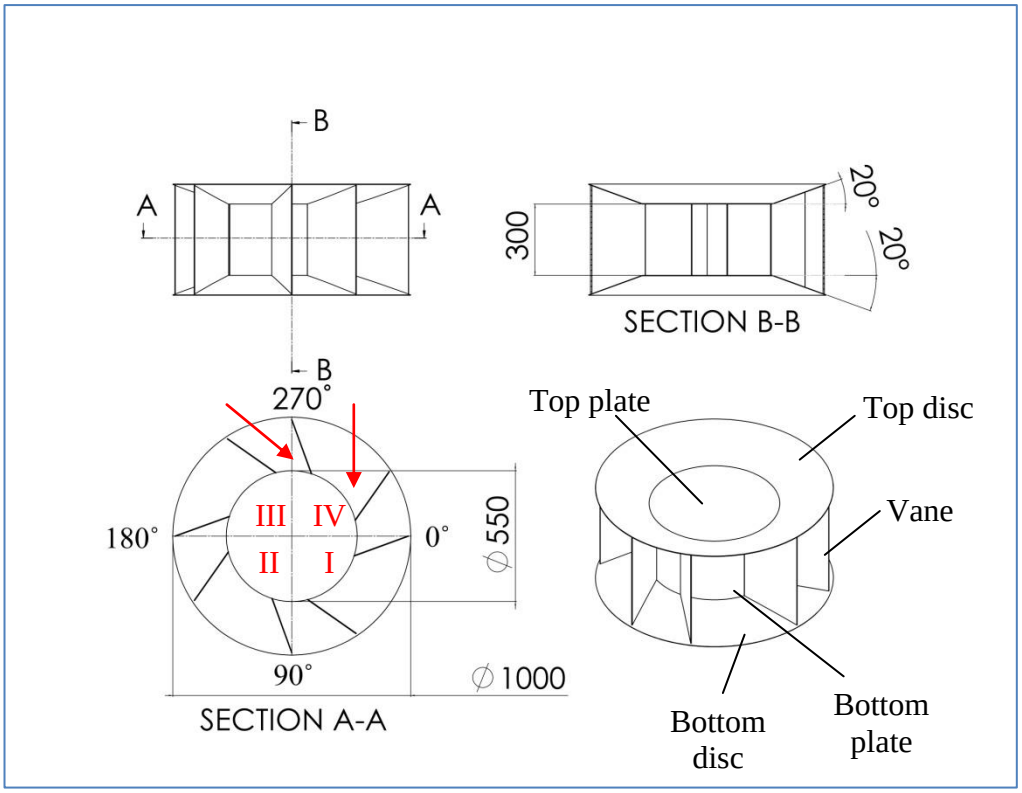

Figure 3.1: General layout of the ODGV

The ODGV has been fabricated based on the design shown in Figure 3.1. The detail drawings of the ODGV are presented in APPENDIX A. The fabricated model of the ODGV (with Savonius VAWT) is shown in Figure 3.2, which is made from two major materials, where plates and discs were made off mild steel sheets and vane was made off Perspex.

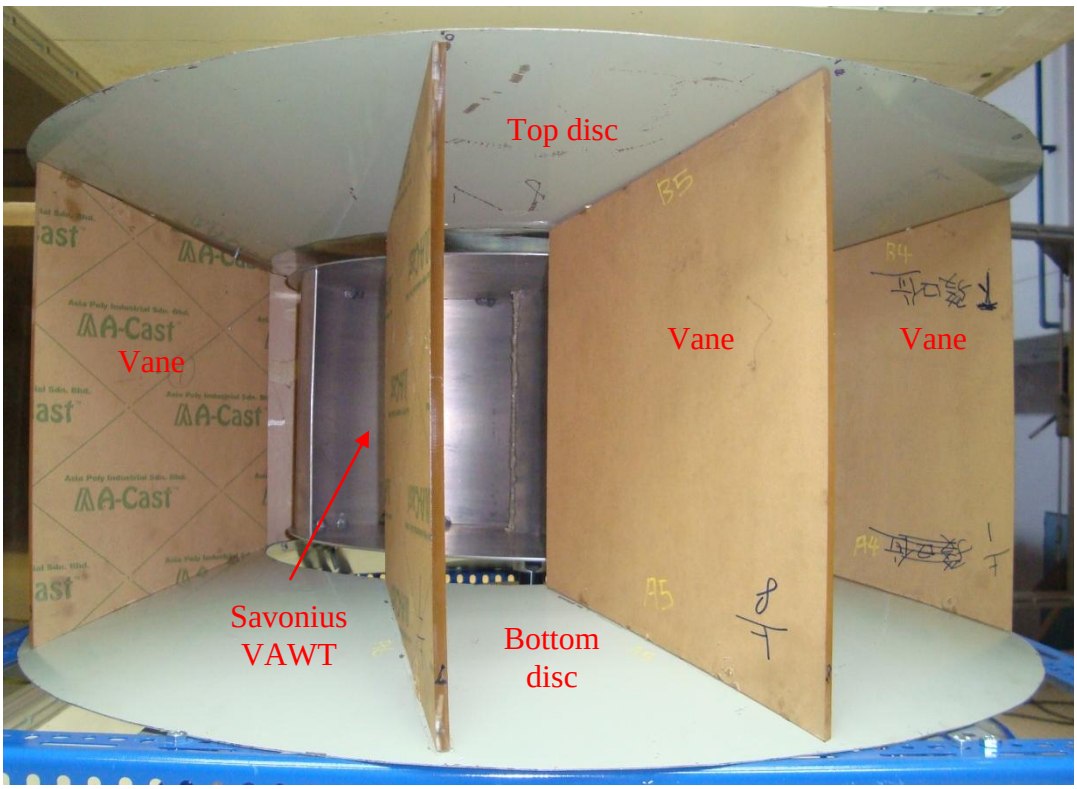

Figure 3.2: Fabricated model ODGV

The outer diameter of ODGV is 1000 mm and the internal diameter is 550 mm with height of 300 mm between top disc and bottom disc. The dimensions were being chosen in order to fit the wind tunnel in University Teknologi Malaysia, Skudai, Johor, Malaysia.

3.2 Experimental method – Savonius VAWT

An under-test unit, two bladed Savonius VAWT with diameter 500 mm and height 250 mm had been designed and fabricated to compare the performance of the Savonius with and without the application of ODGV. The cross-section of the Savonius VAWT was shown in Figure 3.3.

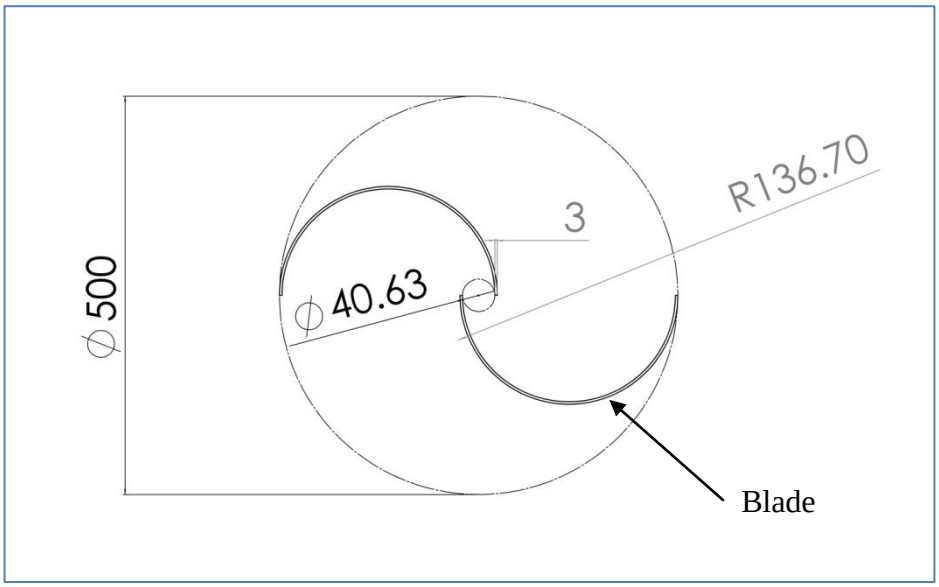

Figure 3.3: Cross sectional of unit undertest, two bladed Savonius VAWT with D, diameter 500 mm and H, height of rotor, 250 mm

3.2.1 Testing of the ODGV with 2 bladed Savonius VAWT in wind tunnel

The testing of model of ODGV with unit under test - 2 bladed Savonius VAWT were conducted in wind tunnel in UTM. The test section of the wind tunnel is 2.0 m (Width) x 1.5 m (Height) x 5.8 m (Long) and more details of the wind tunnel can be found via reference (http://aerolab.fkm.utm.my/?id=TC&pid=724, 02/03/11).

The Savonius VAWT was being supported by two bearing which are SKF roller tapered bearing and SKF ball bearing. The lost (torque and power) from roller tapered bearing (model - 30302 J2) and ball bearing (model - 61802) were calculated from reference

(http://www.skf.com/skf/productcatalogue/calculationsFilter;jsessionid=PeTEBvlT8B3FiBF4Q_HMa-7?lang=en&reloading=false&next=ok&windowName=hDK5eGeM51YiypO4OGDpukM_1300959330860_Calc5&action=Calc5&newlink=&calcform=form1&calc_extrainfo=false&prodid=1310000302&n=158.78+&ny=2.88&Fr=0&Fa=56.1132+&myEHL=0.0020&f01Radio=0&seals=0&DW2=3.5&H=0

, 28/04/11).

The main purpose of the experiment is to compare the performance of the 2 bladed Savonius VAWT with and without the application of the ODGV. There are two main parameters are essential to judge the performance of the Savonius VAWT, which are torque and power, the power coefficient of the rotor is as per Eq. 2.13, or in this case,

$$C_p = \frac{\text{Power extracted}}{\text{Available wind power}}$$

$$C_p = \frac{P_{ext}}{\frac{1}{2}\rho DH{v_\infty}^3} \tag{3.1}$$

Another parameter is TSR, as per Eq. 2.14, by obtaining these two parameters, thus the graph of power coefficient versus TSR were plotted. The arrangement of the testing unit and test rig were shown in Figure 3.4.

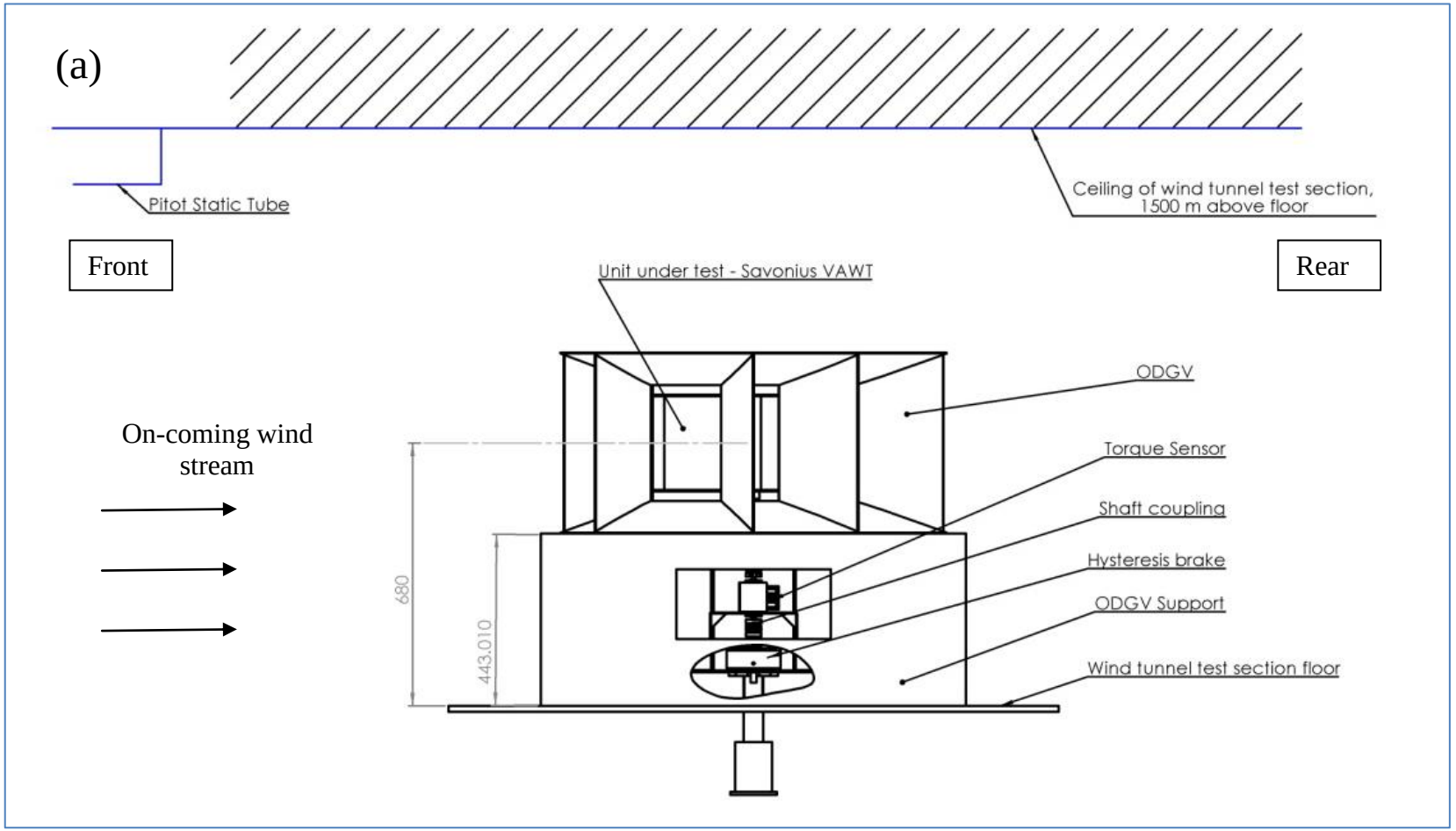

Figure 3.4: The arrangement of the testing unit and test rig in wind tunnel test section. (a) Side view (Schematic)

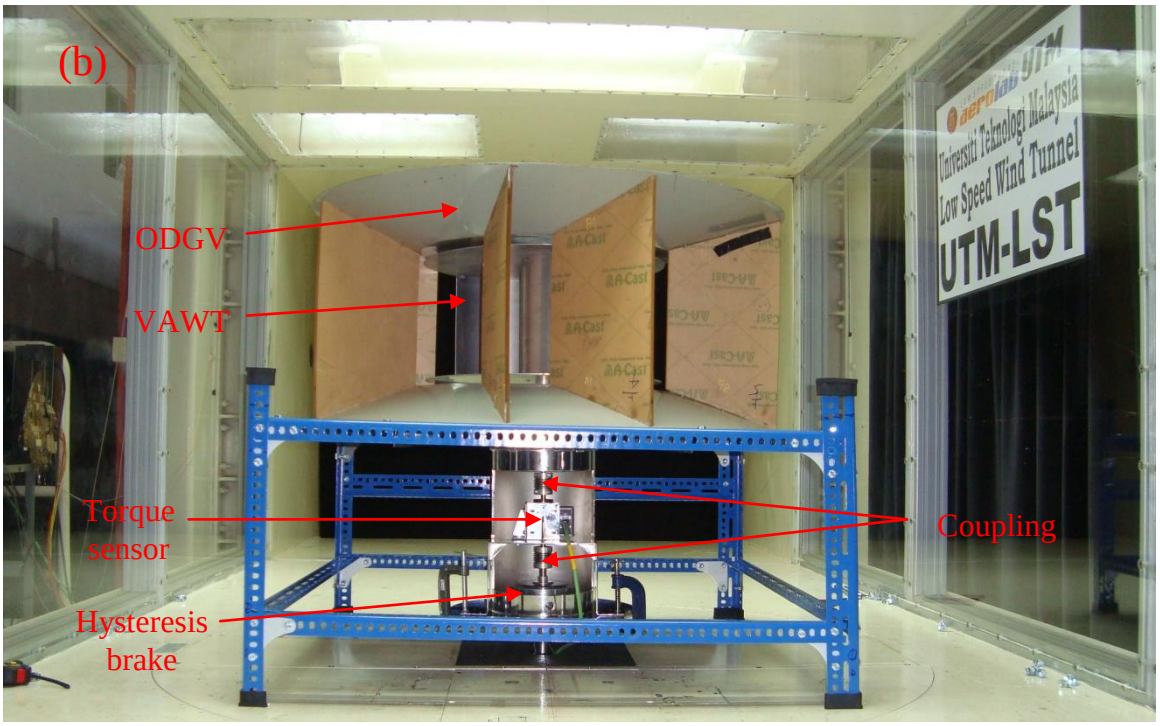

Figure 3.4: The arrangement of the testing unit and test rig in wind tunnel test section.

(b) Actual view- looking to forward

The free stream velocity in wind tunnel was being set via wind tunnel control fan and being sensed by ceiling mounted pitot-static tube. Once the free stream was set to desired velocity, the VAWT was accelerated and was spinning until to a saturated RPM value. Referring to Figure 3.4, there was also a hysteresis brake acted as load to the Savonius VAWT. The VAWT was being brake (or loaded) then the rotational speed of the VAWT was slow down until a steady value. Hence, there was torque produced from the VAWT.

The torque of the Savonius VAWT at the steady value of RPM was measured by using Magtrol TM-305 inline torque transducer as shown in Figure 3.5 (calibration certificate as shown in APPENDIX B).

Figure 3.5: A closer look to the Magtrol TM-305 inline torque transducer which was connected to couplings

The torque value is transient; thus only the steady state torque value was read for analyzing the performance of the VAWT. The torque transducer was came with data logging software, TORQUE 1.0, which has the capability to capture as well as display the transient torque and RPM of the VAWT simultaneously at a preset sampling rate. In the experiment, the sampling rate was set to be 0.05 second. In order to obtain an averaged value of the torque of the VAWT, the interval time of 60 seconds has been chosen for the data logging. As a result, 1200 data were being recorded for a single RPM at a particular on-coming wind speed. Since the VAWT is stopped by hysteresis brake and the angular velocity is decreasing. The decreasing of angular velocity affected the error of torque sensor. According to the calibration certificate from manufacturer,

the combined error for the calibrated torque sensor while in decreasing is 0.1% of full scale deflection. In this experiment, the full scale deflection for the torque sensor would be 2 Nm, thus the decreasing combined error in this experiment would be 0.002 Nm or 2 Nmm.

By increasing the load of the hysteresis brake, the set of torque values versus RPM values (hence power versus TSR curve) were being obtained at a preset free stream wind speed. With the same approach, the experiment has been repeated for the series free stream velocity at 3 m/s, 4.5 m/s, 6 m/s and 7.5 m/s.

The experiment was repeated for twice, one for bare Savonius VAWT and another for Savonius VAWT with ODGV, as to comply with the earlier stated main purpose of the experiment which is to compare the performance of the Savonius VAWT with and without the application of the ODGV. The experiment flow (at a given wind speed) was being summarized and shown in Figure 3.6.

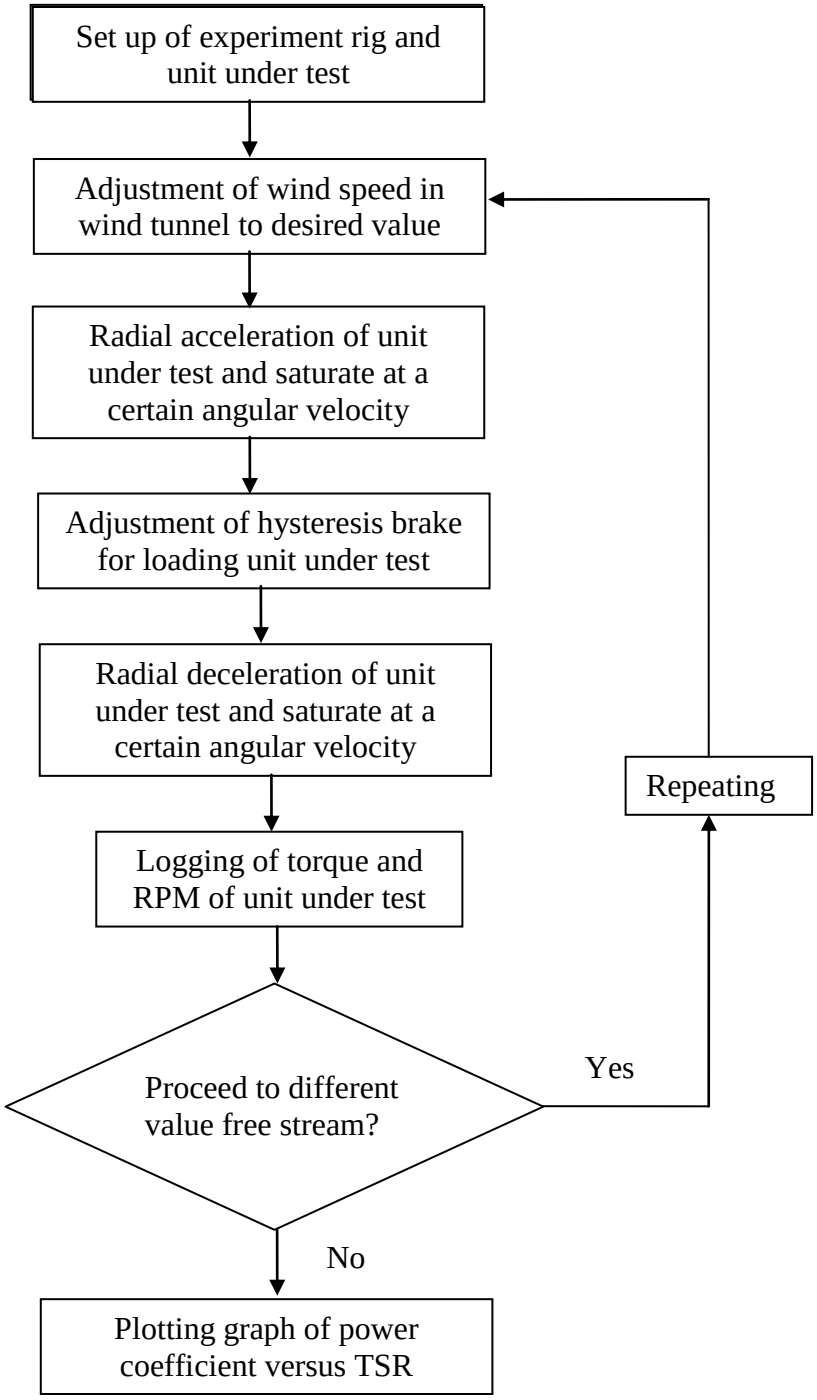

Figure 3.6: Experimental flow chart – The procedure for testing with or without the ODGV is identical

3.3 Computational method – Single bladed NACA 0015 VAWT

An extended study of ODGV has been performed for ODGV with another unit under test; lift type VAWT, single bladed NACA 0015 VAWT. The study has been performed by using Computational Fluid Dynamics (CFD) method since it involves lesser cost and lead time. The study and investigation of the ODGV on the single bladed NACA 0015 VAWT was carried by computational fluid dynamics (CFD) package, FLUENT 6.3.

The effect of application of ODGV is being verified by re-simulating the NACA 0015-airfoil; single bladed VAWT's torque coefficient data, accomplished by Oler *et al.* (Sandia National Laboratories, 1983), published by Sandia lab and comparing the effects with and without the employment of the ODGV for the lift type VAWT. Oler's experiment data was summarized in Table 3.1 and the simulation computational conditions were tabulated as Table 3.2. The boundary conditions of the simulation in Fluent are as per Figure 3.

Table 3.1: Oler's experiment parameters

Parameter	Value
Airfoil chord length, c	0.1524 m
VAWT rotor radius, R	0.61 m
Rotor tip speed, Rω	0.457 m/s
Reynolds number	67,000
Inlet velocity, V_{in}	0.091 m/s (at TSR 5.1)
Inlet velocity, V_{in}	0.183 m/s (at TSR 2.5)

Table 3.2: Computational conditions

Computational conditions			
Density	998.2 kg/m^3	**Interpolating scheme (turbulence)**	2nd Order Upwind
Viscosity	1.003 x 10^{-3} kg/m.s	**Residual error**	1 x 10^{-4}
Pressure	101,325 Pa	**Inlet Boundary Type**	Velocity Inlet
Space /Time	2D /Unsteady, 2nd-Order Implicit	**Reference Frame**	Absolute
Viscous Model	*k* and ω (SST)	**Velocity inlet**	See Table 1
CFD algorithm	SIMPLE	**Blade Motion Type**	Moving Mesh (Rotational)
Interpolating scheme (momentum)	2nd Order Upwind	**Outlet Boundary Type**	Outflow

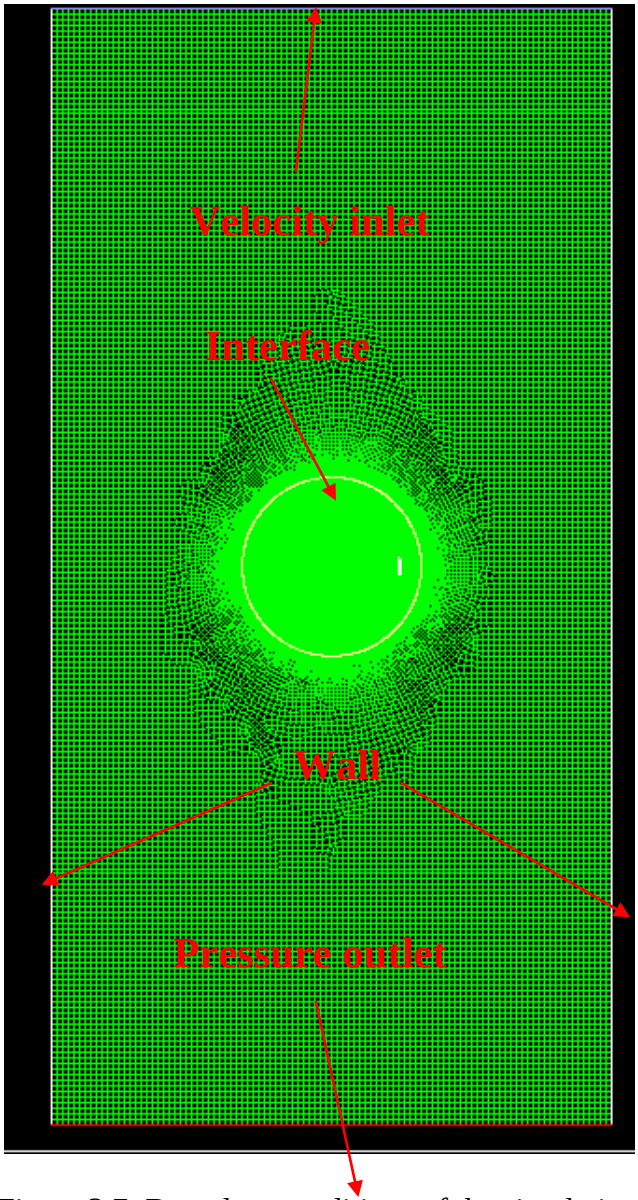

Figure 3.7: Boundary conditions of the simulation

The simulations were repeated with same boundary conditions of the Oler's experiments at TSR 2.5 and TSR 5.1 respectively. The experiment done by Oler *et al.* was used water as a working fluid to facilitate relatively low frequency measurements while working at appropriate blade Reynolds numbers.

3.3.1 CFD solver

The flow-solver is based on the two dimensional Navier-Stokes equations which formulate the principles of conservation of mass, momentum and energy in the form of partial differential equations. The computational domain is divided into cells and discretization of the Navier-Stokes equations using the finite volume method is carried out on each cell in the domain.

In this study, the parameter of temperature is not the interested parameter to be obtained, and velocity and pressure are to be resolved from conservation of mass and momentum of Navier-Stokes equations for an incompressible flow which are (Fluent, 2006):

$$\frac{\delta\rho}{\delta t} + \nabla.(\rho\vec{v}) = s_m\ , \tag{3.2}$$

Eq. 3.2 is the general form of the mass conservation equation and is valid for incompressible as well as compressible flows. The source s_m is the source term.

$$\frac{\delta\rho}{\delta x_i}(\rho\vec{v}) + \nabla.(\rho\vec{v}\vec{v}) = -\nabla p + \nabla.(\bar{\bar{T}}) + \rho\vec{g} + \vec{F} \tag{3.3}$$

where p is the static pressure, $\bar{\bar{T}}$ is the stress tensor (described below), and $\rho\vec{g}$ and $\vec{F}$ are the gravitational body force and external body forces, respectively.

The stress tensor, $\bar{\bar{T}}$ is given by

$$\bar{\bar{T}} = [\mu(\nabla\vec{v} + \nabla\vec{v}^{T}) - \frac{2}{3}\nabla.\vec{v}I] \quad (3.4)$$

where μ is the molecular viscosity, I is the unit tensor, and the second term on the right hand side is the effective of volume dilation.

3.3.2 Finite volume method

The Finite Volume Method (FVM) is one of the most versatile discretization techniques used in CFD for solving the Navier-Stokes, typical partial differential equations. Based on the control volume formulation of analytical fluid dynamics, the first step in the FVM is to divide the domain into a number of control volumes (aka cells, elements) where the variable of interest is located at the centroid of the control volume. The next step is to integrate the differential form of the governing equations (very similar to the control volume approach) over each control volume. Interpolation profiles are then assumed in order to describe the variation of the concerned variable between cell centroids. The resulting equation is called the discretized or discretization equation. In this manner, the discretization equation expresses the conservation principle for the variable inside the control volume.

The most convincing feature of the FVM is that the resulting solution satisfies the conservation of quantities such as mass, momentum, energy, and species. This is exactly satisfied for any control volume as well as for the whole computational domain and for any number of control volumes.

FVM is the ideal method for computing discontinuities solutions arising in compressible flows. Any discontinuity must satisfy the Rankine-Hugoniot jump condition (Versteeg and Malalasekera, 2007) which describes the relationship between the states on both sides of a shock wave in a one-dimensional flow. Since finite volume methods are conservative, they automatically satisfy the jump conditions and hence give physically correct weak solutions.

3.3.3 Turbulence model

All fluid motions, whether turbulent or not, is governed by the dynamical equations for a fluid. The governing equations are momentum, continuity and energy equations, namely, Navier-Stokes equations. A solution of the Navier-Stokes equations is called a velocity field or flow field, which is a description of the velocity of the fluid at a given point in space and time. Once the velocity field is solved for, other quantities of interest (such as flow rate or drag force) may be found.

However, Navier-Stoke equations are in nonlinear partial differential form and they are tough to be solved analytically. Numerically, stable solution of N-S equations could be achieved with very sufficient level of fine mesh, namely, Direct Numerical Simulation (DNS). Therefore, DNS is infeasible for industrial applications due to its excessive computational cost. Alternatively, Large Eddy Simulation generates better result technique, yet it is still not viable for industrial applications because of its relatively high computational cost. For common engineering applications, Reynolds-Averaged Navier–Stokes (RANS) equations with supplemented turbulence models (such as k- ε model, k-ω model and etc) are more favorable with reasonable computational cost. One of the common turbulence models is SST k-ω.

Reynolds-averaged Navier-Stokes (RANS) equations is the oldest approach to turbulence modeling. An ensemble version of the governing equations is solved, which introduces new apparent stresses known as Reynolds stresses. This adds a second order tensor of unknowns for which various models can provide different levels of closure. It is a common misconception that the RANS equations do not apply to flows with a time-varying mean flow because these equations are 'time-averaged'. In fact, statistically unsteady (or non-stationary) flows can equally be treated. There is nothing inherent in Reynolds averaging to preclude this, but the turbulence models used to close the equations are valid only as long as the time scale of these changes in the mean is large compared to the time scales of the turbulent motion containing most of the energy. RANS models can be divided into two broad approaches:

a) Boussinesq hypothesis: This method involves using an algebraic equation for the Reynolds stresses which include determining the turbulent viscosity, and depending on the level of sophistication of the model, solving transport equations for determining the turbulent kinetic energy and dissipation. Models include k-ε (Spalding), Mixing Length Model (Prandtl) and Zero Equation (Chen).The models available in this approach are often referred to by the number of transport equations they include, for example the Mixing Length model is a "Zero Equation" model because no transport equations are solved, and the k-ε on the other hand is a "Two Equation" model because two transport equations are solved.

b) Reynolds stress model (RSM): This approach attempts to actually solve transport equations for the Reynolds stresses. This means introduction of several

transport equations for all the Reynolds stresses and hence this approach is much more costly in CPU effort.

3.3.4 Governing equations of SST *k-ω*

The SST (Shear Stress Transport) *k-ω* turbulence model was deployed in the simulation because this model could produce more accurate and reliable results for the kind of flow under study as shown by (Menter *et al*., 2003).

The general advantage of SST *k-ω*, are

- The standard *k-ω* model and the transformed *k-ε* model are both multiplied by a blending function and both models are added together. The blending function is designed to be one in the near-wall region, which activates the standard *k-ω* model, and zero away from the surface, which activates the transformed k-ε model.
- The SST model incorporates a damped cross-diffusion derivative term in the ω equation.
- The definition of the turbulent viscosity is modified to account for the transport of the turbulent shear stress.
- The modeling constants are different.

The turbulence kinetic energy, k, and the specific dissipation rate, ω, are obtained from the following transport equations (Fluent, 2006):

$$\frac{\delta}{\delta t}(\rho k) + \frac{\delta}{\delta x_i}(\rho k u_i) = \frac{\delta}{\delta x_j}\left(\Gamma_k \frac{\delta k}{\delta x_j}\right) + G_k - Y_k + S_k \,, \tag{3.5}$$

$$\frac{\delta}{\delta t}(\rho \omega) + \frac{\delta}{\delta x_i}(\rho \omega u_i) = \frac{\delta}{\delta x_j}\left(\Gamma_\omega \frac{\delta \omega}{\delta x_j}\right) + G_\omega - Y_\omega + S_\omega \tag{3.6}$$

In these equations, G_k represents the generation of turbulence kinetic energy due to mean velocity gradients. G_ω represents the generation of ω. Γ_k and Γ_ω represent the effective diffusivity of k and ω, respectively. Y_k and Y_ω represent the dissipation of k and ω due to turbulence. S_k and S_ω are user-defined source terms.

The SST *k-ω* model is also known to have reduced sensitivity to far field values of turbulence frequency, ω, and a more balanced performance for a wide range of flow types compared to other general-purpose two equation models, as demonstrated by Menter *et al.* (2003). The SIMPLE (Semi-Implicit Method for Pressure Linked Equations) algorithm of Patankar and Spalding (1972) was used to solve the conservation equations resulting from the discretization. Essentially, the SIMPLE algorithm links the mass conservation equation to the momentum equations via pressure correction. This algorithm was chosen for this study because of its computational efficiency, robustness in iterating the coupled parameters and higher-order differencing schemes are available for this algorithm. The convective terms were numerically differentiated with the linear upwind differencing scheme, providing a balance between accuracy and computing cost.

The sliding mesh method was chosen over the steady rotating reference frame method, since, after preliminary investigations, the former gave a more accurate result compared to the latter (Pope *et al.*, 2009). This is due to the fact that with the sliding mesh method, the transient effect of blade movement is taken into account, whereas with the rotating reference frame method, the effect of rotation is only calculated at an instant in time. Hwang *et al*. (2009) and Howell *et al*. (2010) also performed CFD

simulation of VAWT in sliding mesh method. This gives reasons why a particular method (Table 3.2) was used.

3.4 Computational grid and power acquisition of rotor

The computational domain was being meshed by using GAMBIT software. The domain is shown in Figure 3.8 (a), indicating sliding mesh zone. Azimuth angle of 0 ° is the starting position of the VAWT.

Three different types of mesh have been created for mesh independent study as shown in Table 3.3. The mesh independent study was being reported in section 4.1. With the mesh independent study, there are totally 250,658 of mesh in the computational zone. 220,028 of mesh or 87.78% of the total quantity are the mesh in sliding zone to simulate dynamic characteristic of the VAWT.

Table 3.3: Sets of generated mesh for mesh independent study

Region	Cell Quantity		
	Mesh 1	**Mesh 2**	**Mesh 3**
Water tunnel	28,177	31,852	30,630
Rotary maingrid	74,844	92,133	95,711
Rotary subgrid	58,903	85,569	124,317
Total	**161,924**	**209,554**	**250,658**

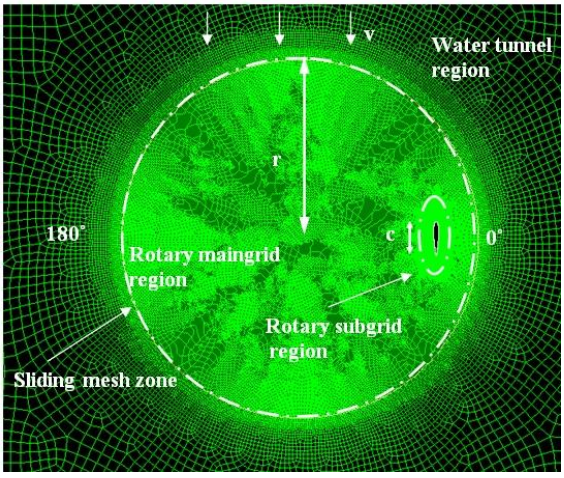

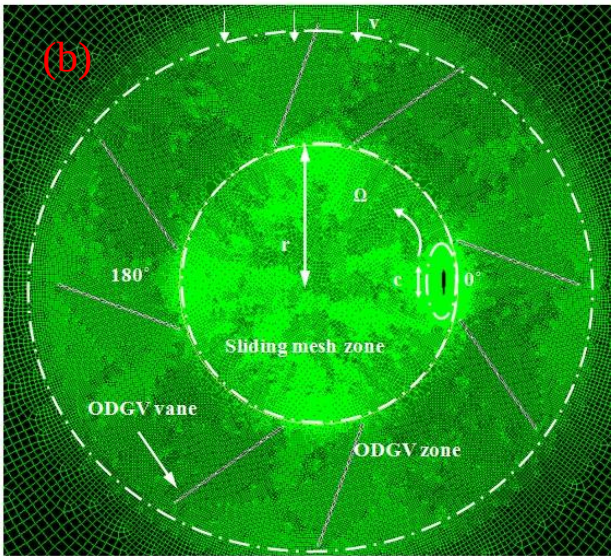

Figure 3.8: (a) Mesh for VAWT only (b) Mesh for VAWT with presence of the ODGV

For VAWT with the ODGV, as in Figure 3.8 (b), the ODGV surrounds the VAWT. The boundary conditions of computational model are identical to Oler's experiment at TSR 5.1 and TSR 2.5 respectively. The mesh of the VAWT with the ODGV is also same with the bare VAWT case but with additional ODGV zone. This zone comprises 47,422 of mesh quantity.

In Fluent, the software is capable to capture surface pressure on the NACA 0015 blade, hence the force and the torque (with moment arm equals to R). The torque value of the blade was being captured in non-dimensional form, the coefficient of torque, $C\tau$, (Eq. 3.7), at each single degree of azimuth angle. After completion one cycle of the VAWT, all 360 set of data was being averaged, $C\tau_{avg}$. The average power coefficient extracted from the rotor, C_{pavg} were calculated using (Eq. 3.8).

$$C_\tau = \frac{\tau}{{}^1/_2\,\rho c H v_{in}{}^2 R} \text{ , for blade} \tag{3.7}$$

$$C_{p_{avg}} = C_{\tau_{avg}} \times \text{TSR} \times \frac{c}{2R} \text{, for rotor} \tag{3.8}$$

CHAPTER 4: Results and discussions

4.1 Results of C_p versus TSR of 2 bladed Savonius VAWT without ODGV

The transient data, torque and angular velocity (in RPM) were logged by Magtrol TM 305 torque transducer and TORQUE 1.0 software over one hundred and twenty seconds logging period. Figure 4.1 shows the print screen of the transient torque, power and RPM value of the bare 2 bladed Savonius VAWT at 153 rpm and on-coming wind speed of 3 m/s. For other test conditions (without the ODGV), the data logging print screen are in APPENDIX C.

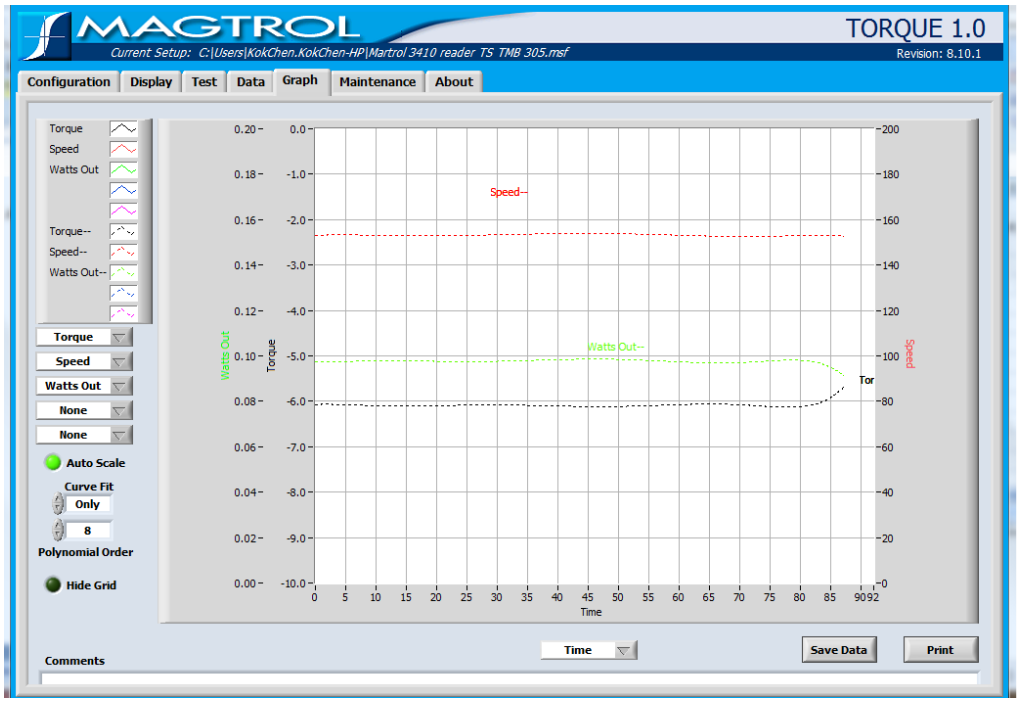

Figure 4.1: Print screen of the transient torque, power and RPM value of the bare 2 bladed Savonius VAWT at 153 rpm and on-coming wind speed of 3 m/s

In order to plot graph C_p versus TSR, higher load was applied to the VAWT which yielded the VAWT had been decelerated to 125.32 rpm. Subsequent another

higher load had been further applied to the VAWT, thus the angular velocity of the VAWT was decelerated to 107.21 rpm, 87.51 rpm and 59.90 rpm after three levels of load. The respective transient torque values were logged for each rpm.

The torque shown in software does not include the torque lost due to bearing friction. Thus, the total torque can be represented by,

$$\tau_{total} = \tau_{measured} + \tau_{bearing} \tag{4.1}$$

Where $\tau_{measured}$ is the averaged torque value of 1200 points data over the logging period of one hundred and twenty seconds, and $\tau_{bearing}$ is the torque lost due to bearing friction. The details of $\tau_{bearing}$ calculation are shown in APPENDIX D.

Table 4.1 summarized all the respectively RPMs, measured torque by the torque sensor and calculated bearing lost at on-coming wind speed of 3 m/s.

Table 4.1: Summary of angular velocity, torque, power and TSR of 2 bladed Savonius VAWT only at 3.0 m/s

RPM	**Measured torque (N mm)**	**Measured power (W)**	**Bearing Lost Power (W)**	**Total Power (W)**	**TSR**	***Cp***
153.20	-6.0857	0.0976	0.1510	0.2486	1.3371	0.1203
125.32	-16.5264	0.2169	0.1210	0.3379	1.0938	0.1635
107.21	-21.0669	0.2365	0.1020	0.3385	0.9357	0.1637
87.51	-29.3233	0.2467	0.0821	0.3508	0.7638	0.1591
59.90	-39.1400	0.2457	0.0547	0.3004	0.5228	0.1453

Same approach has been repeated for obtaining graph of C_p versus TSR at on-coming wind speed of 4.5 m/s, 6.0 m/s and 7.5 m/s. The result was tabulated in Table 4.2, Table 4.3 and Table 4.4.

Table 4.2: Summary of angular velocity, torque, power and TSR of 2 bladed Savonius VAWT only at 4.5 m/s

RPM	Measured torque (N mm)	Measured power (W)	Bearing Lost Power (W)	Total Power (W)	TSR	*Cp*
229.70	-4.8907	0.1213	0.2370	0.3583	1.3365	0.0174
201.53	-27.0164	0.5701	0.2050	0.7751	1.1726	0.0817
162.22	-46.0041	0.7815	0.1610	0.9425	0.9439	0.1120
119.74	-65.8468	0.8257	0.1150	0.9407	0.6967	0.1184

Table 4.3: Summary of angular velocity, torque, power and TSR of 2 bladed Savonius VAWT only at 6.0 m/s

RPM	Measured torque (N mm)	Measured power (W)	Calculated Bearing Lost Power (W)	Total Power (W)	TSR	*Cp*
305.00	-5.7645	0.1870	0.3260	0.5130	1.3310	0.0310
285.60	-28.7146	0.8589	0.3020	1.1609	1.2463	0.0702
250.10	-61.6767	1.6152	0.2600	1.8752	1.0914	0.1134
182.60	-101.0710	1.9327	0.1830	2.1157	0.7968	0.1279
125.97	-138.3600	1.8252	0.1220	1.9472	0.5497	0.1177

Table 4.4: Summary of angular velocity, torque, power and TSR of 2 bladed Savonius VAWT only at 7.5 m/s

RPM	Measured torque (N mm)	Measured power (W)	Calculated Bearing Lost Power (W)	Total Power (W)	TSR	*Cp*
382.00	-7.3301	0.2931	0.4210	0.7141	1.3336	0.0220
343.70	-58.8385	2.1179	0.3730	2.4909	1.1999	0.0768
311.11	-91.0074	2.9650	0.3330	3.2980	1.0861	0.1017
286.94	-119.6900	3.5966	0.3040	3.9006	1.0017	0.1203
275.70	-126.8000	3.6605	0.2910	3.9515	0.9625	0.1218
209.25	-174.8400	3.8314	0.2130	4.0444	0.7305	0.1247
128.76	-223.6400	3.0154	0.1250	3.1404	0.4495	0.0968

Referring to Figure 4.2, generally, the dimensionless quantities, for different on-coming wind speed, C_p and TSR are fall in approximately same range, where C_p ranges

from 0 to 0.13 while TSR ranges from 0.5 to 1.3. It is also noted that after the peak TSR, continuously increasing load to the VAWT was not produced power at a steady RPM, and the VAWT was stopped eventually. In other words, the VAWT cannot sustain at a steady RPM after the peak TSR and keeps on decreasing its angular velocity and eventually stopped. This scenario also explains why the experiment did not obtain data at low TSR (TSR < 0.4).

From calibrated certificate supplied by the manufacturer, the combined error for decreasing signal of the torque sensor is 2 Nmm. This error value has gave impact on the measurement of especially on low on-coming wind speed condition, where the the VAWT angular velocity and measured torque value which are relatively low. For 3 m/s on-coming wind speed, the combined error for decreasing signal of the measured peak power value is approximately 7%. This error may lead to higher measured torque value was obtained for low on-coming wind speed. For other on-coming testing condition/ wind speed, the combined error for decreasing signal of the measured peak power value are approximately 3%, 2% and 1% for on-coming wind speed of 4.5 m/s, 6 m/s and 7 m/s respectively.

The error of result C_p versus TSR curve is believed to be greater since there are also additional errors sources in the experiment such as fluctuation of on-coming wind and mechanical friction calculation. However, the reproducibility and repeatability of the curve is quite good, apart from curve for on-coming wind speed of 3m/s.

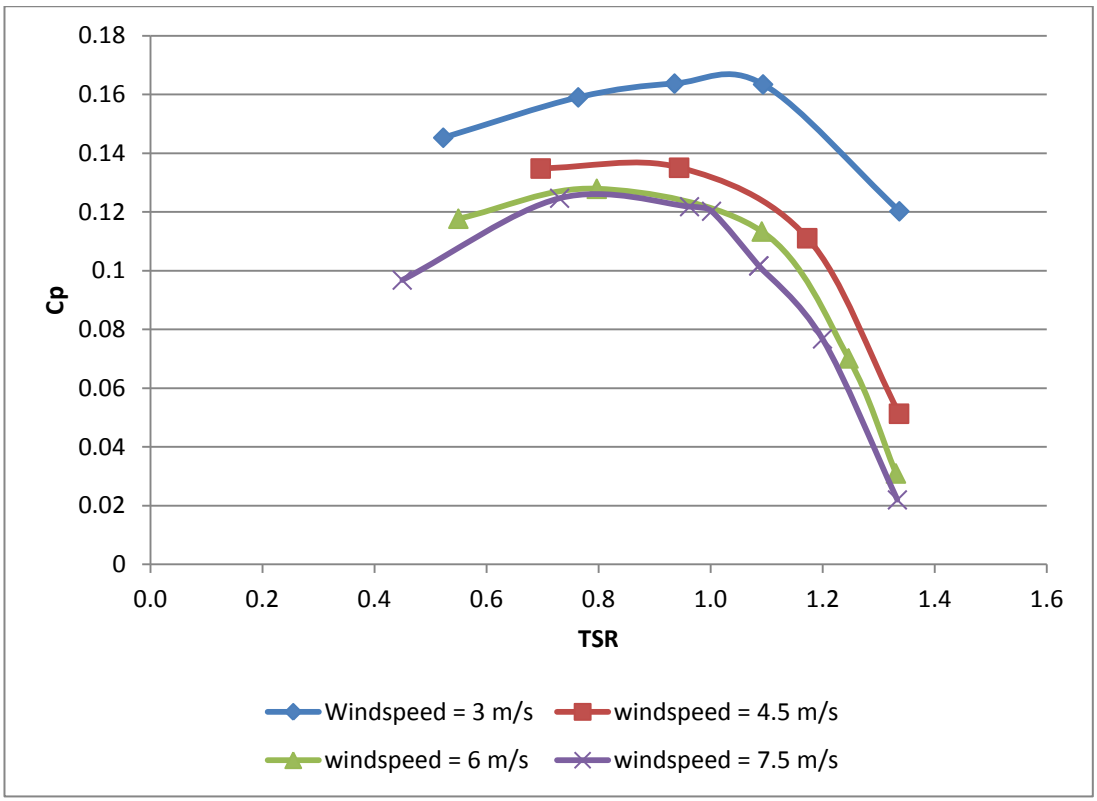

Figure 4.2: Summary of C_p versus TSR for bare Savonius VAWT at various on-coming wind speed

4.2 Results of C_p versus TSR of 2 Bladed Savonius VAWT with ODGV

In order to compare the effect of application of the ODGV on Savonius VAWT, the whole configuration of the experiment has been repeated exactly same except for the existence of ODGV. Table 4.5 through Table 4.8 tabulated the results of angular velocity, torque, power coefficient and TSR of the 2 bladed savonius VAWT with application of the ODGV and the print screen of data logging (with the ODGV) are in APPENDIX E. The summary of the C_p versus TSR was summarized in Figure 4.3.

Table 4.5: Summary of angular velocity, torque, power and TSR of 2 bladed Savonius VAWT with ODGV at 3.0 m/s

RPM	Measured torque (N mm)	Measured power (W)	Calculated Bearing Lost Power (W)	Total Power (W)	TSR	C_p
170.60	-2.5378	0.0466	0.1700	0.2166	1.4890	0.1043
162.70	2.3818	0.0427	0.1610	0.2037	1.4200	0.0981
158.90	-9.0486	0.1505	0.1570	0.3075	1.3868	0.1481
146.20	-15.6949	0.2403	0.1430	0.3833	1.2760	0.1847
140.00	-19.7885	0.2901	0.1370	0.4271	1.2219	0.2058
126.80	-27.6879	0.3677	0.1230	0.4907	1.1067	0.2364
108.47	-37.7797	0.4292	0.1040	0.5332	0.9467	0.2569

Table 4.6: Summary of angular velocity, torque, power and TSR of 2 bladed Savonius VAWT with ODGV at 4.5 m/s

RPM	Measured torque (N mm)	Measured power (W)	Calculated Bearing Lost Power (W)	Total Power (W)	TSR	C_p
239.20	-0.7998	0.0467	0.2480	0.2947	1.3918	0.0421
226.80	-11.9896	0.2848	0.2330	0.5178	1.3196	0.0739
191.00	-40.2045	0.8039	0.1930	0.9969	1.1113	0.1423
160.10	-66.1506	1.1093	0.1580	1.2673	0.9315	0.1809
135.50	-84.1418	1.1938	0.1320	1.3258	0.7884	0.1893

Table 4.7: Summary of angular velocity, torque, power and TSR of 2 bladed Savonius VAWT with ODGV at 6.0 m/s

RPM	Measured torque (N mm)	Measured power (W)	Calculated Bearing Lost Power (W)	Total Power (W)	TSR	C_p
307.00	-2.2960	0.0810	0.3280	0.4090	1.3397	0.0246
297.60	-13.9563	0.4349	0.3170	0.7519	1.2987	0.0453
279.80	-34.1439	1.0003	0.2960	1.2963	1.2210	0.0781
266.13	-47.7053	1.3295	0.2790	1.6085	1.1613	0.0969
234.18	-82.2411	2.0169	0.2420	2.2589	1.0220	0.1360
210.45	-107.8100	2.3759	0.2150	2.5909	0.9184	0.1560
188.80	-129.8400	2.5677	0.1900	2.7577	0.8239	0.1661

Table 4.8: Summary of angular velocity, torque, power and TSR of 2 bladed Savonius VAWT with ODGV at 7.5 m/s

RPM	Measured torque (N mm)	Measured power (W)	Calculated Bearing Lost Power (W)	Total Power (W)	TSR	C_p
382.37	-4.2459	0.1700	0.4220	0.5920	1.3349	0.0183
365.32	-27.4800	1.0513	0.4000	1.4513	1.2754	0.0449
306.47	-92.8866	2.9811	0.3280	3.3091	1.0699	0.1024
258.16	-161.9803	4.3790	0.2700	4.6490	0.9013	0.1439
227.14	-201.1165	4.7837	0.2340	5.0177	0.7930	0.1553

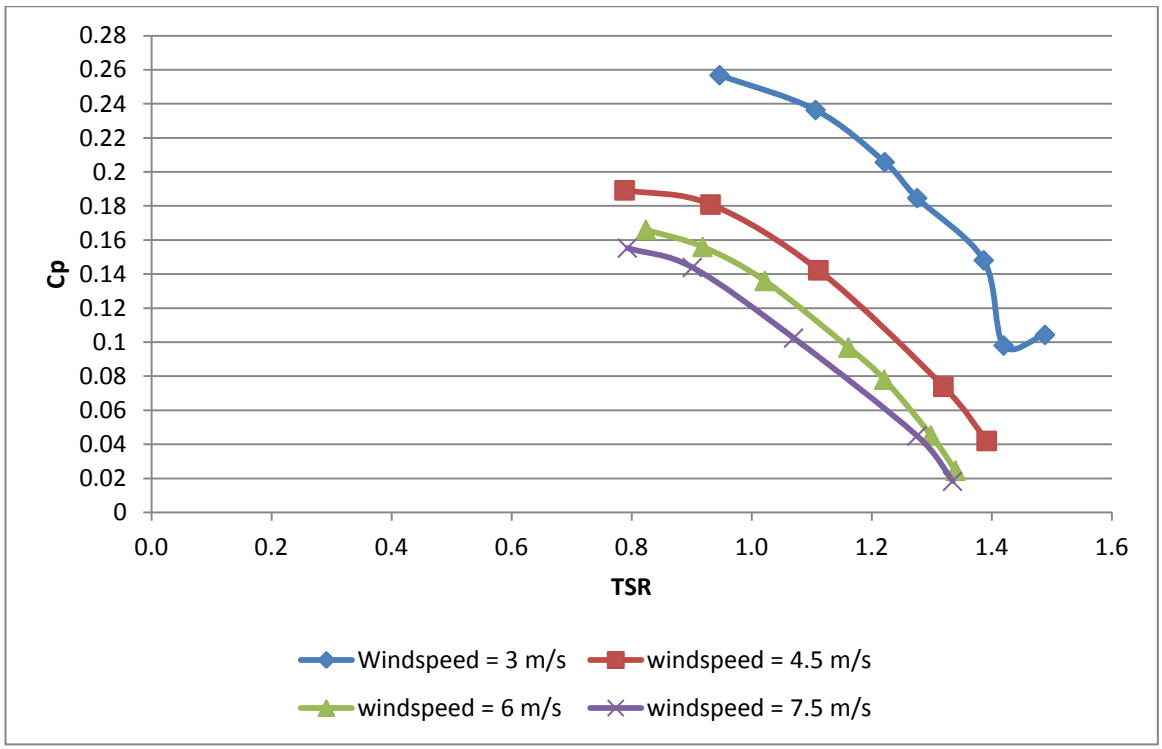

Figure 4.3: Summary of C_p versus TSR for Savonius VAWT with ODGV at various on-coming wind speed

The combined error for decreasing signal of the measured peak power value are approximately 5%, 2%, 2% and 1% for on-coming wind speed of 3 m/s, 4.5 m/s, 6 m/s and 7 m/s respectively.

4.3 Results comparison of 2 bladed Savonius VAWT with the ODGV and without the ODGV

With the application of the ODGV, it was noticed that before loading of the hysteresis brake to the VAWT, the VAWT was spinning at higher angular velocity. It means that the VAWT has more capability to couple with more load, hence producing higher power at same on-coming wind speed. The data has been further processed in graphical form, plotted in C_p versus TSR form, as below.

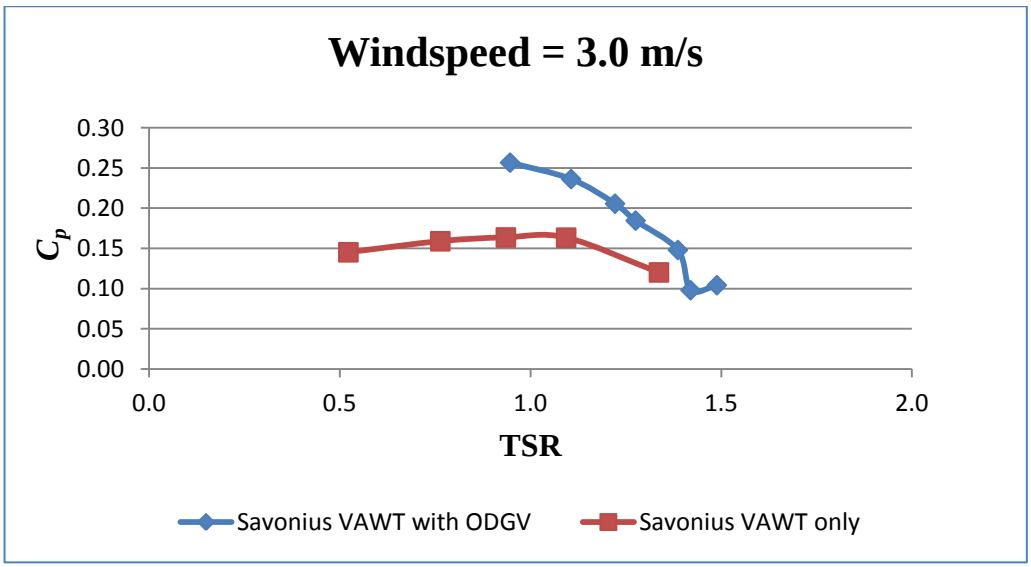

Figure 4.4: Graph of power coefficients versus TSR comparing the application of the ODGV on Savonius VAWT at 3 m/s

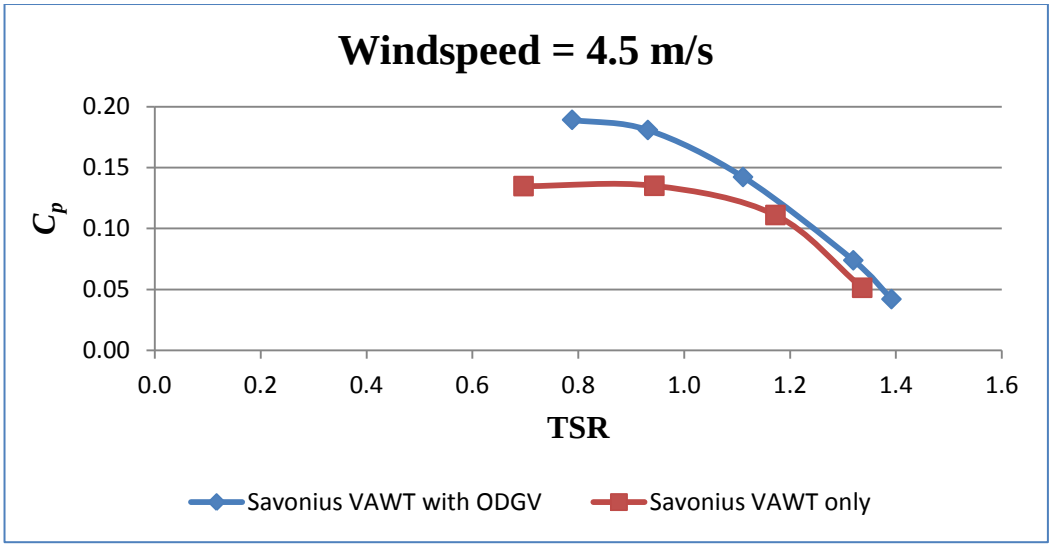

Figure 4.5: Graph power coefficients versus TSR comparing the application of the ODGV on Savonius VAWT at 4.5 m/s

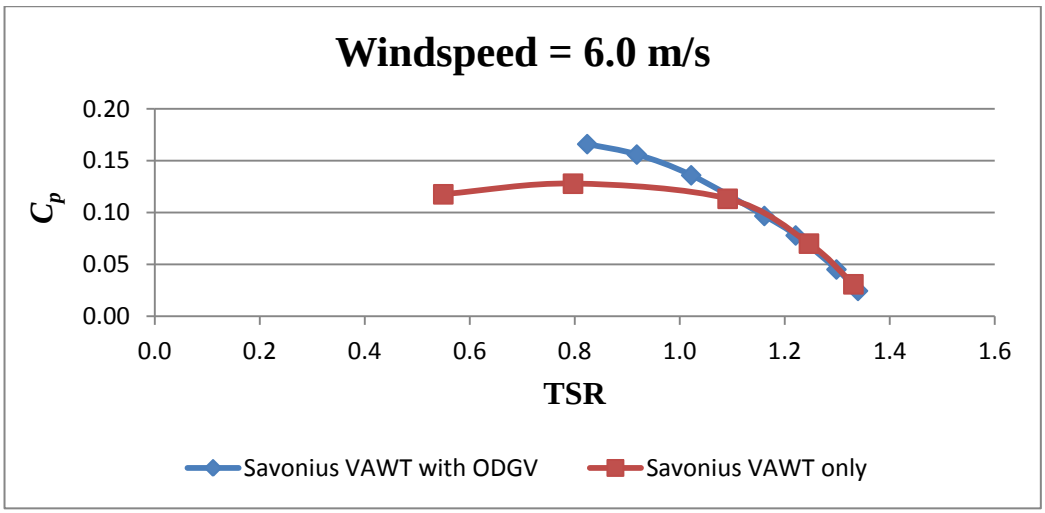

Figure 4.6: Graph of power coefficients versus TSR comparing the application of the ODGV on Savonius VAWT at 6.0 m/s

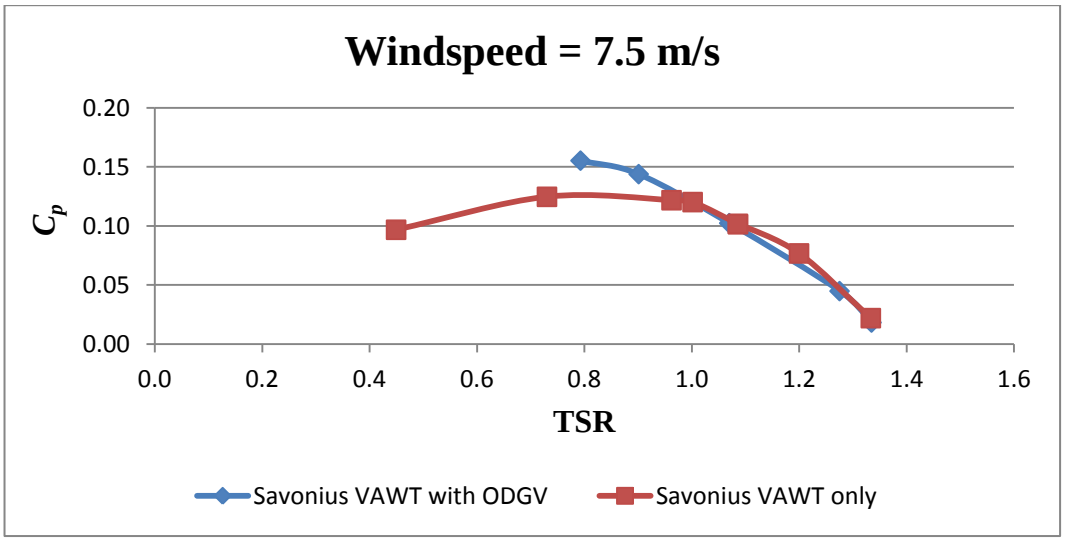

Figure 4.7: Graph power coefficients versus TSR comparing the application of the ODGV on Savonius VAWT at 7.5 m/s

Figure 4.4 through Figure 4.7 show the result as well as the effect of the application of the ODGV at different wind speed. At wind speed 3 m/s and 4.5 m/s, the effect of the application of ODGV is most noticeable. The augmentation at the peak power coefficient of Savonius VAWT with the application of ODGV is 51.36% greater than bare Savonius VAWT only. At on-coming wind speed of 4.5 m/s, the augmentation at the peak power coefficient, which is 40.10%. The power augmentations

for the wind speed from 3.0 to 7.5 m/s have been summarized in Table 4.9 and Figure 4.8. The drop in the increment of peak power coefficient is because the higher on-coming wind speed, the higher turbulent level of the on-coming wind, thus increment is decreased.

Table 4.9 Summary of peak power coefficient increment at various wind speed

Wind speed (m/s)	Increment of peak power coefficient, %
3.0	56.86
4.5	40.10
6.0	29.81
7.5	24.57

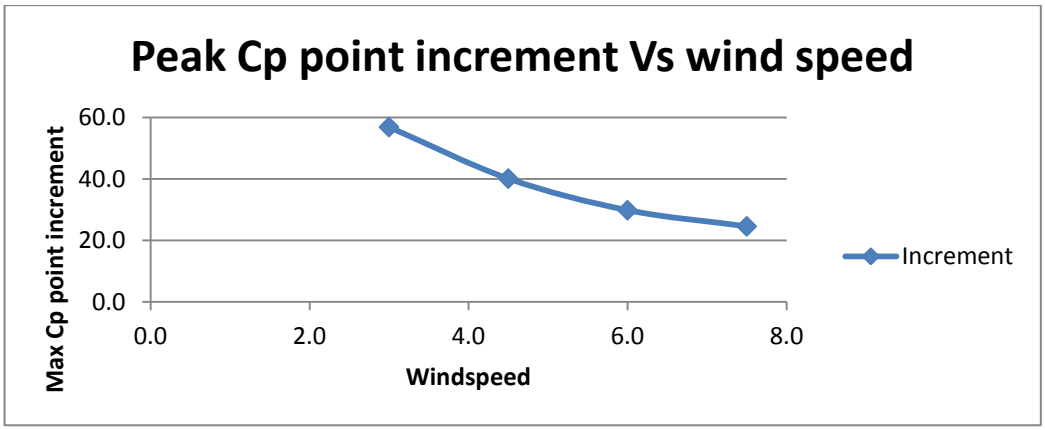

Figure 4.8: Graph of peak C_p increment versus wind speed

.

According to Soo's survey (Soo, 2008), the range of highest available wind power is from 3.0 m/s to 4.0 m/s for the typical weak wind region such as Malaysia. The increment of peak power coefficient at low wind speed could greatly increase the harvesting power of wind.

On the other hand, it is clear that the peak power increment is decreasing while wind speed is increasing. The ODGV device also has acted as the angular speed regulator to the VAWT. Referring to Table 4.4 and Table 4.9, at wind speed 7.5 m/s, the

free running RPM for case of with and without the ODGV are at almost 382 rpm. This suggests that the ODGV has acted as an angular speed (hence centripetal force) regulator which can save the cost for adding in a breaking mechanism for high wind speed condition which is usually to avoid VAWT structural failure due to strong wind. This is a very common practice in commercial small-medium wind turbine.

Furthermore, when the case of VAWT blade is fractured or failed during strong wind condition, the ODGV can serve as buffering device to reduce and absorb the impact force of flying blades for harming nearby buildings and human.

4.4 Results of CFD simulation on single bladed NACA 0015 VAWT

4.4.1 Mesh independent study

Mesh independent study had been performed for re-simulating the Oler's experiment at TSR 5.1. Table 4.10 is the summary of cell quantity and averaged coefficient of torque obtained for three different types of mesh. Mesh 1 contains 161,924 cells where Mesh 2 and Mesh 3 contain 209,554 and 250,658 cells respectively. The difference between averaged coefficient of torque, $C_{\tau_{avg}}$ for Mesh 2 and Mesh 3 is 0.2756%. As a result, Mesh 2 has been chosen for the rest of simulations for saving time and computational cost consideration.

Table 4.10: Cell quantity and averaged $C\tau$ of different mesh type

Zone	**Cell Quantity**		
	Mesh 1	**Mesh 2**	**Mesh 3**
Water tunnel	28,177	31,852	30,630
Rotary maingrid	74,844	92,133	95,711
Rotary subgrid	58,903	85,569	124,317
Total	**161,924**	**209,554**	**250,658**
Averaged $C\tau$	**0.3537**	**0.3681**	**0.3691**

4.4.2 Verification of the simulation result

The torque coefficient versus azimuth angle simulation was compared to the experimental data at TSR 5.1. Generally, the simulation demonstrates good agreement pattern with the experimental data. From torque coefficient versus azimuth angle plot, the 2D simulation (Figure 4.9) has over-predicted the peak value of the torque coefficient at approximately, azimuth angle of 120 °. A 2D analytical model based on the Oler's experimental parameters had also been carried out by Deglaire *et al*. (2009) by using conformal mapping techniques and Laurent's series decomposition. It is reported that the over prediction is due to

(i) Low Reynolds number consideration, which not only increases the drag but also significantly decreases the lift. Hence the power extracted from the upwind pass is too high and the speed is too much reduced in the downwind pass inducing simulated normal forces that are too low.

(ii) Low aspect ratio of blade used in the experiment by Oler *et al.* and might suggest a 3D influence.

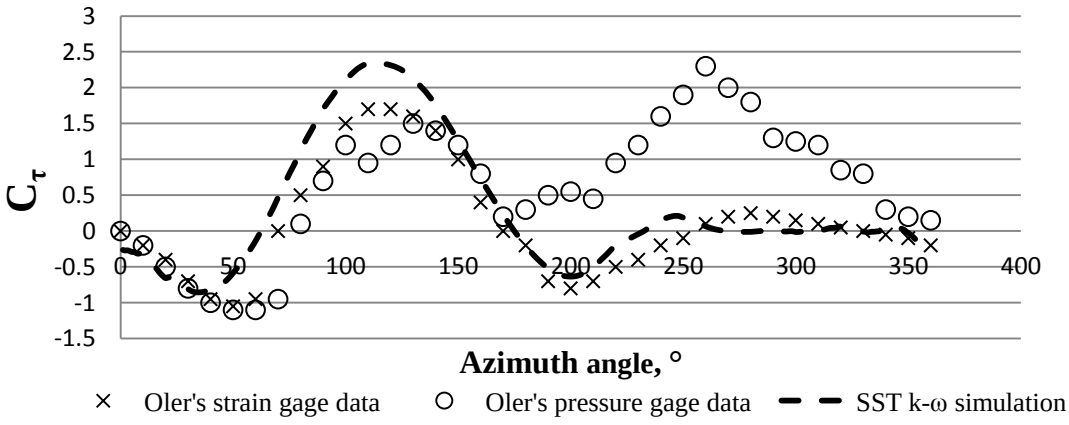

Figure 4.9**:** Comparison of the torque coefficient versus azimuth angle between Oler's experimental data and simulation data at TSR 5.1

4.4.3 Simulation results – comparison with and without presence of the ODGV

The main purpose of this simulation is to investigate the effect of the ODGV when applies to NACA 0015 VAWT. With the ODGV, at TSR 5.1, the averaged torque coefficient of the NACA 0015 single-bladed VAWT has been increased 38.62%, which having a value of 0.4195, whereas without the ODGV, the averaged torque coefficient of the VAWT is only 0.3681. Figure 4.10 is the torque coefficient history versus azimuth angle for a complete cycle for the single bladed NACA 0015 VAWT at TSR 5.1, it is clearly seen that positive torque has been gained at azimuth angle from 1 ° to 100 °, 130 ° to 140 °, 190 ° to 210 ° and also from 260 ° to 300 °. Figure 4.11 shows the velocity contour around NACA 0015 airfoil VAWT without the ODGV at azimuth 0 ° and Figure 4.12 shows velocity contour for the VAWT with the ODGV.

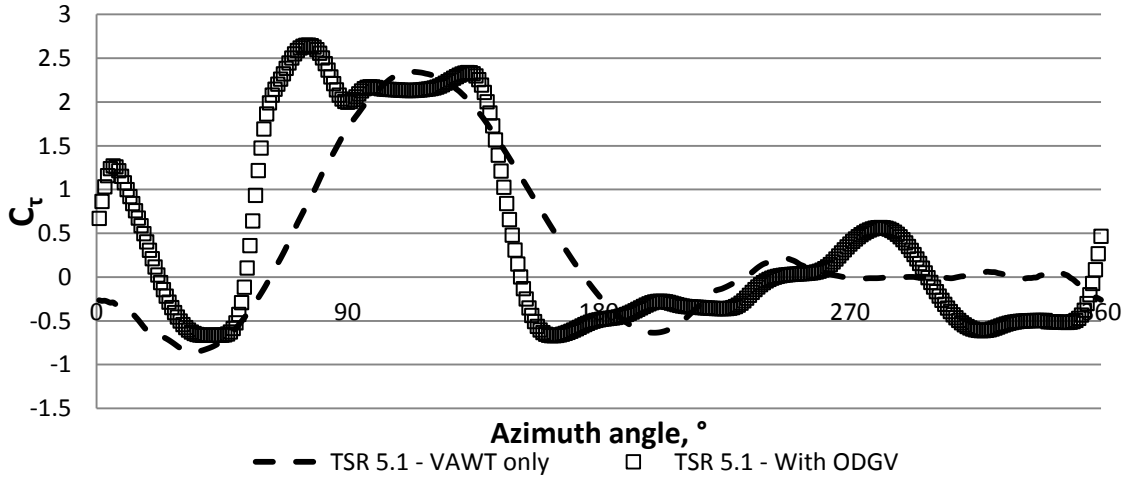

Figure 4.10: Comparison of the effects of the ODGV on NACA 0015 single bladed VAWT at TSR 5.1

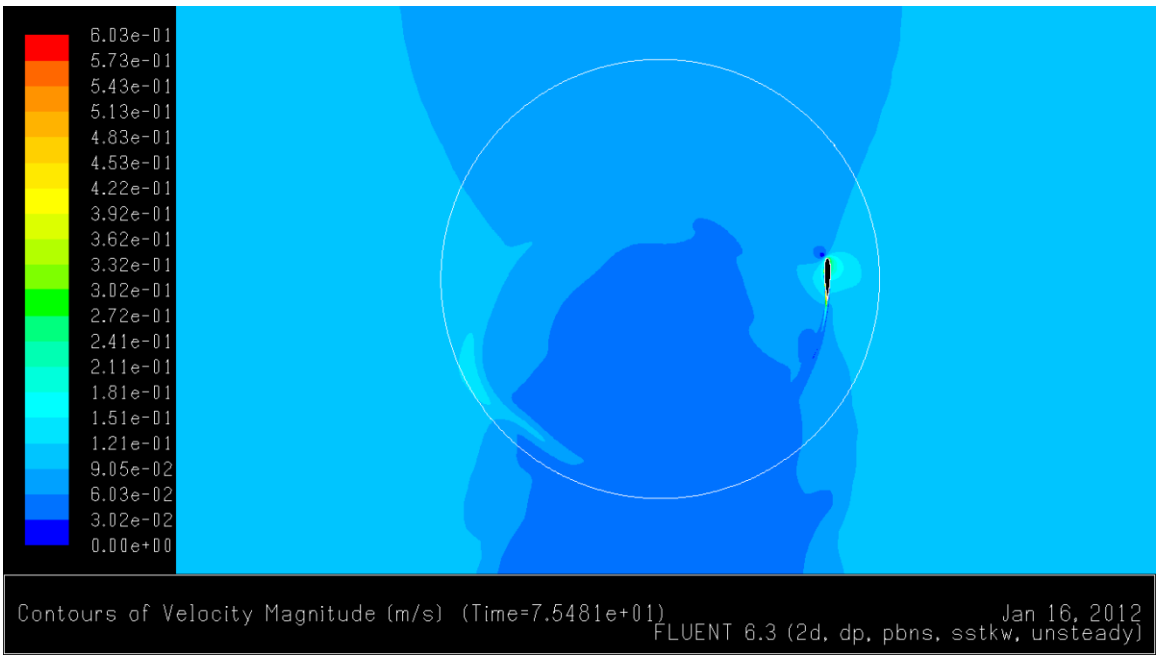

Figure 4.11: Velocity contour around NACA 0015 airfoil VAWT without ODGV at azimuth 0 °(TSR 5.1)

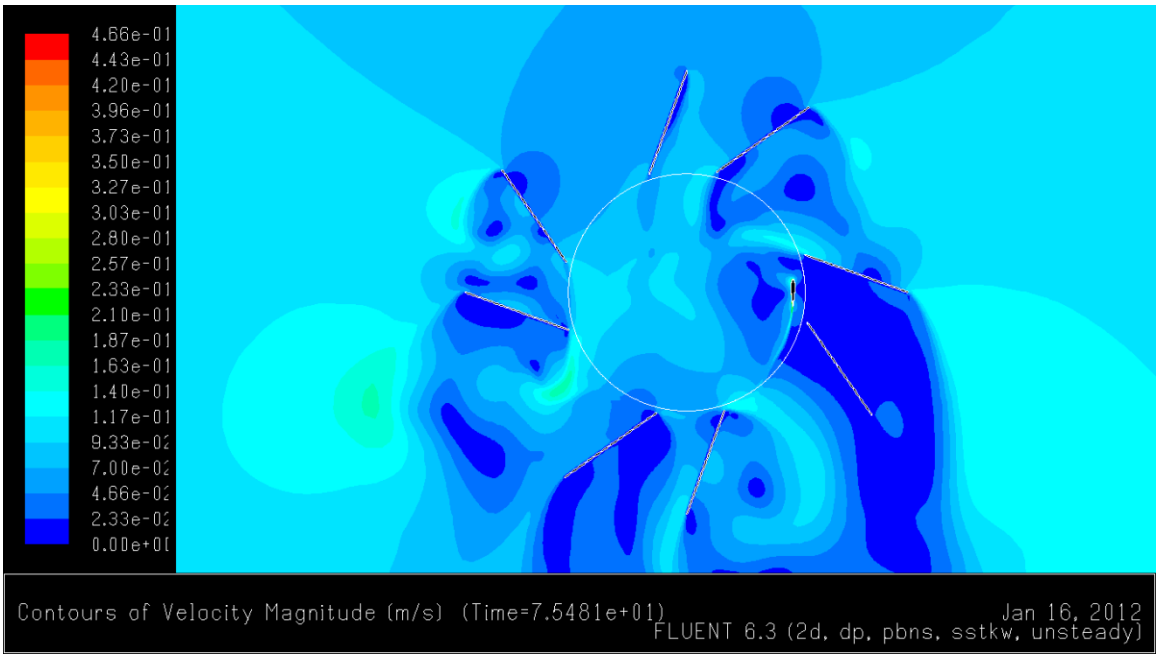

Figure 4.12: Velocity contour around NACA 0015 airfoil VAWT with the ODGV at azimuth 0 °(TSR 5.1)

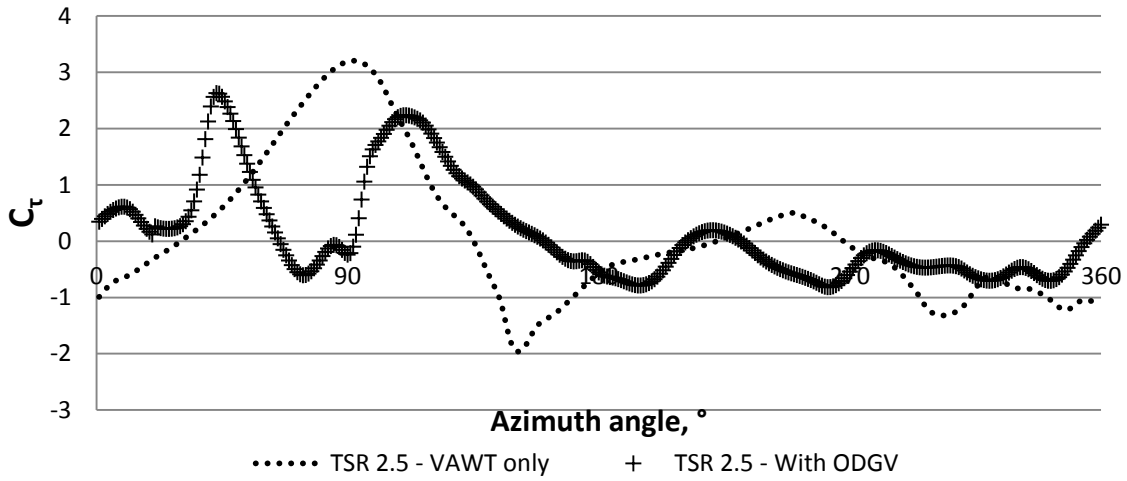

Figure 4.13: Comparison of the effects of the ODGV on NACA 0015 single bladed VAWT at TSR 2.5

As per Figure 4.13, at TSR 2.5, the VAWT with ODGV gain positive torque value at azimuth angle 0 ° to 55 °, 110 ° to 180 ° and 330 ° to 360 °. The averaged torque coefficient has been increased from 0.0902 to 0.1421, which the increment is 57.50%. Figure 4.14 shows the velocity contour around NACA 0015 airfoil VAWT without the ODGV at azimuth 0 ° and Figure 4.15 shows velocity contour for the VAWT with the ODGV.

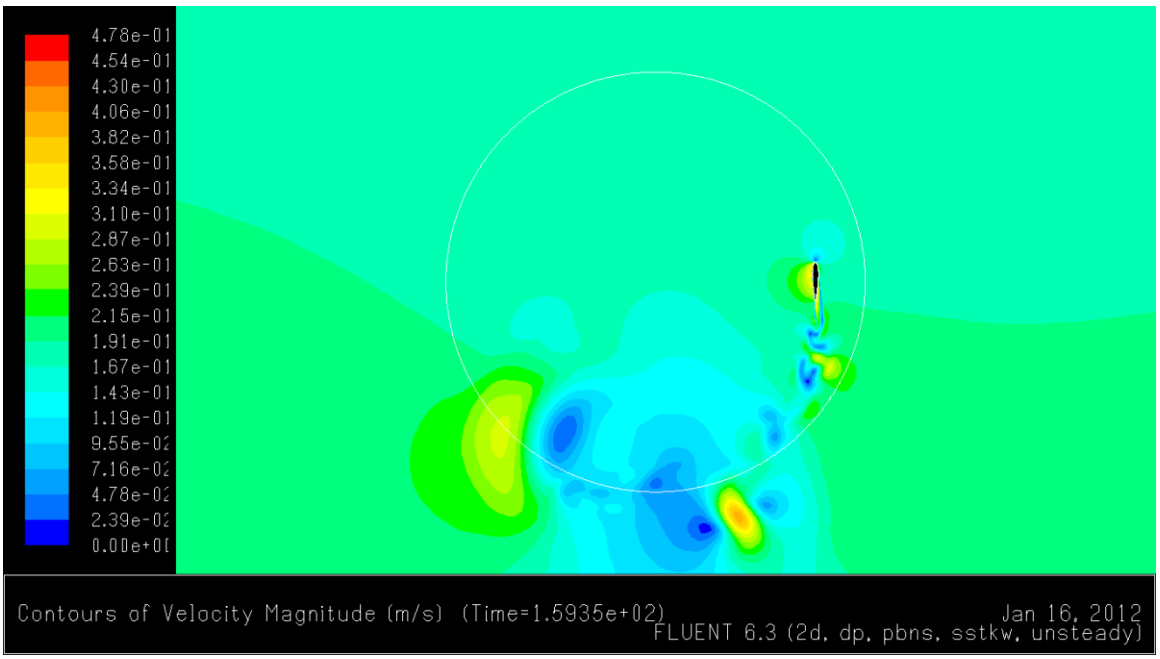

Figure 4.14: Velocity contour around NACA 0015 airfoil VAWT without the ODGV at azimuth 0 ° (TSR 2.5)

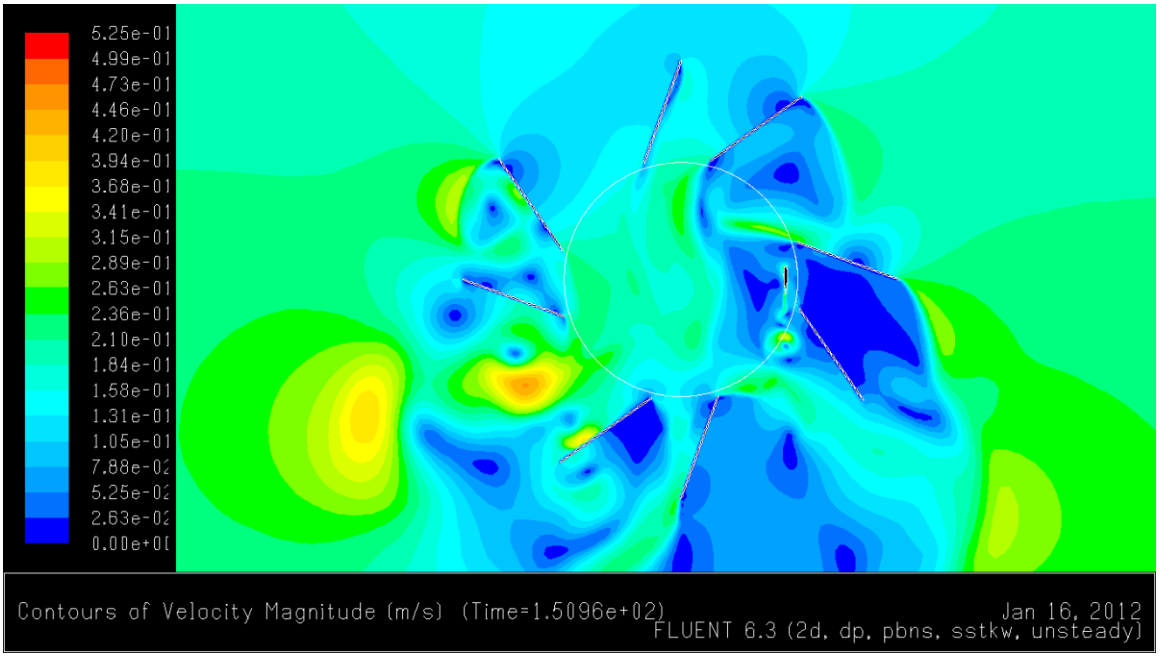

Figure 4.15: Velocity contour around NACA 0015 airfoil VAWT with the ODGV at azimuth 0 °(TSR 2.5)

Table 4.11 shows the summary of the effect of the ODGV on averaged torque coefficient (blade) and averaged power coefficient (rotor) at different TSR.

Table 4.11: Summary of the effect of the ODGV on torque coefficient at different TSR

	C_τ avg		C_p avg	
	TSR 5.1	**TSR 2.5**	**TSR 5.1**	**TSR 2.5**
VAWT only	0.3026	0.0902	0.188997	0.028735
With ODGV	0.4195	0.1421	0.261997	0.045256
Increment of Cτ avg,v%	38.62	57.50	38.62	57.50

As a result, by augmenting the performance of the wind turbine (either drag type or lift type VAWT), ODGV can help to address low wind speed problem and encourag the site of wind turbine in weak wind region.

CHAPTER 5: Conclusions and recommendations

5.1 Conclusions

An innovative guide vane system that integrates several green and renewable energy harvesting technologies (wind-solar hybrid energy generation system and rain water collector) has been designed and introduced. The system integrates and optimizes several green technologies; including urban wind turbine, solar cell module and rain water collector. From techno-economic analysis has been carried out earlier, the technical viability of the PAGV system shows that by available technologies of wind turbine and photovoltaic panels, and by taking into account the advantages of the innovative guide vane system; this system can cover a significant portion of a building's energy demand and helps to make an independent (or semi independent) building from the urban electricity grid.

Omni-Directional Guide Vane (ODGV), a variation of the power-augmentation-guide-vane, which surrounds a VAWT (both drag type and lift type), was designed to improve the wind rotor performance. The shrouded design of the ODGV is recommended for urban high rise application. It can minimize the public concerns of installing a high-speed rotating wind turbine in urbanized area and also could be integrated into the building without negative visual impact and public concern.

From the experimental measurements, the ODGV is capable to augment the power output of a Savonius rotor. With the presence of the ODGV, at wind speed of 3 m/s, the power coefficient of the Savonius rotor is 0.2569 whereas without the ODGV is 0.1637, which the peak power magnificent is 1.56 times greater. At wind speed of 4.5

m/s, the power coefficient of the Savonius rotor is 0.1893 whereas without the ODGV is 0.1184, which the peak power magnificent is 1.4 times greater. At wind speed of 6 m/s, the power coefficient of the Savonius rotor is 0.1661 whereas without the ODGV is 0.1279, which the peak power magnificent is approximately 1.30 times greater and at wind speed of 7.5 m/s, the power coefficient of the Savonius rotor is 0.1553 whereas without the ODGV is 0.1247, which the peak power magnificent is 1.25 times greater.

The extension of the study, the CFD simulation shows that the ODGV is capable to augment the power output of a single-bladed NACA 0015 VAWT. With the presence of the ODGV, the single-bladed VAWT has been increased by 57.50% and 38.62% at TSR 2.5 and TSR 5.1 respectively.

As a conclusion, by augmenting the performance of the wind turbine (either drag type or lift type VAWT), ODGV can help to address low wind speed problem and encouraging the site of wind turbine in weak wind region. The long-term goal is the proliferation of wind and solar energy applications in populated urban areas or sub-urban regions, capable of supplying supplementary power to urban buildings.

5.2 Recommendations

In this study, the capability of the ODGV to improve the performance of VAWT has been shown. However, there are more to be doned and studied to further optimize the ODGV such as:

- Study the vane geometry or vane arrangement of the ODGV, for example, the vane to be designed in more aerodynamic profile to minimize friction lost or the angle of vane to be fine tuned for optimizing the performance of a VAWT

- To study and perform the experiment of the VAWT and the ODGV in bigger size, hence mechanical lost such bearing friction and measurement error could be minimum
- To simulate the CFD simulation in 3D which need more computational time and resources (parallel computing)
- The simulation to be done in LES model instead of RANS model, which LES model always provides more accurate result than RANS model, but in cons, LES model needs finer mesh and also requires much more computing resources

REFERENCES

Altan, B.D. and Atilgan, M. (2010). The use of a curtain design to increase the performance level of a Savonius wind rotors. *Renewable Energy*, 35, 821-29.

Bahaj, A. S., Myers, L. & James, P.A.B. (2007*).* Urban energy generation: influence of micro wind turbine output on electricity consumption in buildings. *Energy and Buildings*, 39(2), 154-165.

Bet, F. and Grassmann, H. (2003). Upgrading conventional wind turbines, *Renewable Energy*, 28, 71-78.

Campbell, N., Stankovic, S., Graham, M., Parkin, P., Duijvendjik, M.V. & Gruiter, T.D. (2001). Proceedings of the European Wind Energy Conference: *Wind Energy for the Built Environment (PROJECT WEB)*. Copenhagen, Denmark.

Chong, W.T., Kong Y.Y., & Tan, L.L. (2009). Wind, solar and rain harvester. *Intellectual Property Corporation of Malaysia*. Patent No. PI200090728.

Chong, W.T., Naghavi, M.S., Poh, S.C., Mahlia T.M.I, & Pan, K.C. (2011). Techno-economic analysis of a wind-solar hybrid renewable energy system with rainwater collection feature for urban high-rise application. *Applied Energy*, 88, 4067-77.

Dayan, E. (2006). Wind energy in buildings. *Refocus*, 7(2), 33-38.

Deglaire, P., Engblom, S., Ågren, O. & Bernhoff, H. (2009). Analytical solutions for a single blade in vertical axis turbine motion in two-dimensions. *European Journal of Mechanics B/Fluids*, 28(4), 506-20.

Eke, R., Kara, O. & Ulgen, K. (2005). Optimization of a wind/PV hybrid power generation system. *International Journal of Green Energy*, 2, 57-53.

Eriksson, S., Bernhoff, H. & Leijon, M. (2008). Evaluation of different turbine concepts for wind power, *Renewable & Sustainable Energy Reviews*. 12(5), 1419-34.

Frankovic, B. and Vrsalovic, I. (2001). New high profitable wind turbines. *Renewable Energy*, 24(3-4), 491-99.

Fluent Inc. (2006) *Fluent User's Guide*,: U.S.A.

Grant, A., Johnstone, C. & Kelly, N. (2008). Urban wind energy conversion: the potential of ducted turbines. *Renewable Energy*, 33 (6), 1157-63.

Grassmann, H., Bet, F., Cabras, G., Ceschia, M., Cobai, D. & Delpapa, C. (2003). A partially static turbine – first experimental results. *Renewable Energy*, 28(11), 1779-85.

Govardhan, M., and Dhanasekaran, T.S. (2001). Effect of guide vanes on the performance of a self-rectifying air turbine with constant and variable chord rotors. *Renewable Energy*, 26, 201-19.

Hau, E. (2006). *Wind turbines: Fundamentals, Technologies, Application, Economics (2nd ed.).* Berlin, Germany: Springer.

Hu, S.Y. and Cheng, J.H. (2008). Innovatory designs for ducted wind turbines. *Renewable Energy*, 33(7), 1491-98.

Howell, R., Qin, N. Edwards, E. & Durrani, N. (2010). Wind tunnel and numerical study of a small vertical axis wind turbine. *Renewable Energy*, 35, 412-22.

Hwang, I.S, Lee, Y.H.,& Kim, S.J. (2009) Optimization of cycloidal water turbine and the performance improvement by individual blade control. *Applied Energy*, 86, 1532-40.

Irabu, K. and Roy, J.N. (2007). Characteristic of wind power on Savonius rotor using a guide-box tunnel. *Experimental Thermal and Fluid Science*, 32, 580-86.

Islam Mazharul, David S.-K. Ting, & Amir Fartaj, (2008). Aerodynamic models for Darrieus-type straight blade vertical axis wind turbines. *Renewable & Sustainable Energy Reviews*, 12, 1087-1109.

Kimura, Y., Onai, Y., & Ushiyama, I. (1996). *A Demonstrative Study for the Wind and Solar Hybrid Power System*. World Renewable Energy Congress, Denver, Colorado, USA.

Knight, J. (2004). Urban wind power: breezing into town. *Nature*, 430, 12-13.

Matsushima, T., Takagi, S. & Muroyama, S. (2006). Characteristics of a highly efficient propeller type small wind turbine with a diffuser, *Renewable Energy*,31, 1343-54.

Menter , F.R., Kuntz, M. & Langtry, R. (2003). *Ten Years of Industrial Experience with the* SST *Turbulence Model*. Proceedings of the Fourth International Conference on Turbulence, Heat and Mass Transfer, Begell House, Redding, CT.

Mertens, S.M, Kuik, G.V. & Bussel G.J.W. (2003). Performance of an H-Darrieus in the skewed flow on a roof, *Journal of Solar Energy Engineering*. 125 (4), 433-440.

Müller, G., Jentsch M.F., & Stoddart, E. (2009). Vertical axis resistance type wind turbines for use in buildings. *Renewable Energy* 34(5), 1407-12.

Ohya, Y., Karasudani, T., Sakurai, A., Abe, K. & Inoue, M. (2005). Development of a shrouded wind turbine with a flanged diffuser. *Journal of Wind Engineering and Industrial Aerodynamics* 96(5), 524-39.

Oppenheim, D., Owen, C. & White, G. (2004). Outside the Square: Integrating Wind into Urban Environments. *Refocus*, 5(3), 32-35.

Patankar, S.V. and Spalding, D.B. (1972). A calculation procedure for heat, mass and momentum transfer in three-dimensional parabolic flows. *Int. J. Heat Mass Transfer*, 15, 1787.

Pope,K., Rodrigues, V., Doyle, R., Tsopelas, A., Gravelsins, R., Naterer, G.F.& Tsang, E. (2009). Effects of stator vanes on power coefficients of a zephyr vertical axis wind turbine. *Applied Energy*, 35(5), 1043-51.

Sandia National Laboratories. (1974). *The vertical-axis wind turbine 'How it works'* (SAND74-0160), Albuquerque, New Mexico. : Blackwell, B.F.

Sandia National Laboratories. (1983). Dynamic stall regulation of the Darrieus Dynamic stall regulation of the Darrieus turbine, (SAND83-7029 UC-261), Albuquerque, New Mexico. : Oler, J.W., Strickland, J.H. & Graham, B.J. Im, G.H.

Soo, C.K. (2008). The design and analysis of power-augmentation-guide-vane for wind energy generation system. Unpublished final year project, University of Malaya, Kuala Lumpur.

Takao, M., Maeda, T., Kamada, Y., Oki, M. & Kuma, H. (2008). A straight-bladed vertical axis wind turbine with a directed guide vane row. *Journal of Fluid Science and Technology*, 3(3), 379-86.

Versteeg, H. K. and W. Malalasekera (2007*). An Introduction To Computational Fluid Dynamics: The Finite Volume Method*. United Kingdom, Pearson.

Wang, F., Bai, L., Fletcher, J., Whiteford, J. & Cullen, D. (2008). The methodology for aerodynamic study on a small domestic wind turbine with scoop. *Journal of Wind Engineering and Industrial Aerodynamics*, 96(1), 1-24.

White, F.M. (2005). *Fluid Mechanics (5th ed.).* U.S.A.: McGraw Hill.

Wright, A. and Firth, S. (2007). The nature of domestic electricity-loads and effects of time averaging on statistics and on-site generation calculations. *Applied Energy*, 88, 389-403.

Internet Reference:

Aerolab @ Faculty of Mechanical Engineering. Retrieved March 2 2011, from http://aerolab.fkm.utm.my/?id=TC&pid=724.

Bahrain World Trade Center. Retrieved September 29, 2010, from http://www.bahrainwtc.com/.

SKF Fictional moment-power loss of tapered roller bearing, 303002 J2 and deep groove ball bearing, 61802 . Retrieved April 28 2011, from http://www.skf.com/skf/productcatalogue/calculationsFilter;jsessionid=PeTEBvlT8B3FiBF4Q_HMa-7?lang=en&reloading=false&next=ok&windowName=hDK5eGeM51YiypO4OGDpukM_1300959330860_Calc5&action=Calc5&newlink=&calcform=form1&calc_e

xtrainfo=false&prodid=1310000302&n=158.78+&ny=2.88&Fr=0&Fa=56.1132+&myEHL=0.0020&f01Radio=0&seals=0&DW2=3.5&H=0.

APPENDIX A

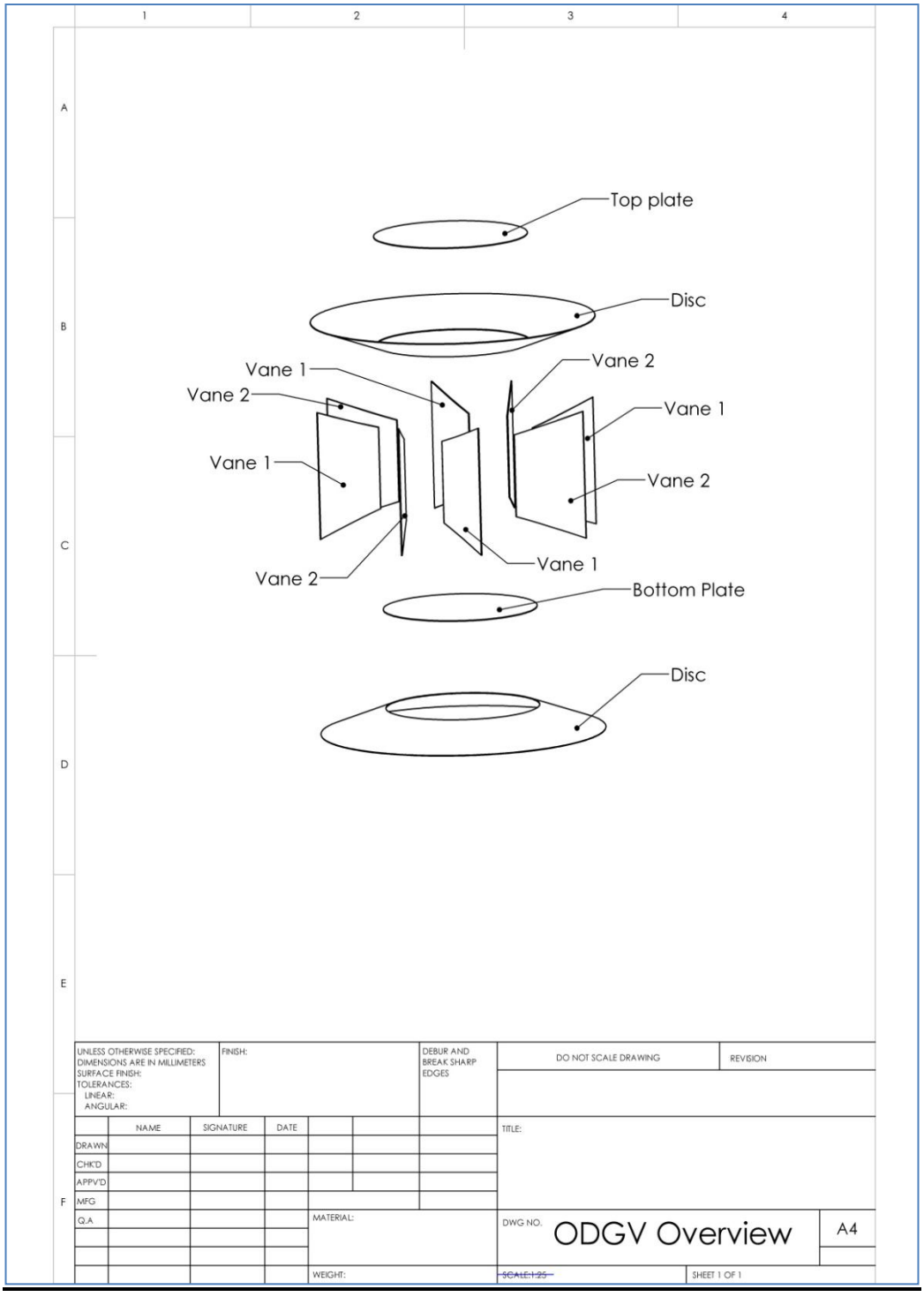

Figure A1: ODGV overview

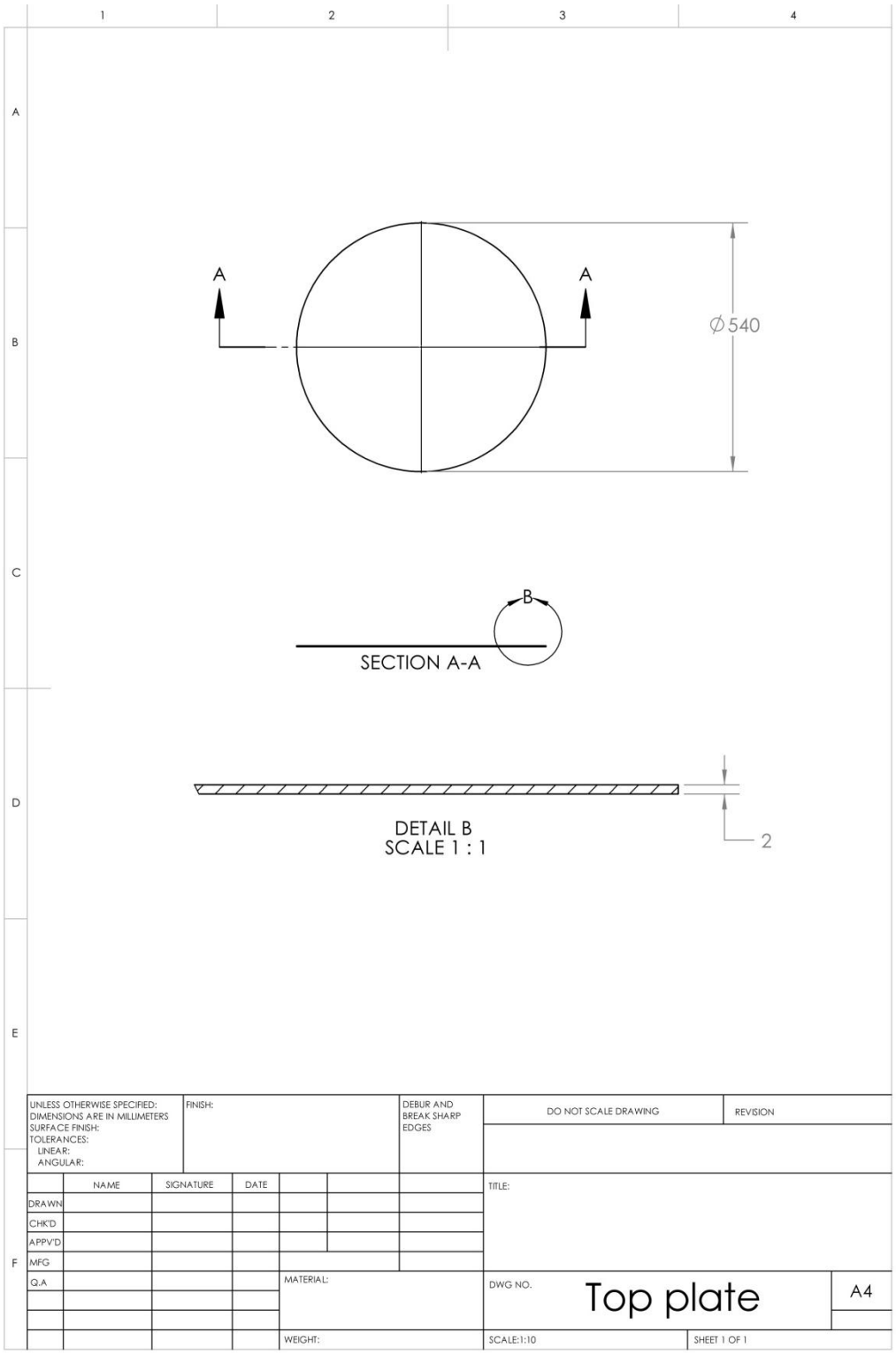

Figure A2: Top plate details

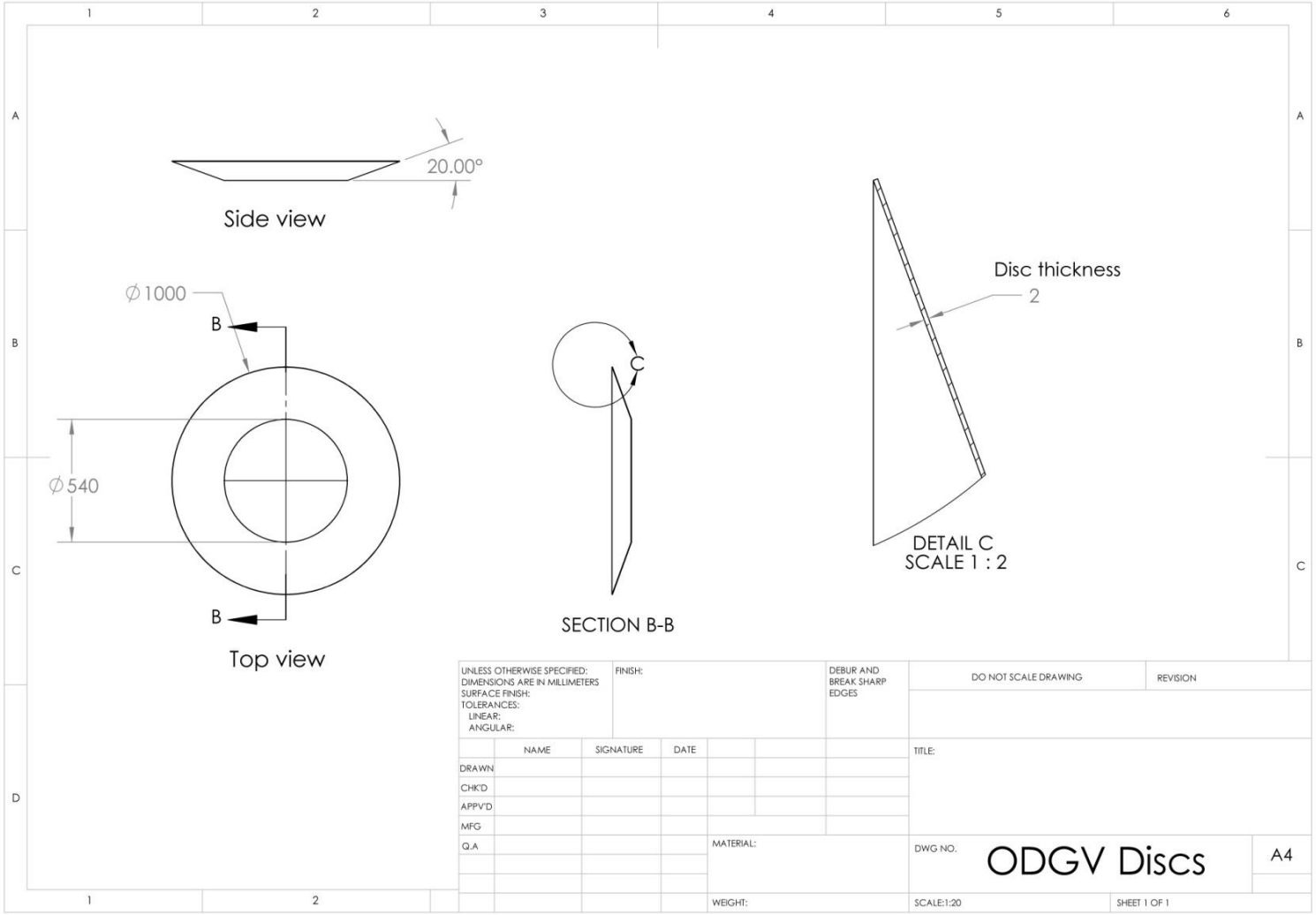

Figure A3: Details of ODGV discs

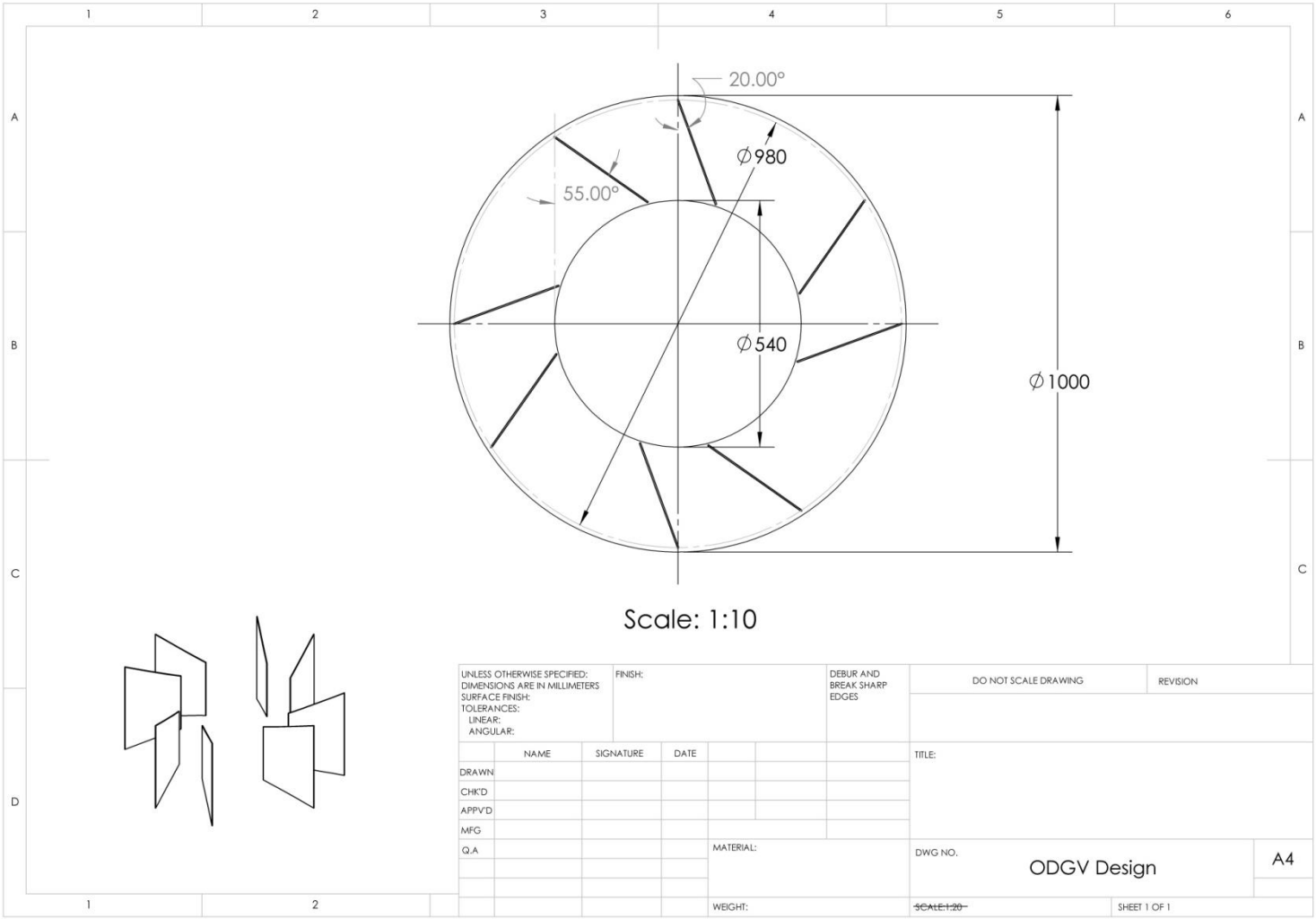

Figure A4: ODGV design

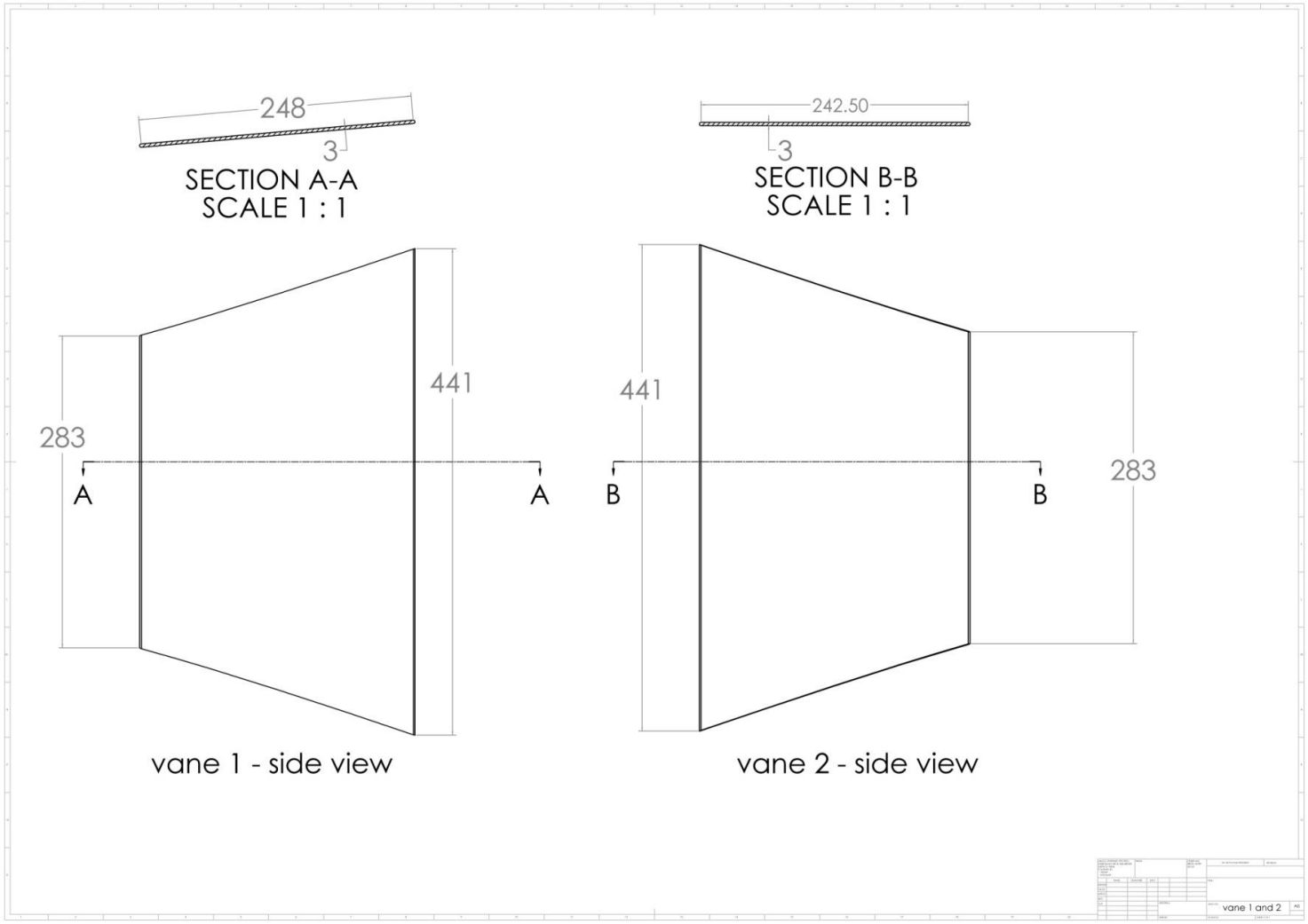

Figure A5: Details of vane 1 & vane 2

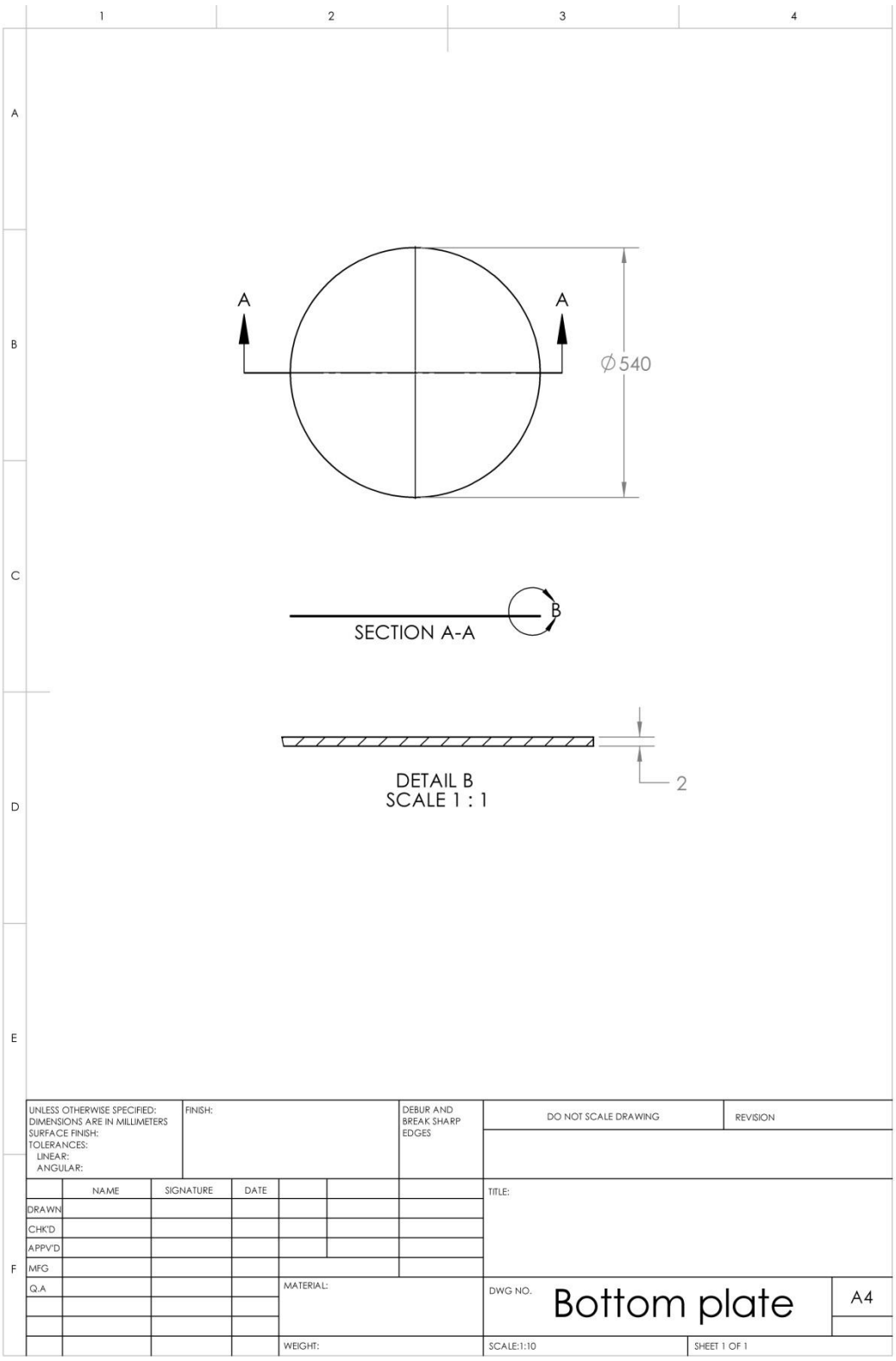

Figure A6: Bottom plate details

APPENDIX B

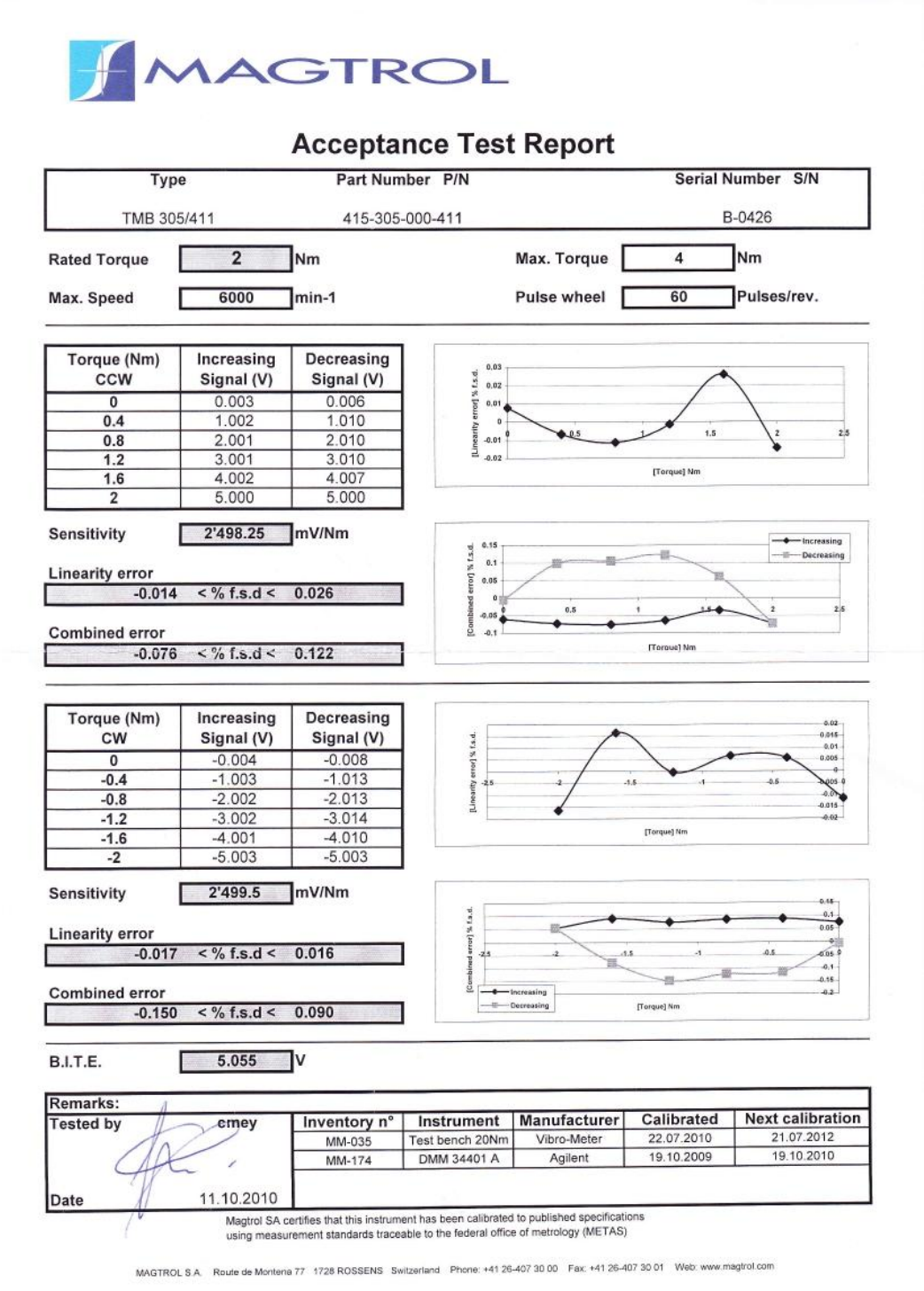

MAGTROL

Acceptance Test Report

Type	Part Number P/N	Serial Number S/N
TMB 305/411	415-305-000-411	B-0426

Rated Torque: 2 Nm — Max. Torque: 4 Nm

Max. Speed: 6000 min-1 — Pulse wheel: 60 Pulses/rev.

Torque (Nm) CCW	Increasing Signal (V)	Decreasing Signal (V)
0	0.003	0.006
0.4	1.002	1.010
0.8	2.001	2.010
1.2	3.001	3.010
1.6	4.002	4.007
2	5.000	5.000

Sensitivity: 2'498.25 mV/Nm

Linearity error: -0.014 < % f.s.d < 0.026

Combined error: -0.076 < % f.s.d < 0.122

Torque (Nm) CW	Increasing Signal (V)	Decreasing Signal (V)
0	-0.004	-0.008
-0.4	-1.003	-1.013
-0.8	-2.002	-2.013
-1.2	-3.002	-3.014
-1.6	-4.001	-4.010
-2	-5.003	-5.003

Sensitivity: 2'499.5 mV/Nm

Linearity error: -0.017 < % f.s.d < 0.016

Combined error: -0.150 < % f.s.d < 0.090

B.I.T.E. 5.055 V

Remarks:

Tested by cmey

Date 11.10.2010

Inventory n°	Instrument	Manufacturer	Calibrated	Next calibration
MM-035	Test bench 20Nm	Vibro-Meter	22.07.2010	21.07.2012
MM-174	DMM 34401 A	Agilent	19.10.2009	19.10.2010

Magtrol SA certifies that this instrument has been calibrated to published specifications using measurement standards traceable to the federal office of metrology (METAS)

MAGTROL S.A. Route de Moncria 77 1728 ROSSENS Switzerland Phone: +41 26-407 30 00 Fax: +41 26-407 30 01 Web: www.magtrol.com

Figure B1: Magtrol torque sensor TMB 305 acceptance test report

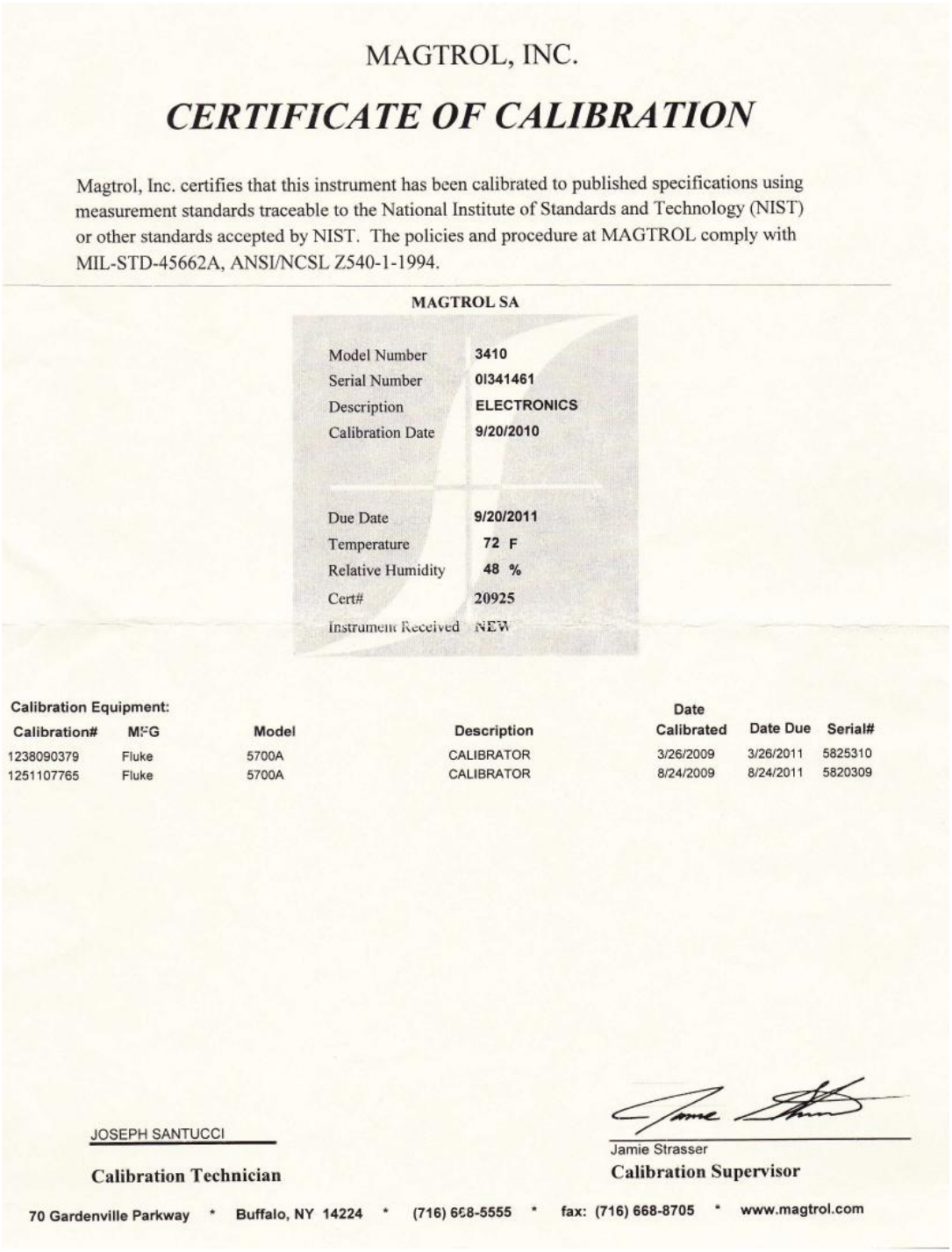

MAGTROL, INC.

CERTIFICATE OF CALIBRATION

Magtrol, Inc. certifies that this instrument has been calibrated to published specifications using measurement standards traceable to the National Institute of Standards and Technology (NIST) or other standards accepted by NIST. The policies and procedure at MAGTROL comply with MIL-STD-45662A, ANSI/NCSL Z540-1-1994.

MAGTROL SA

Model Number	3410
Serial Number	0I341461
Description	ELECTRONICS
Calibration Date	9/20/2010
Due Date	9/20/2011
Temperature	72 F
Relative Humidity	48 %
Cert#	20925
Instrument Received	NEW

Calibration Equipment:

Calibration#	MFG	Model	Description	Date Calibrated	Date Due	Serial#
1238090379	Fluke	5700A	CALIBRATOR	3/26/2009	3/26/2011	5825310
1251107765	Fluke	5700A	CALIBRATOR	8/24/2009	8/24/2011	5820309

JOSEPH SANTUCCI

Calibration Technician

Jamie Strasser

Calibration Supervisor

70 Gardenville Parkway * Buffalo, NY 14224 * (716) 668-5555 * fax: (716) 668-8705 * www.magtrol.com

Figure B2: Magtrol torque sensor TMB 305 certificate of calibration

APPENDIX C

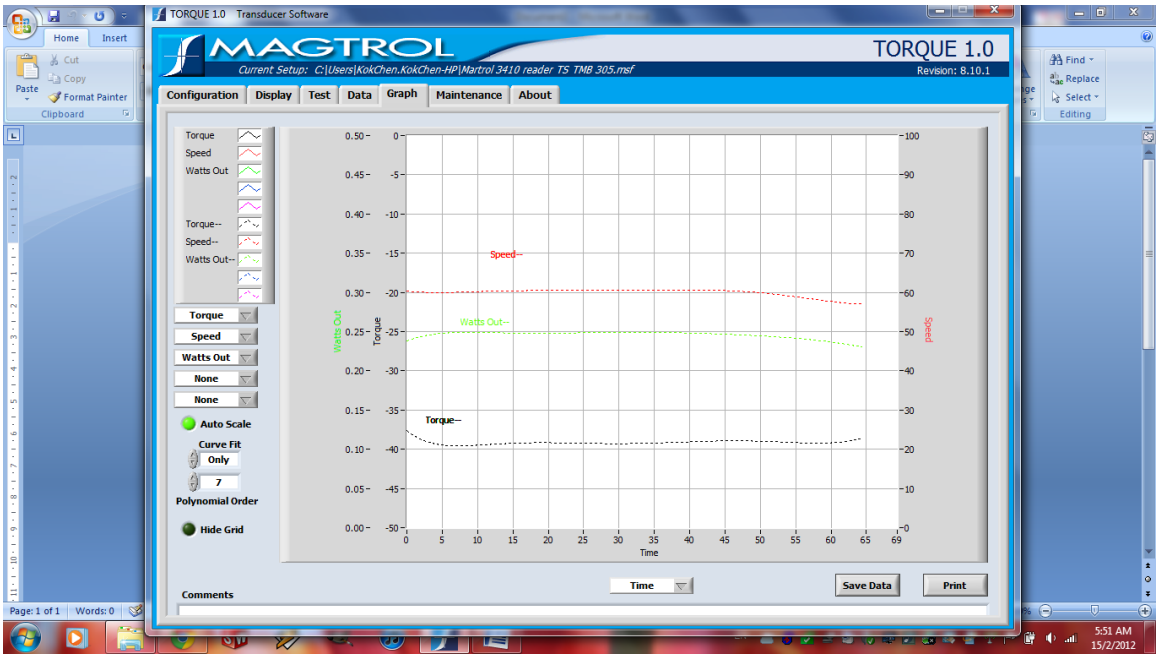

Figure C1: Print screen of the transient torque and power value of the bare 2 bladed Savonius VAWT at 59.90 rpm and on-coming wind speed of 3 m/s

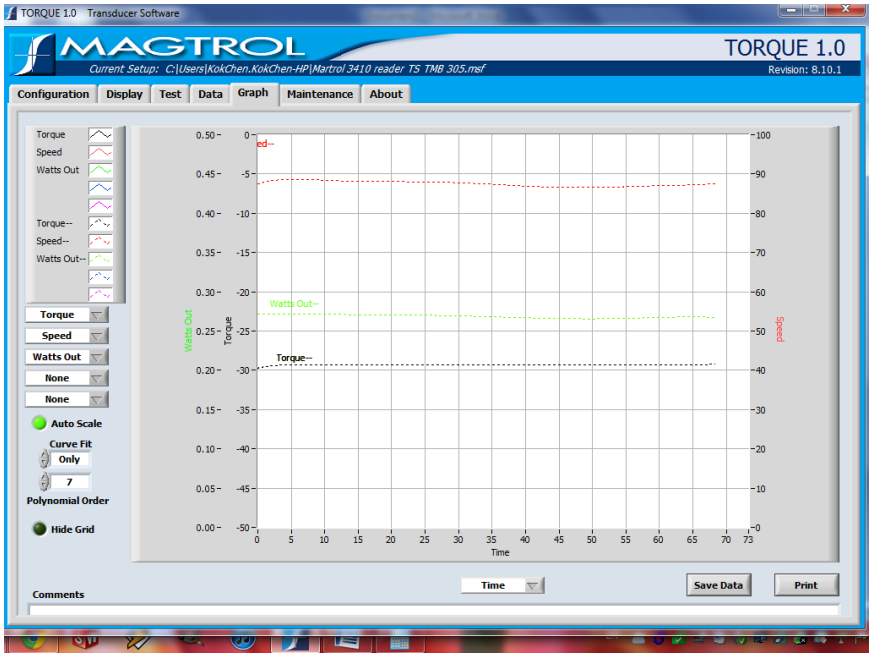

Figure C2: Print screen of the transient torque and power value of the bare 2 bladed Savonius VAWT at 87.51 rpm and on-coming wind speed of 3 m/s

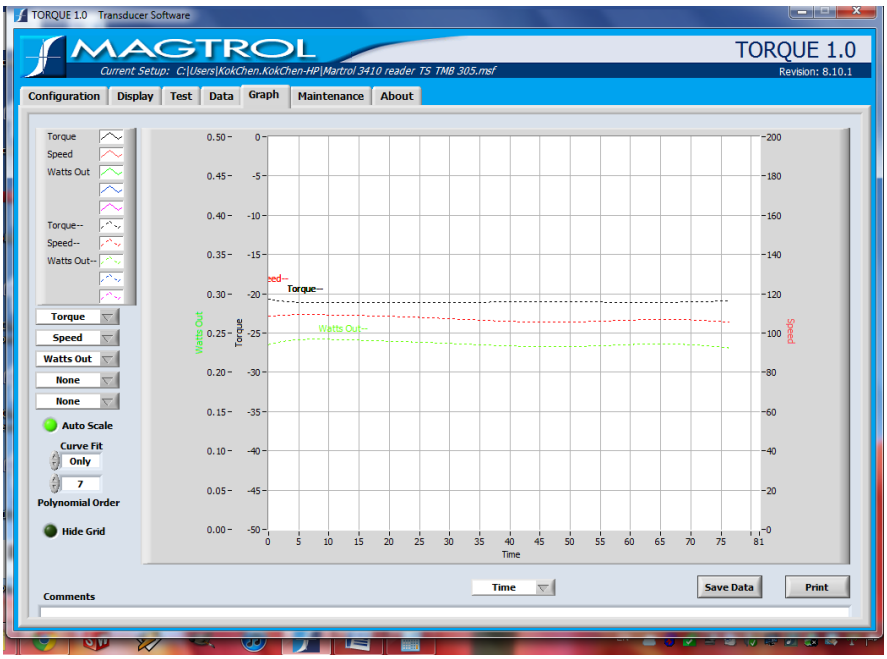

Figure C3: Print screen of the transient torque and power value of the bare 2 bladed Savonius VAWT at 107.21 rpm and on-coming wind speed of 3 m/s

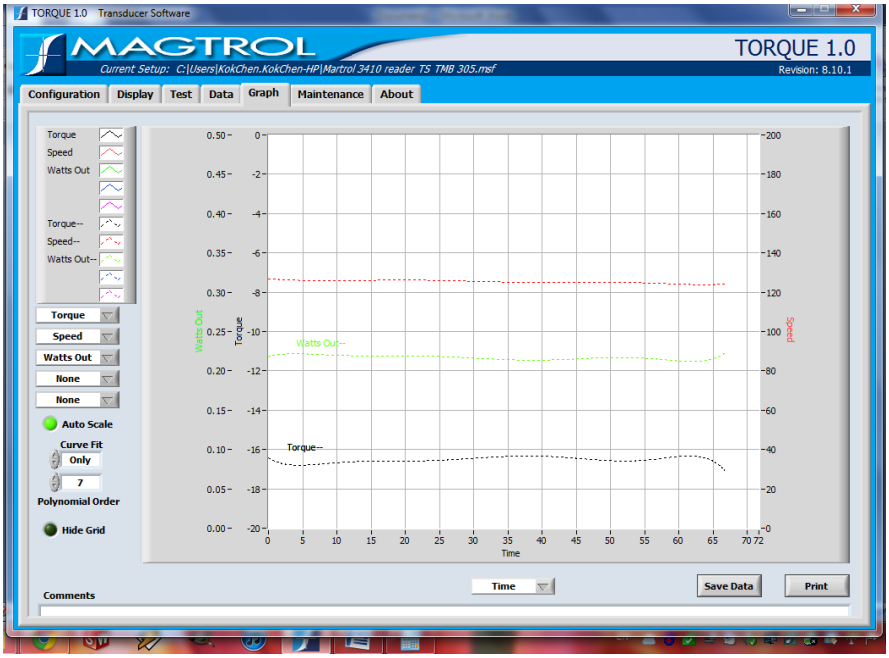

Figure C4: Print screen of the transient torque and power value of the bare 2 bladed Savonius VAWT at 125.32 rpm and on-coming wind speed of 3 m/s

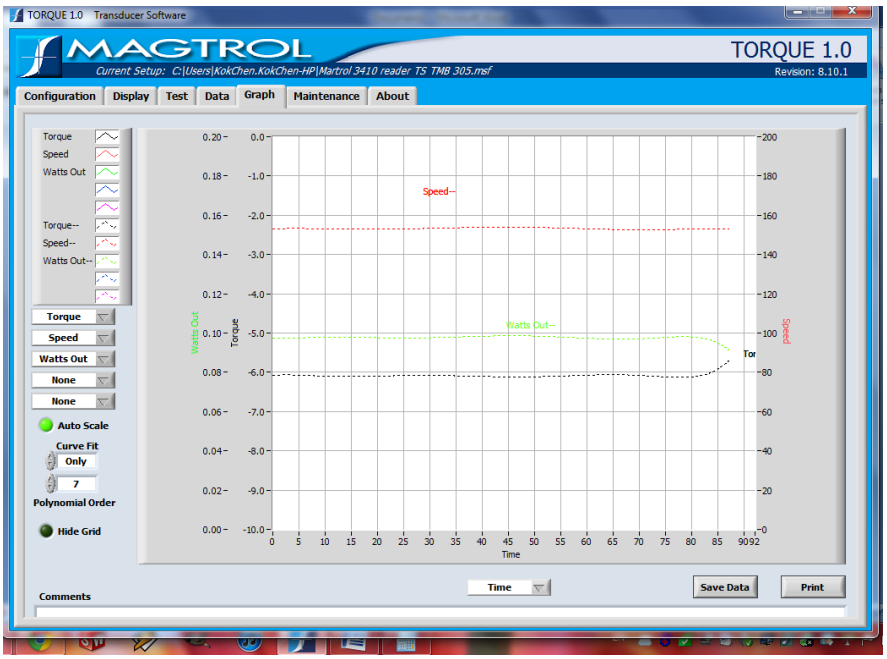

Figure C5: Print screen of the transient torque and power value of the bare 2 bladed Savonius VAWT at 153.20 rpm and on-coming wind speed of 3 m/s

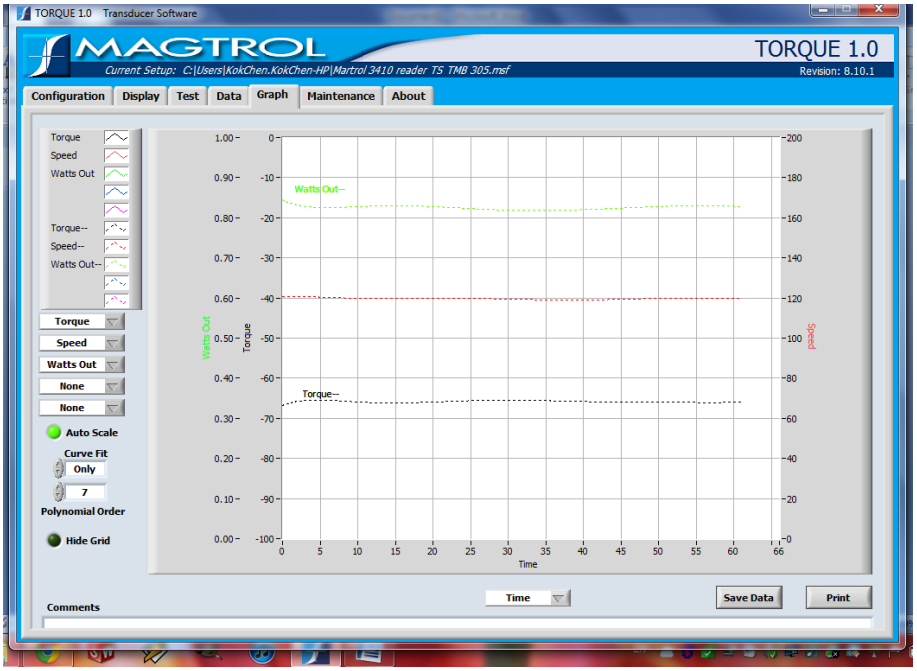

Figure C6: Print screen of the transient torque and power value of the bare 2 bladed Savonius VAWT at 119.74 rpm and on-coming wind speed of 4.5 m/s

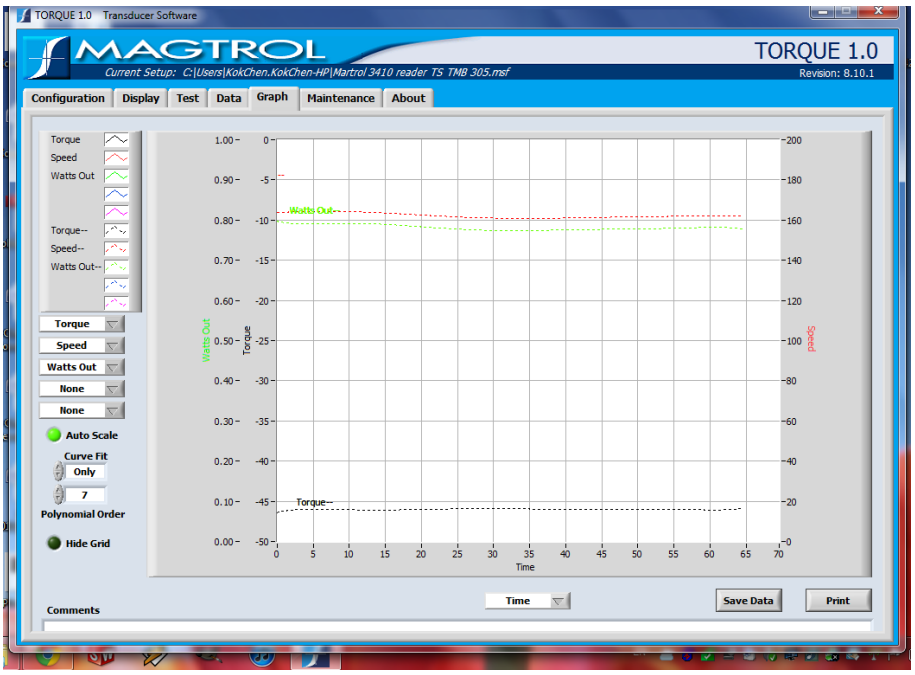

Figure C7: Print screen of the transient torque and power value of the bare 2 bladed Savonius VAWT at 162.22 rpm and on-coming wind speed of 4.5 m/s

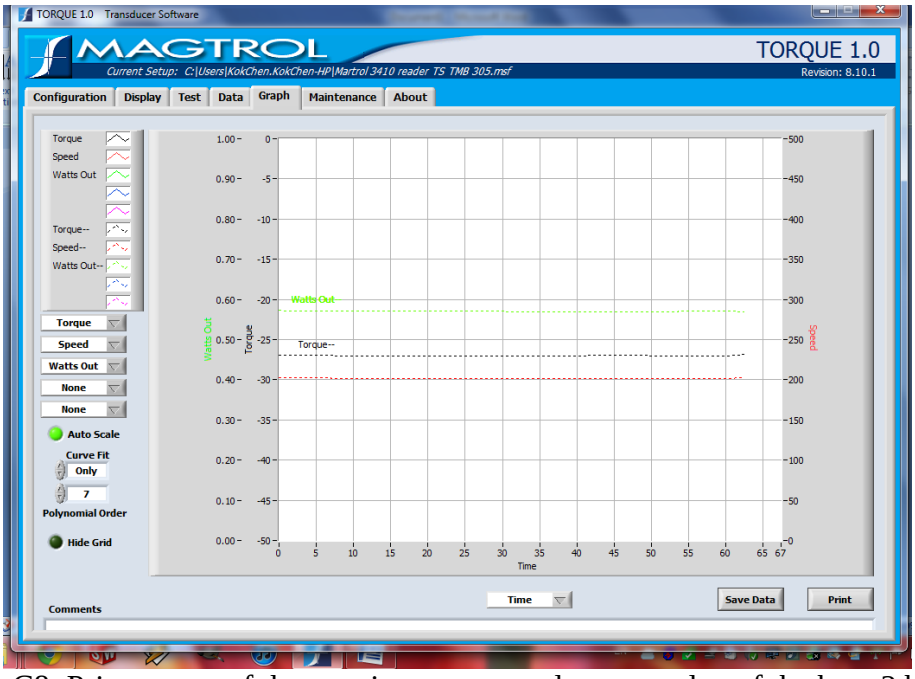

Figure C8: Print screen of the transient torque and power value of the bare 2 bladed Savonius VAWT at 201.53 rpm and on-coming wind speed of 4.5 m/s

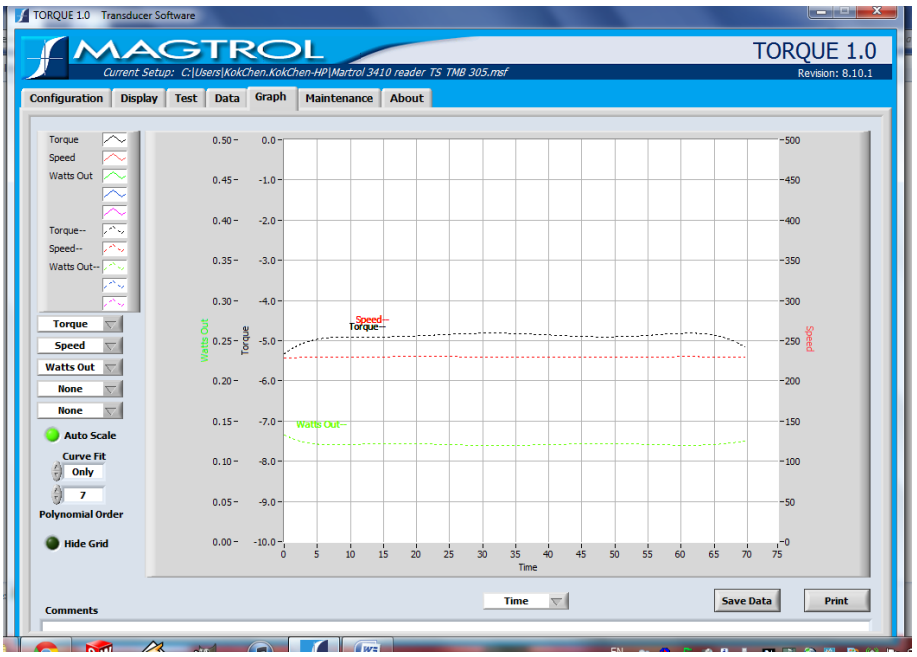

Figure C9: Print screen of the transient torque and power value of the bare 2 bladed Savonius VAWT at 229.70 rpm and on-coming wind speed of 4.5 m/s

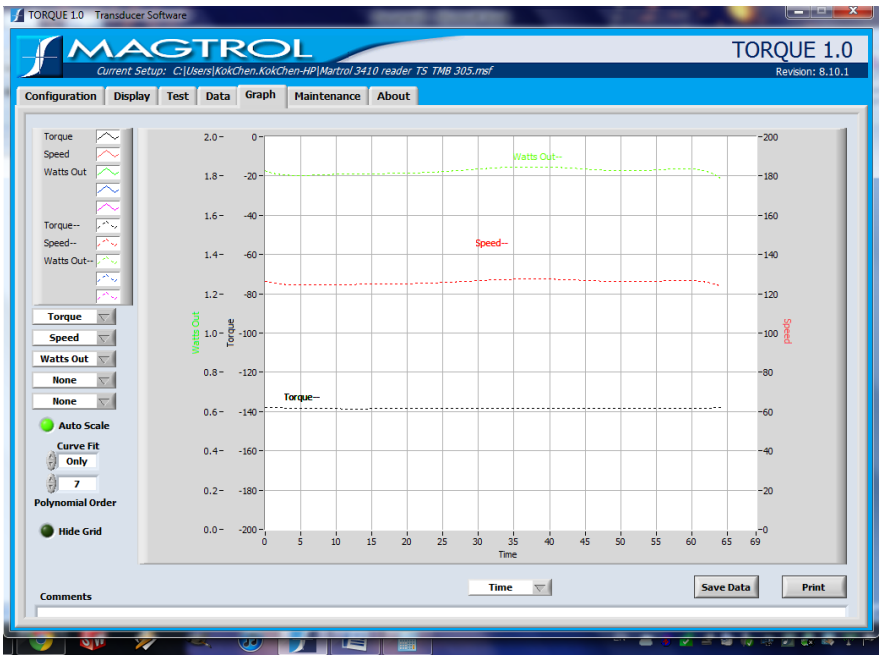

Figure C10: Print screen of the transient torque and power value of the bare 2 bladed Savonius VAWT at 125.97 rpm and on-coming wind speed of 6 m/s

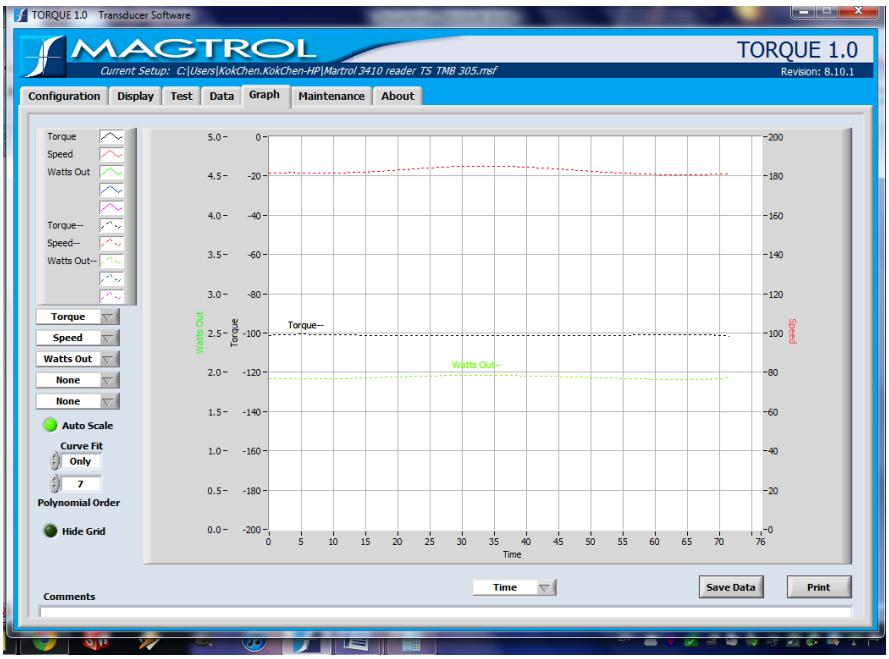

Figure C11: Print screen of the transient torque and power value of the bare 2 bladed Savonius VAWT at 182.60 rpm and on-coming wind speed of 6 m/s

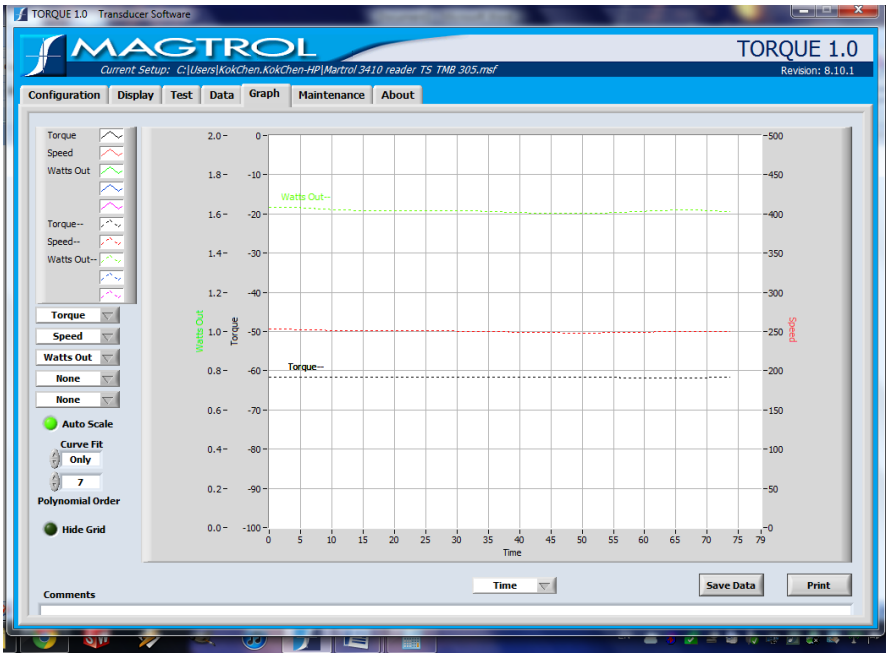

Figure C12: Print screen of the transient torque and power value of the bare 2 bladed Savonius VAWT at 250.10 rpm and on-coming wind speed of 6 m/s

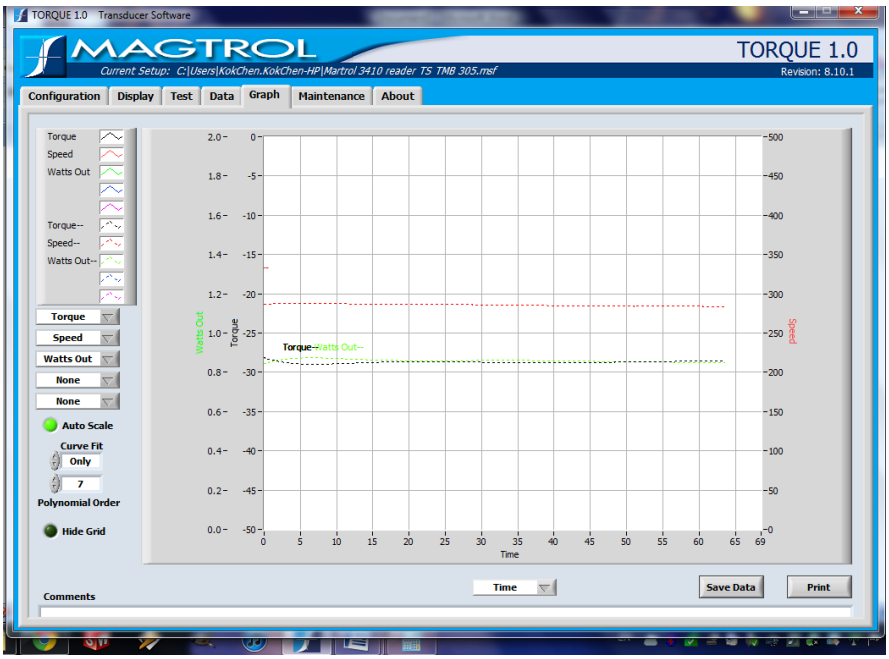

Figure C13: Print screen of the transient torque and power value of the bare 2 bladed Savonius VAWT at 285.60 rpm and on-coming wind speed of 6 m/s

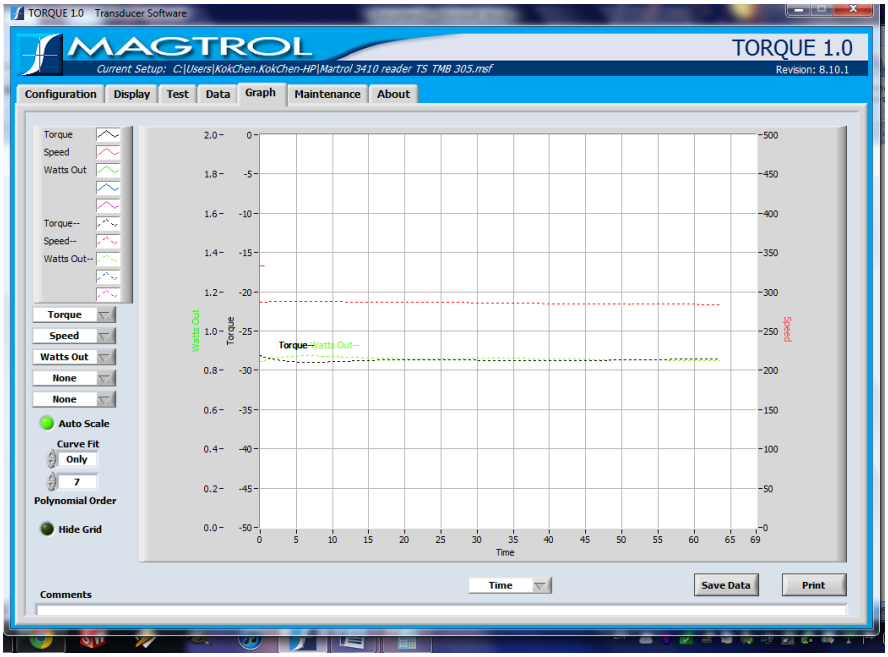

Figure C14: Print screen of the transient torque and power value of the bare 2 bladed Savonius VAWT at 305.00 rpm and on-coming wind speed of 6 m/s

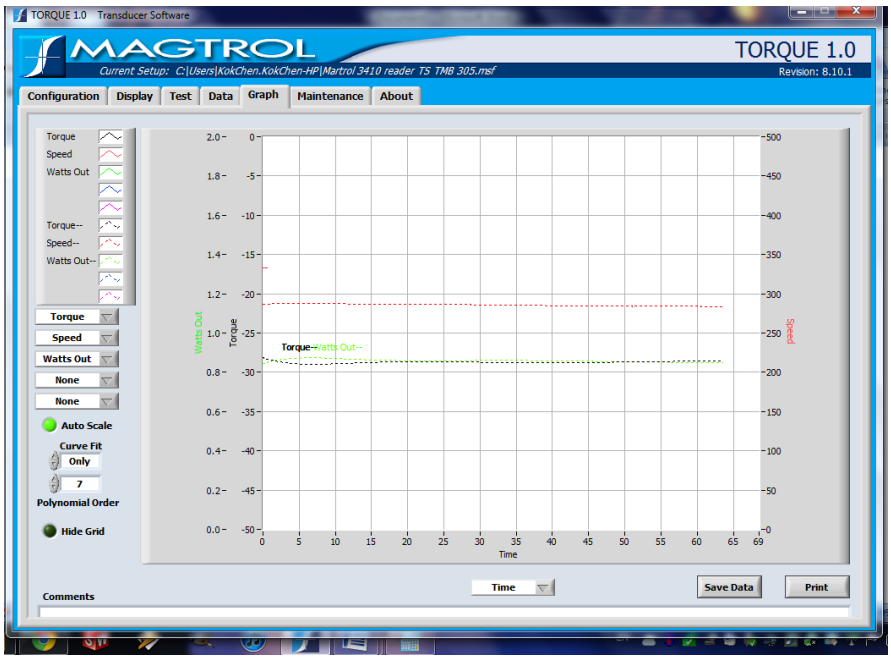

Figure C15: Print screen of the transient torque and power value of the bare 2 bladed Savonius VAWT at 128.76 rpm and on-coming wind speed of 7.5 m/s

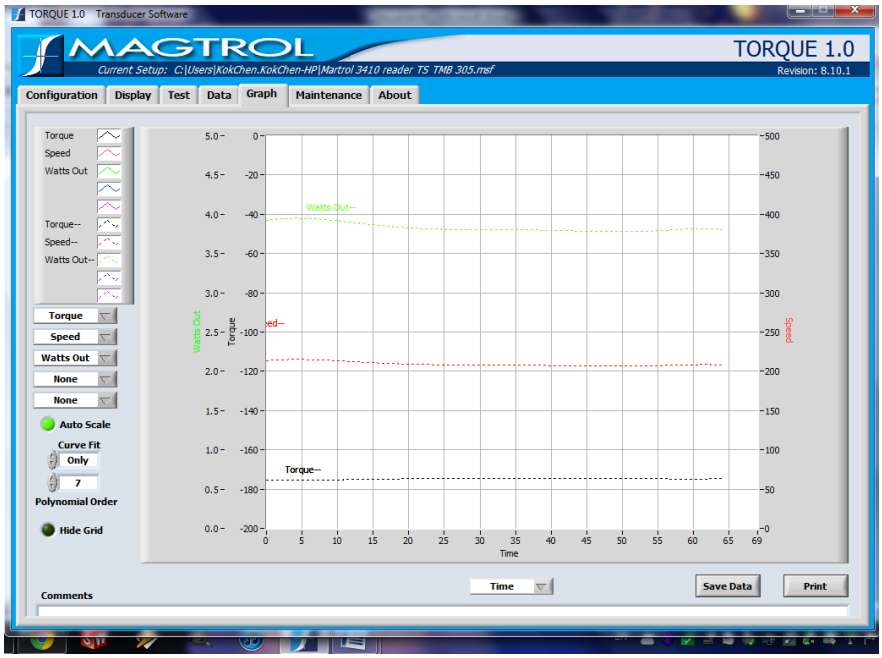

Figure C16: Print screen of the transient torque and power value of the bare 2 bladed Savonius VAWT at 209.25 rpm and on-coming wind speed of 7.5 m/s

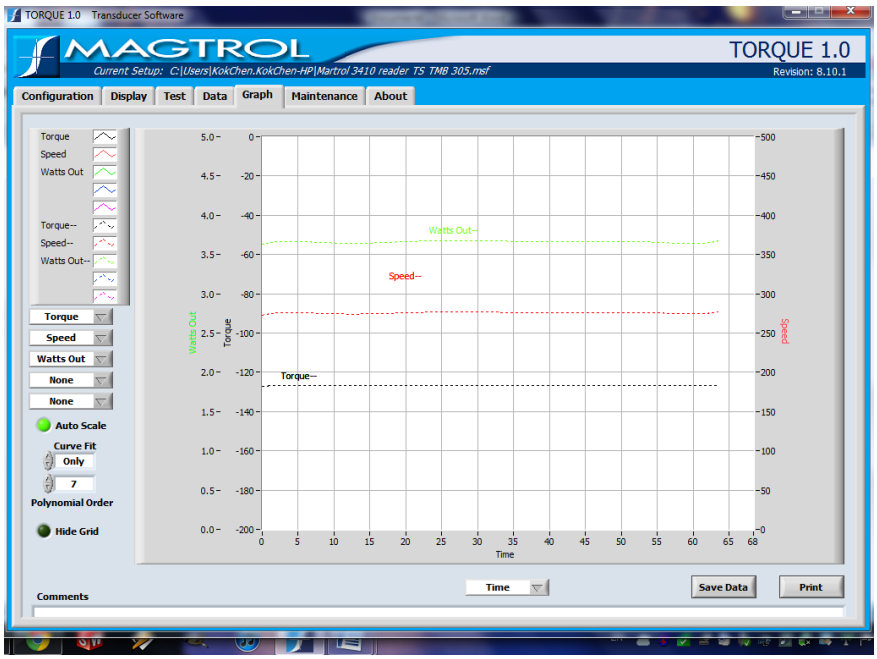

Figure C17: Print screen of the transient torque and power value of the bare 2 bladed Savonius VAWT at 275.70 rpm and on-coming wind speed of 7.5 m/s

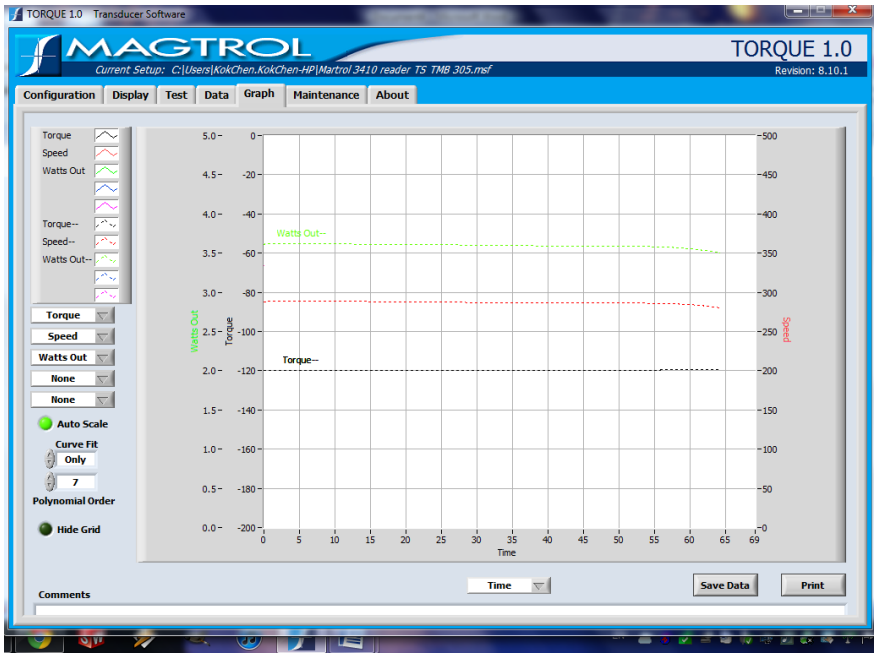

Figure C18: Print screen of the transient torque and power value of the bare 2 bladed Savonius VAWT at 286.94 rpm and on-coming wind speed of 7.5 m/s

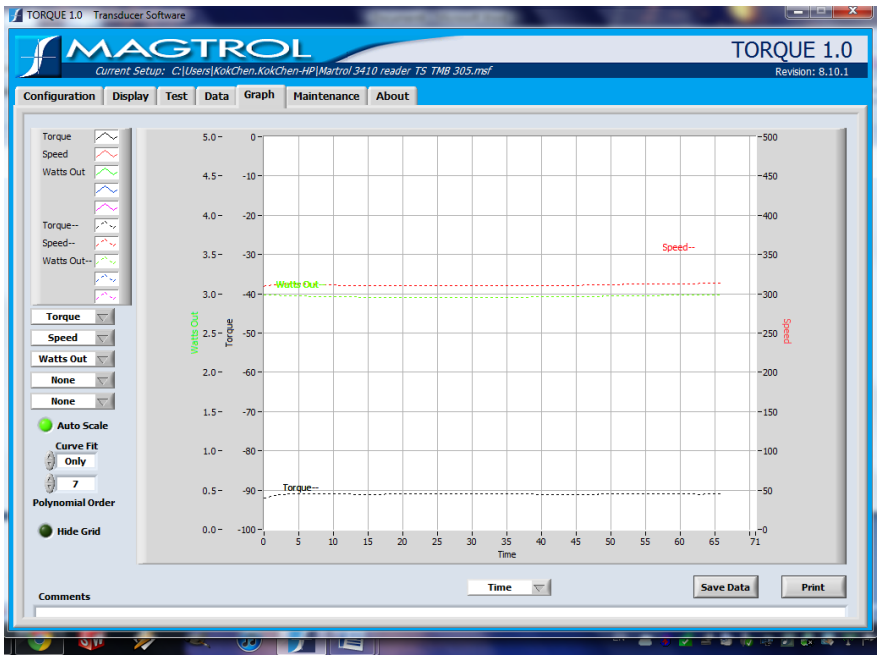

Figure C19: Print screen of the transient torque and power value of the bare 2 bladed Savonius VAWT at 311.11 rpm and on-coming wind speed of 7.5 m/s

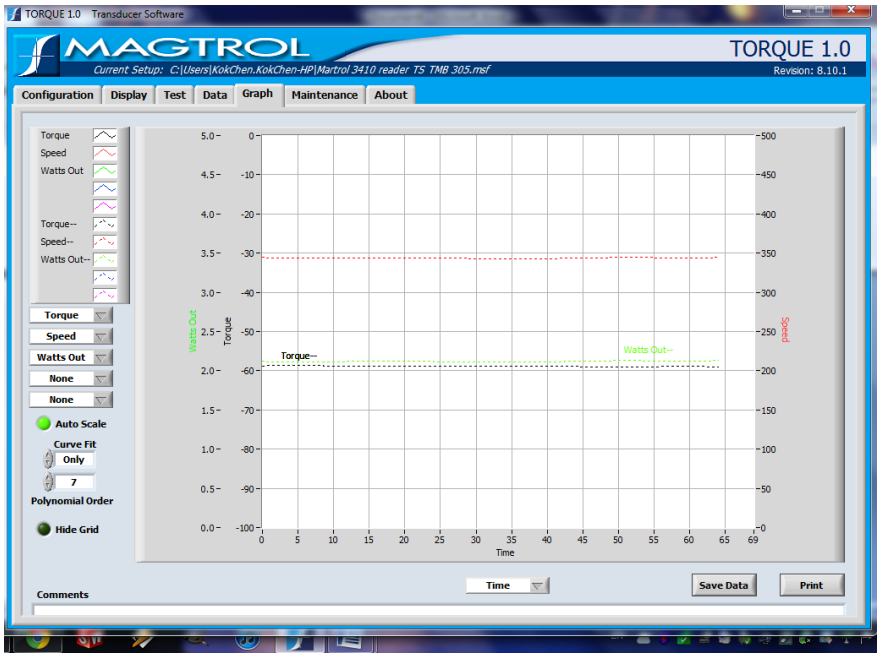

Figure C20: Print screen of the transient torque and power value of the bare 2 bladed Savonius VAWT at 343.70 rpm and on-coming wind speed of 7.5 m/s

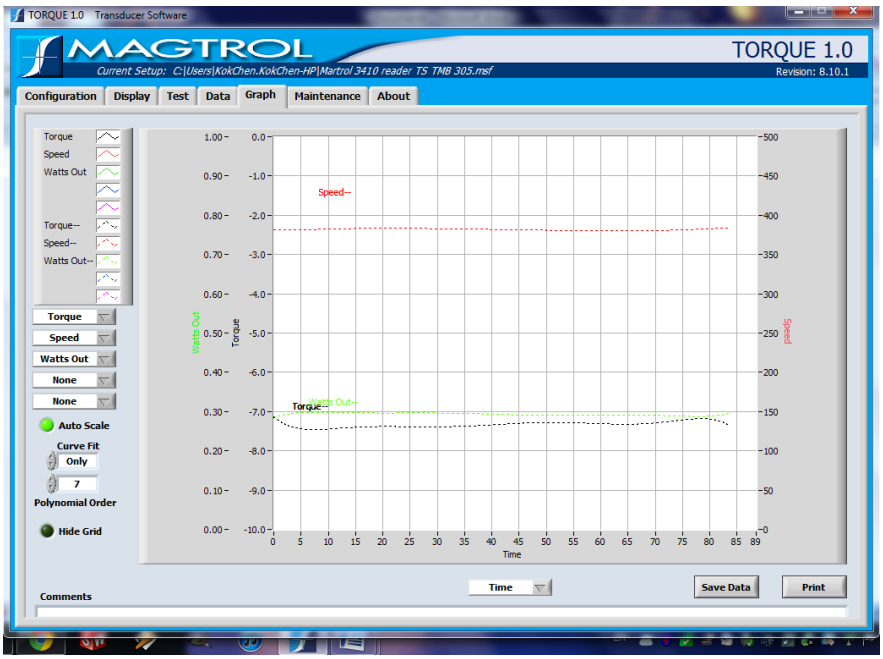

Figure C21: Print screen of the transient torque and power value of the bare 2 bladed Savonius VAWT at 382.00 rpm and on-coming wind speed of 7.5 m/s

APPENDIX D

The bearing friction calculation is based on the SKF model which enables an accurate of the frictional moment generated in SKF rolling bearings according to the equation,

$$\tau_{bearing} = \tau_{rr} + \tau_{sl} + \tau_{seal} + \tau_{drag}$$

The equation consists terms of (at right hand side) rolling friction moment, sliding frictional moment and drag losses in oil bath lubrication

- $\tau_{rr} = G_{rr}(vn)^{0.6}$, rolling friction moment [Nmm]

where

G_{rr} = a variable that depends on

  - The bearing type
  - The bearing mean diameter $d_{m_{bearing}} = 0.5(d + D)$, where d and D could be obtain via SKF website or handbook
  - The radial load F_r [N]
  - The axial load F_a [N],

n = rotational speed [r/min],

v = kinematic viscosity of the lubricant at the operating temperature [mm^2/s] (for grease lubrication the base oil viscosity

- $\tau_{sl} = \mu_{sl} G_{sl}$, sliding frictional moment [Nmm]

where

G_{sl} = a variable that depends on

  - The bearing type

- The bearing mean diameter $d_{m_{bearing}} = 0.5(d + D)$, where d and D could be obtain via SKF website or handbook
- The radial load F_r [N]
- The axial load F_a [N],

μ_{sl} = sliding friction coefficient, which can be set to the value for full film applications, i.e.,

- 0.05 for lubrication with mineral oils
- 0.04 for lubrication with synthetic oils
- 0.1 for lubrication with transmission fluids
- For cylindrical roller bearing and tapered roller bearing , the coefficients value to be 0.02 and 0.002 respectively.

Equations for G_{sl} and geometry constants are read from the database when could be obtained from below link, (http://www.skf.com/skf/productcatalogue/calculationsFilter?newlink=1_0_1&action=Calc5&maincatalogue=1&lang=en)(Retrieved June 20, 2012)

- $\tau_{seal} = K_{s1} {d_s}^{\beta} + K_{s2}$, frictional moment of seals [Nmm]

where

K_{s1} = constant depending on the bearing type

K_{s2} = constant depending on the bearing type and seal type

d_s = seal counterface diameter [mm]

β = exponent depending on bearing and seal type

Values for constants K_{s1} and K_{s2}, shoulder diameter, d_s and exponent, β are read from the SKF, at below link, (http://www.skf.com/skf/productcatalogue/calculationsFilter?newlink=1_0_1&action=Calc5&maincatalogue=1&lang=en) (Retrieved June 20, 2012)

- τ_{drag}, drag losses

In oil bath lubrication, the bearing is partially, or in special situations, completely submerged. Under these conditions the size and geometry of the oil reservoir together with the oil level used can have a substantial impact on the bearing frictional moment. For a very large oil bath, disregarding any reservoir size interaction and any influence of other mechanical elements working close to the bearing, e.g. external oil agitation, gears or cams, the drag losses in a bearing as a function of the oil level in the reservoir can be approximated from the variable, V_m plotted as below Figure D1, as a function of the oil level H and the bearing mean diameter.

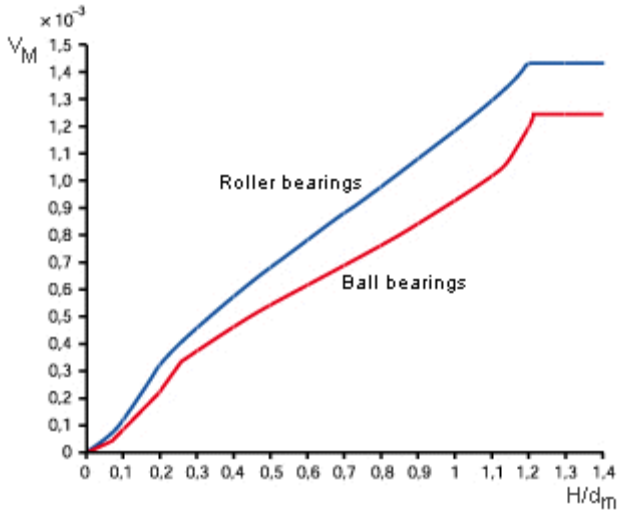

Figure D1: Variable, V_m versus oil level H and the bearing mean diameter

Figure D1 can be applied for bearing speeds up to the reference speed of the bearing. At higher speeds and high oil levels other effects might have an important influence in the results.

The variable, V_m in Figure D1 is related to the frictional moment of drag losses for ball bearings by

$$\tau_{drag_{ball\ bearing}} = V_m K_{ball} {d_m}^5 n^2 \text{ , [Nmm]}$$

$$\tau_{drag_{roller\ bearing}} = 10 V_m K_{roll} B {d_m}^4 n^2 \text{ , [Nmm]}$$

where

V_m = variable as a function of the oil level according to Figure D1

$K_{ball} = (i_{rw} K_Z (D + d))/(D - d)10^{-12}$, ball bearing related constant

$K_{roll} = (K_L K_Z (D + d)/(D - d)10^{-12}$, roller bearing related constant

d_m = bearing mean diameter [mm]

B = bearing width [mm], T for tapered roller bearings, H for thrust bearings

n = rotational speed [r/min]

i_{rw} = the number of ball rows

K_Z = bearing type related geometry constant

K_L = roller bearing type related geometry constant

d = bearing bore diameter [mm]

D = bearing outside diameter [mm]

http://www.skf.com/portal/skf/home/products?maincatalogue=1&lang=en&newlink=1_0_38a (Retrieved June 20, 2012)

One can find that the calculation of the frictional lost of bearing is tedious, especially at various RPM parameters. For the sake of convenience, SKF prepares a webpage for calculation by keying the parameters such as bearing type, rotational speed,

viscosity of the lubrication oil, radial load of the bearing, axial load of the bearing and etc. The print screen of the webpage was shown as Figure D2.

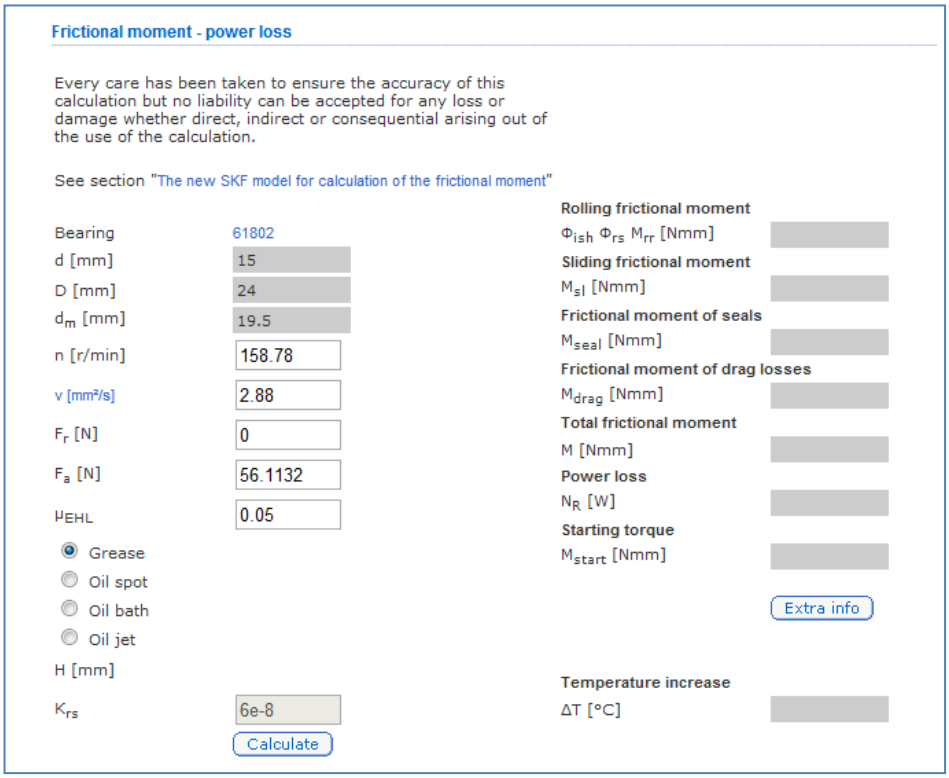

Figure D2: Print screen of SKF's webpage for bearing total frictional moment/ torque lost calculation

APPENDIX E

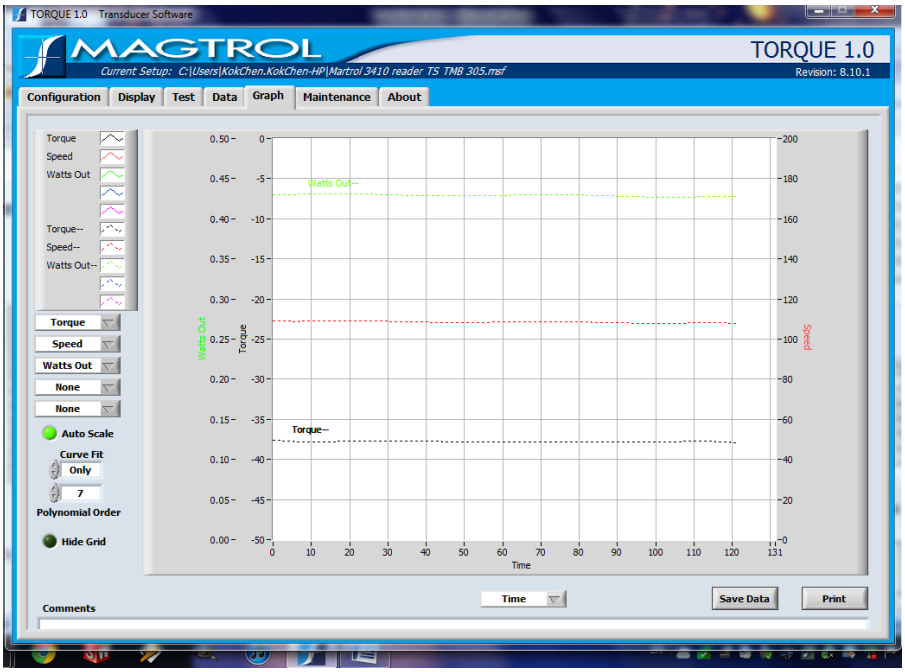

Figure E1: Print screen of the transient torque and power value of the 2 bladed Savonius VAWT with the ODGV at 108.47 rpm and on-coming wind speed of 3 m/s

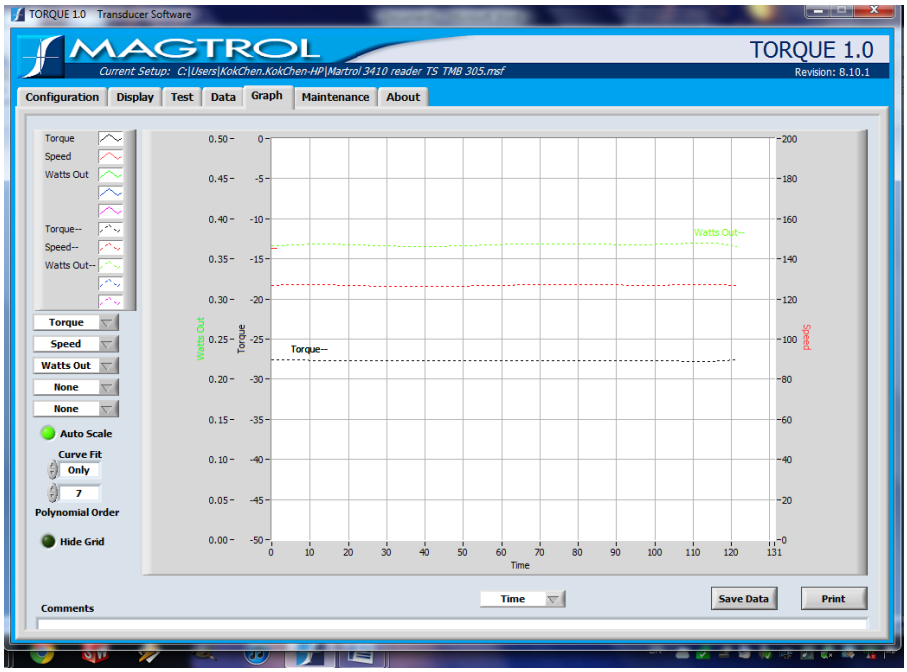

Figure E2: Print screen of the transient torque and power value of the 2 bladed Savonius VAWT with the ODGV at 126.80 rpm and on-coming wind speed of 3 m/s

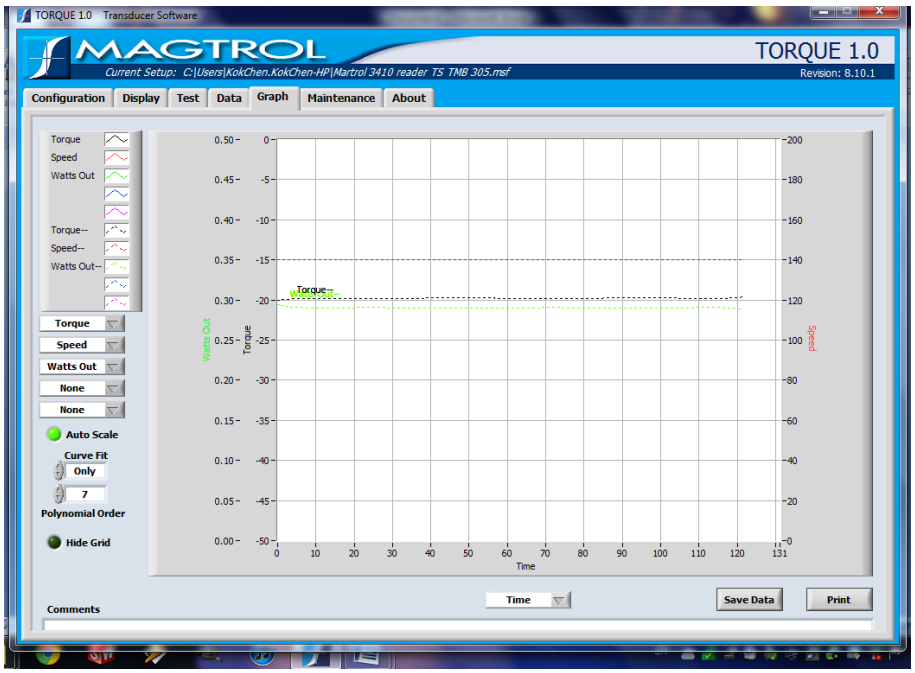

Figure E3: Print screen of the transient torque and power value of the 2 bladed Savonius VAWT with the ODGV at 140.00 rpm and on-coming wind speed of 3 m/s

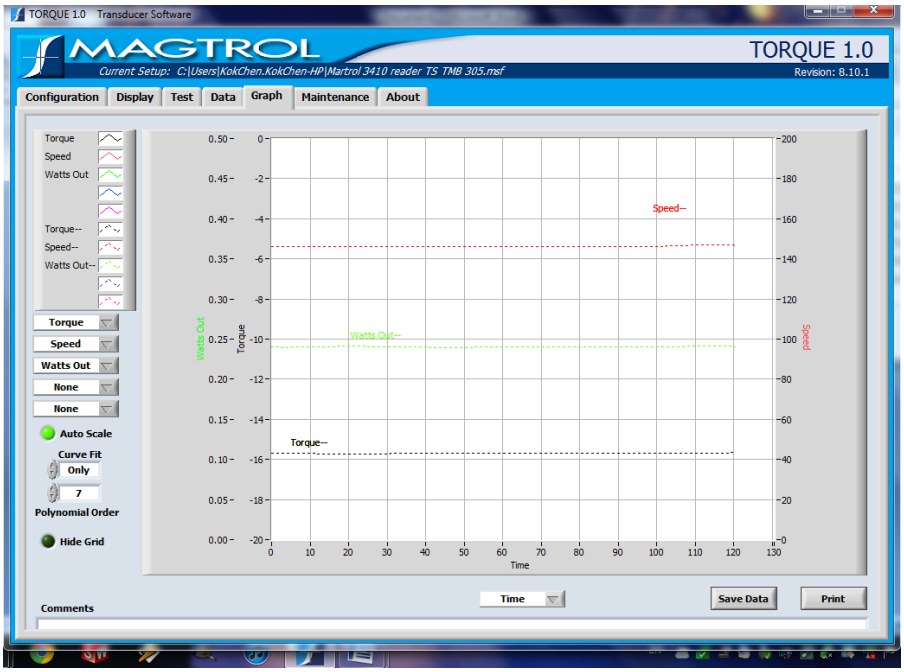

Figure E4: Print screen of the transient torque and power value of the 2 bladed Savonius VAWT with the ODGV at 146.20 rpm and on-coming wind speed of 3 m/s

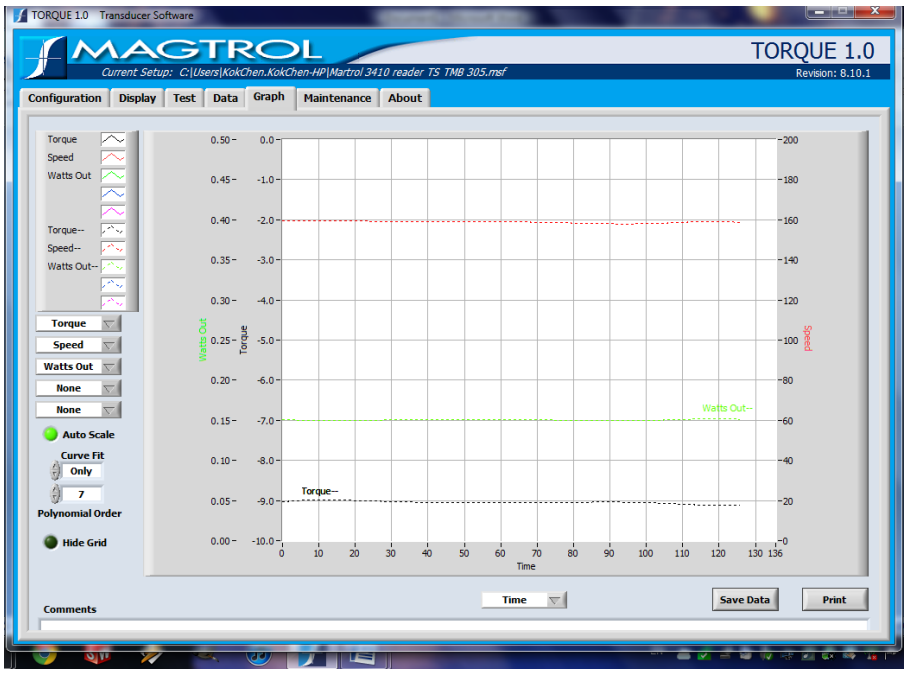

Figure E5: Print screen of the transient torque and power value of the 2 bladed Savonius VAWT with the ODGV at 158.90 rpm and on-coming wind speed of 3 m/s

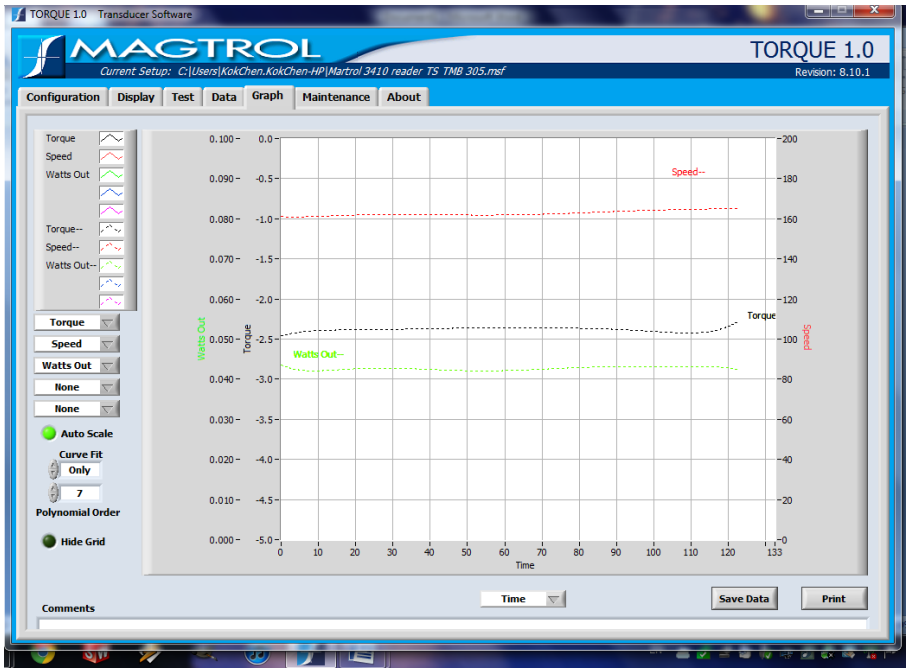

Figure E6: Print screen of the transient torque and power value of the 2 bladed Savonius VAWT with the ODGV at 162.70 rpm and on-coming wind speed of 3 m/s

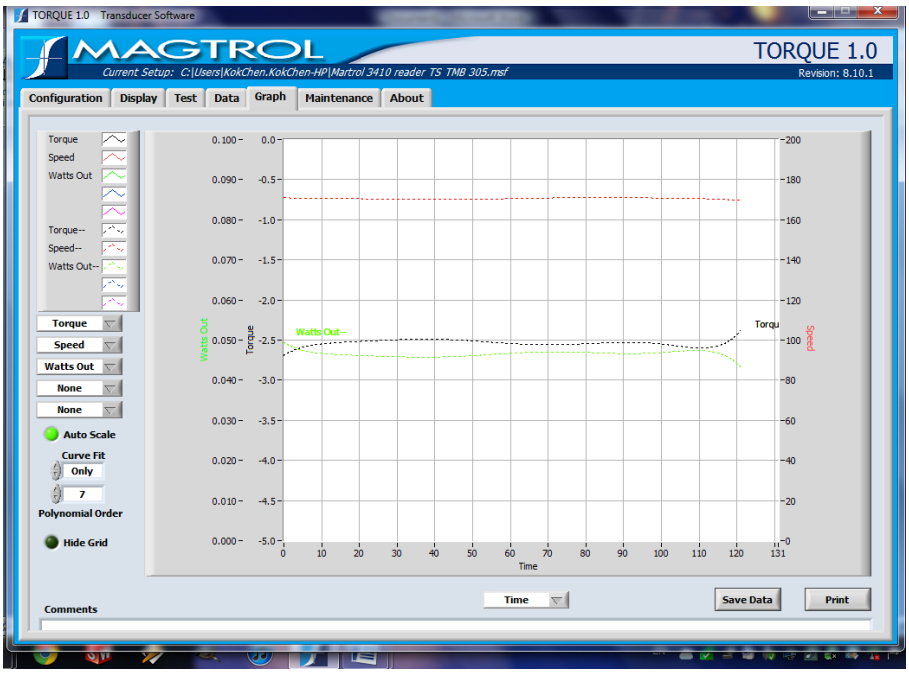

Figure E7: Print screen of the transient torque and power value of the 2 bladed Savonius VAWT with the ODGV at 170.60 rpm and on-coming wind speed of 3 m/s

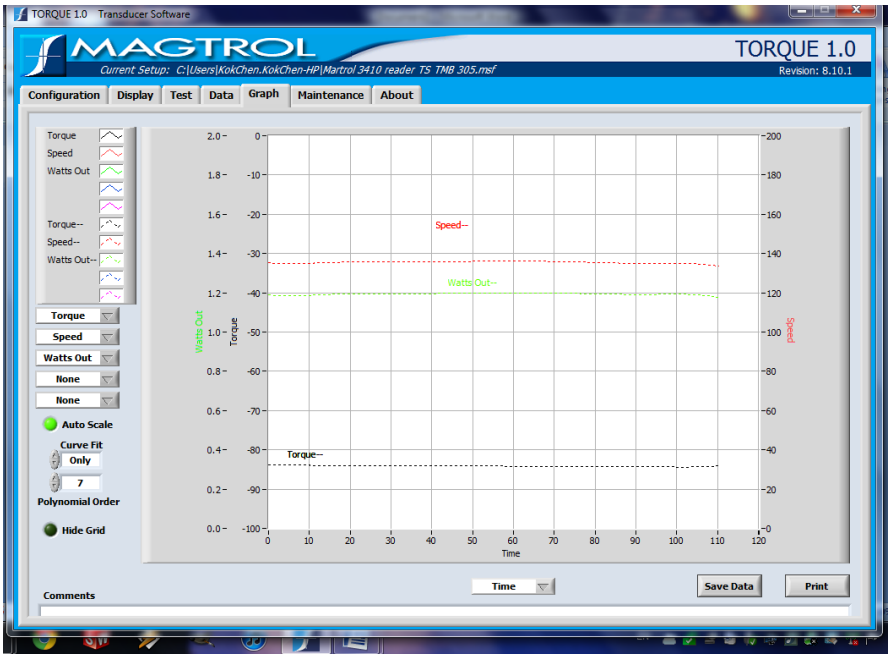

Figure E8: Print screen of the transient torque and power value of the 2 bladed Savonius VAWT with the ODGV at 135.50 rpm and on-coming wind speed of 4.5 m/s

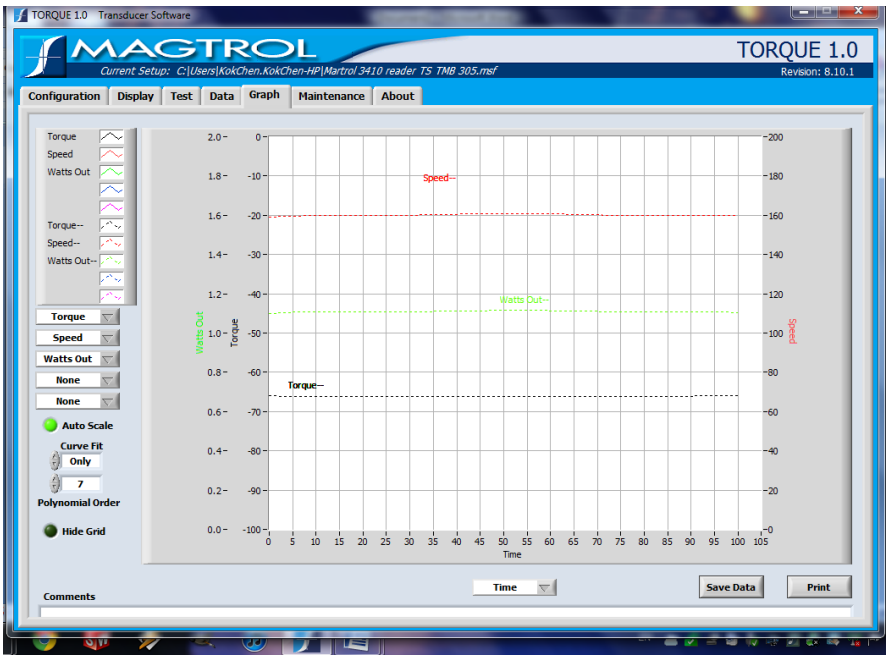

Figure E9: Print screen of the transient torque and power value of the 2 bladed Savonius VAWT with the ODGV at 160.10 rpm and on-coming wind speed of 4.5 m/s

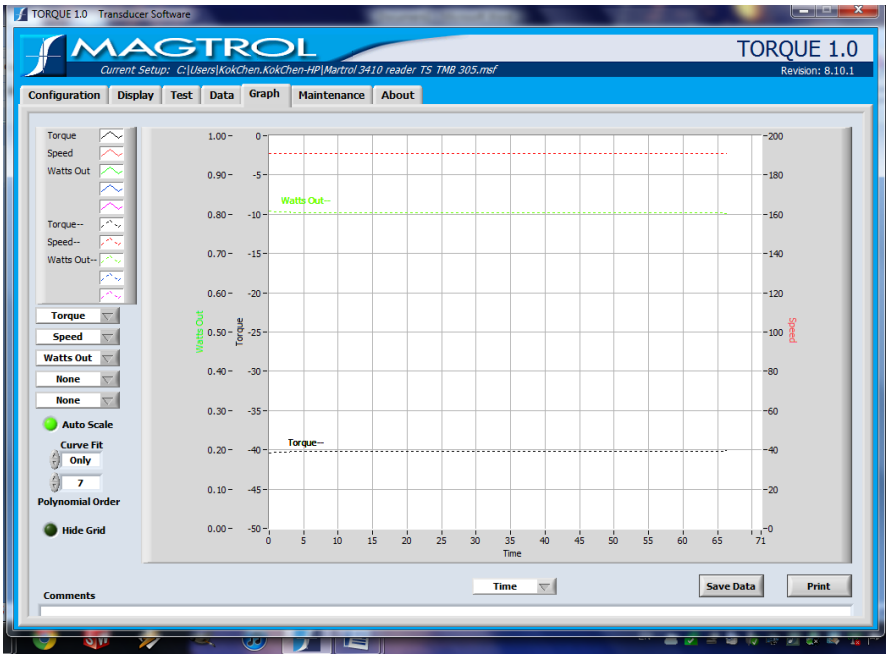

Figure E10: Print screen of the transient torque and power value of the 2 bladed Savonius VAWT with the ODGV at 191.00 rpm and on-coming wind speed of 4.5 m/s

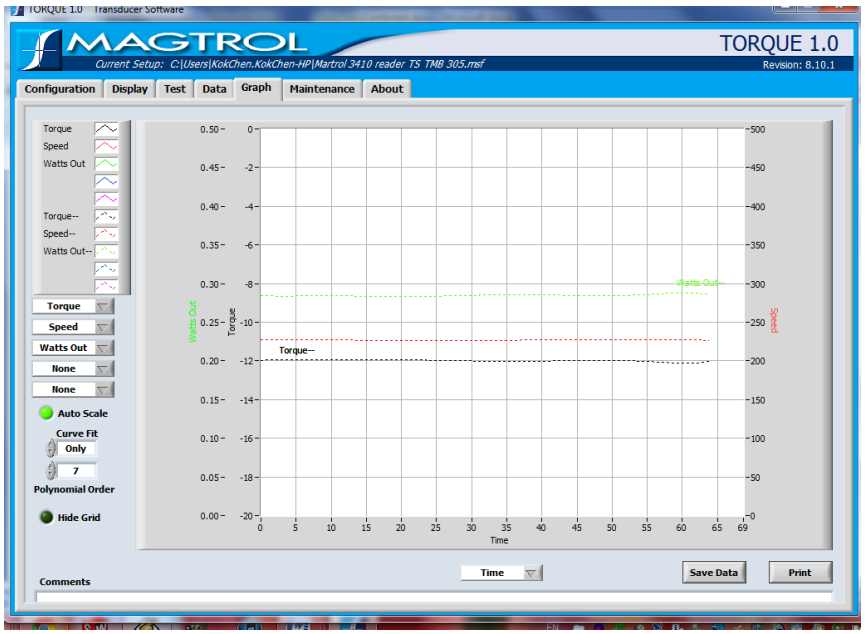

Figure E11: Print screen of the transient torque and power value of the 2 bladed

Savonius VAWT with the ODGV at 226.80 rpm and on-coming wind speed of 4.5 m/s

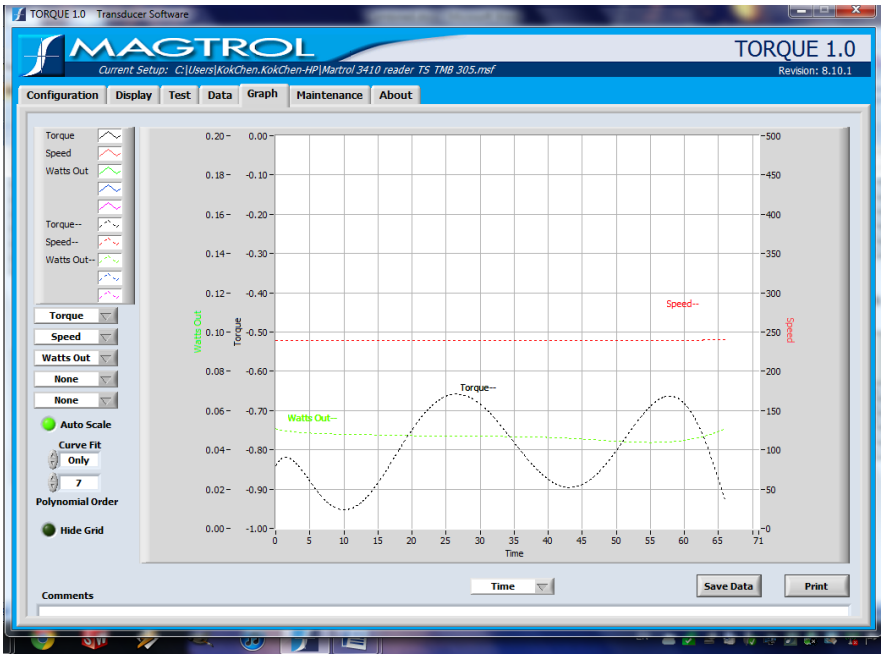

Figure E12: Print screen of the transient torque and power value of the 2 bladed

Savonius VAWT with the ODGV at 239.20 rpm and on-coming wind speed of 4.5 m/s

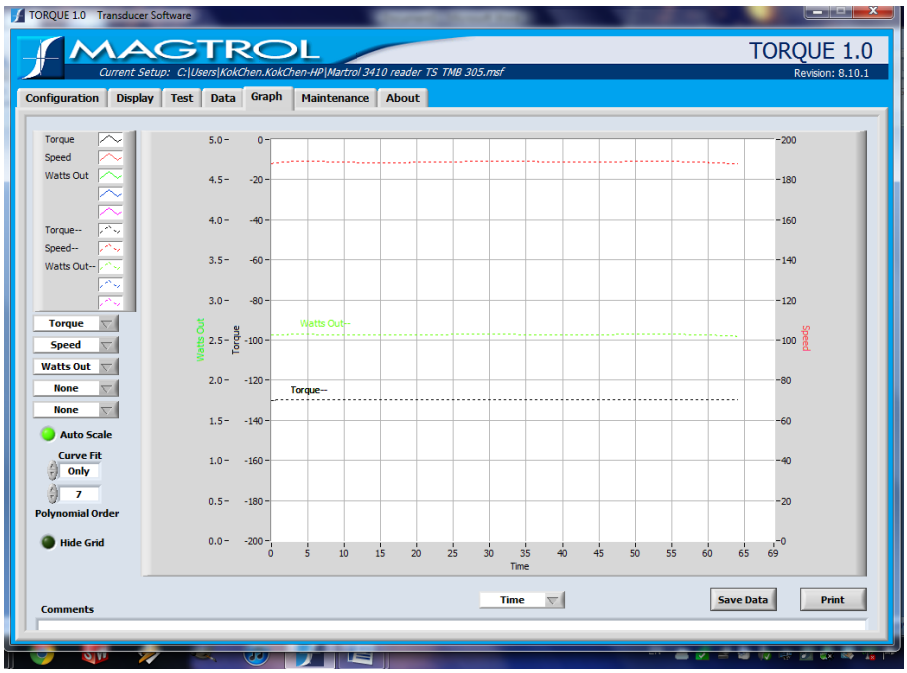

Figure E13: Print screen of the transient torque and power value of the 2 bladed

Savonius VAWT with the ODGV at 188.80 rpm and on-coming wind speed of 6 m/s

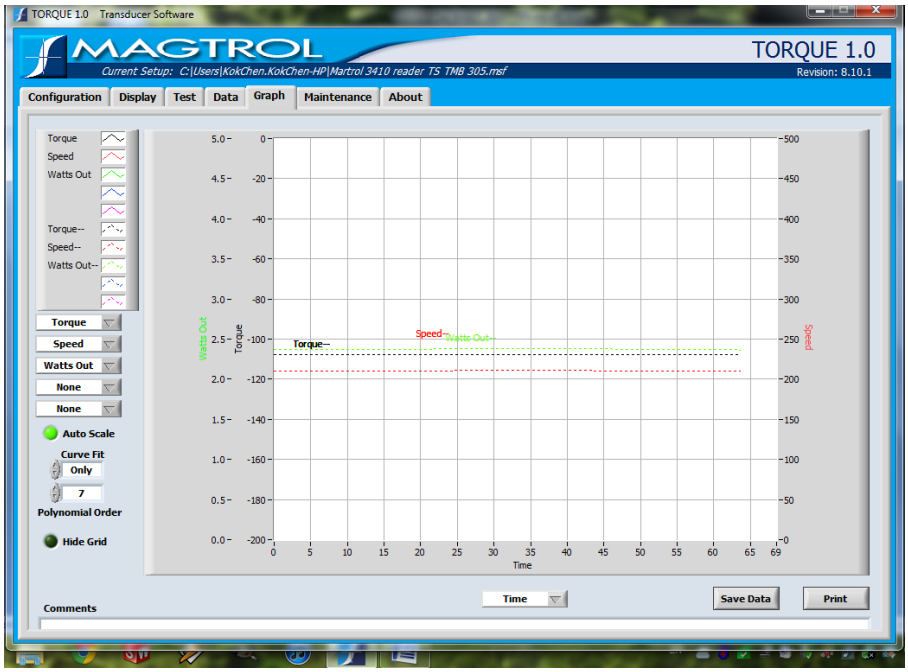

Figure E14: Print screen of the transient torque and power value of the 2 bladed

Savonius VAWT with the ODGV at 210.45 rpm and on-coming wind speed of 6 m/s

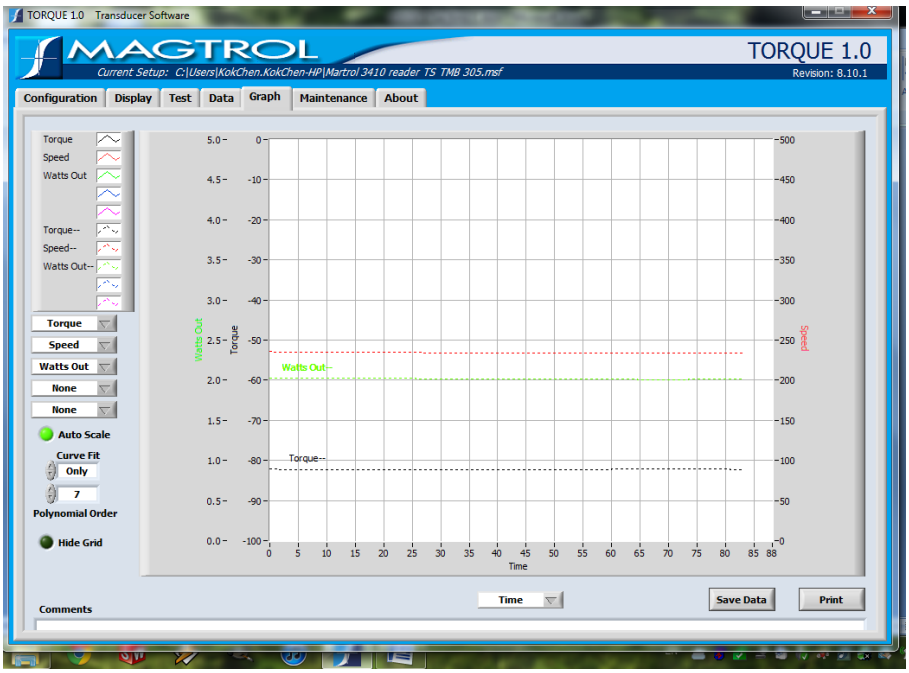

Figure E15: Print screen of the transient torque and power value of the 2 bladed

Savonius VAWT with the ODGV at 234.18 rpm and on-coming wind speed of 6 m/s

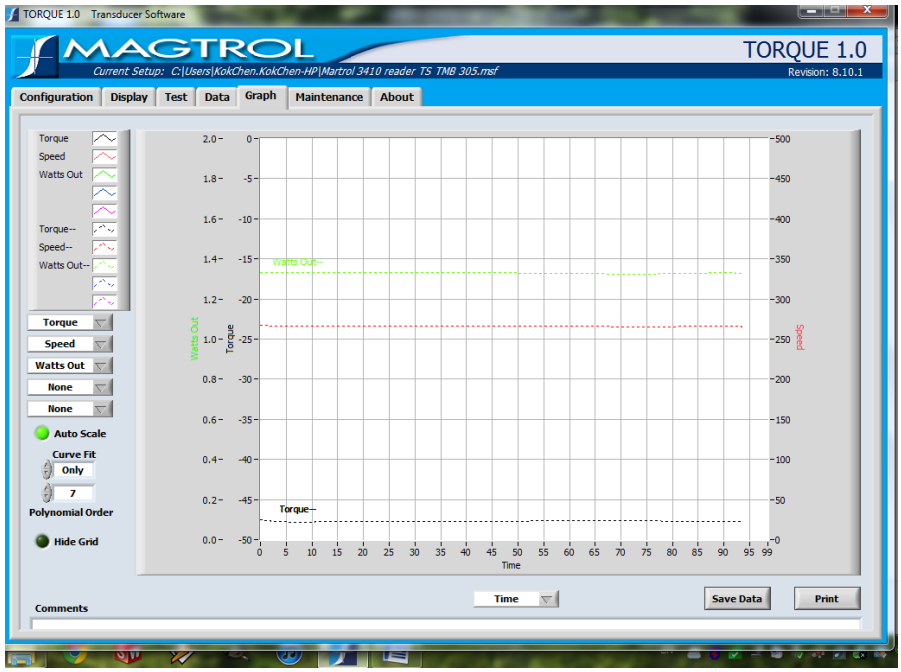

Figure E16: Print screen of the transient torque and power value of the 2 bladed

Savonius VAWT with the ODGV at 266.13 rpm and on-coming wind speed of 6 m/s

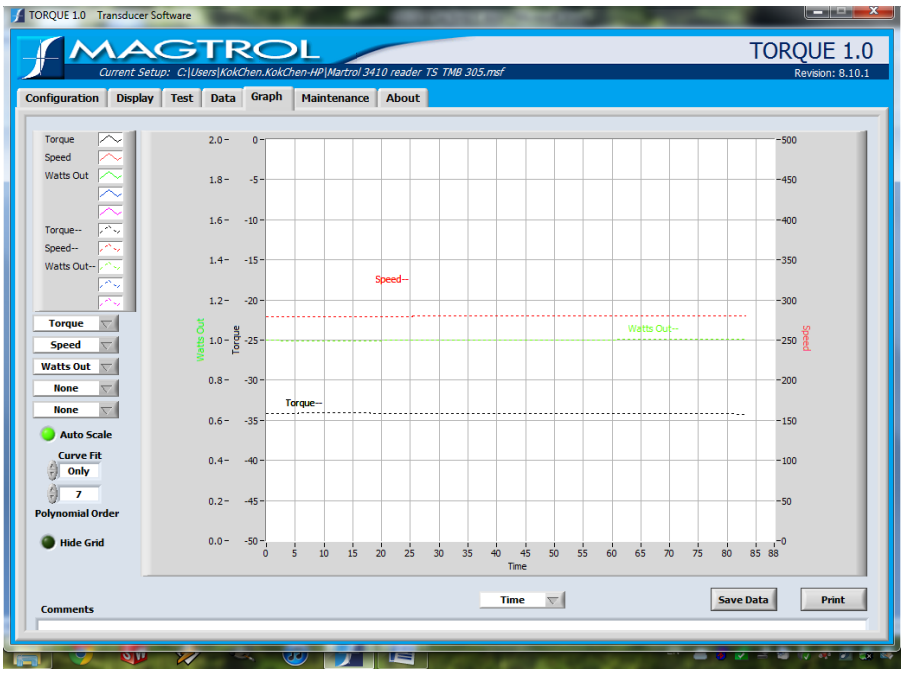

Figure E17: Print screen of the transient torque and power value of the 2 bladed

Savonius VAWT with the ODGV at 279.80 rpm and on-coming wind speed of 6 m/s

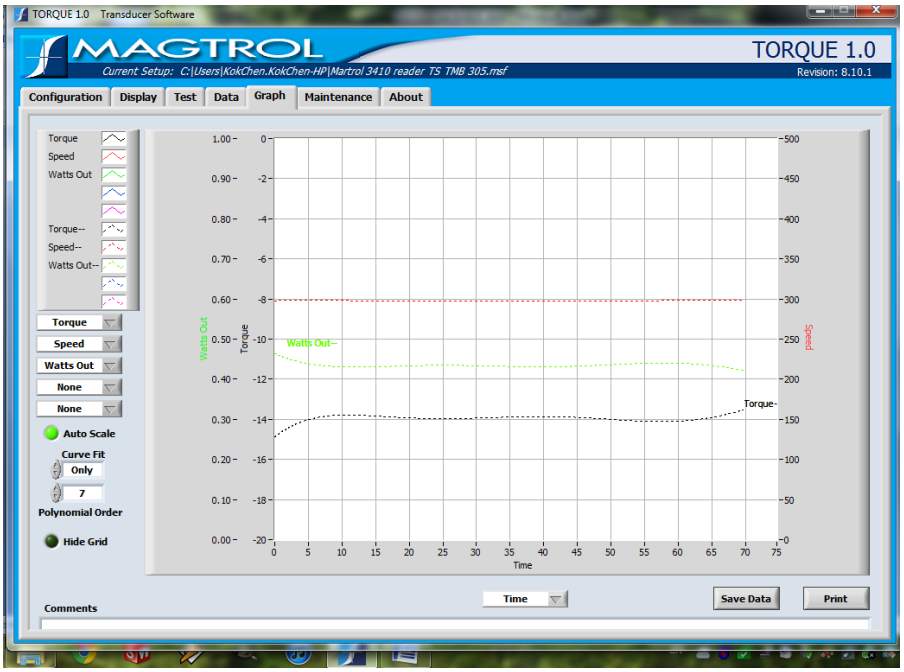

Figure E18: Print screen of the transient torque and power value of the 2 bladed

Savonius VAWT with the ODGV at 297.60 rpm and on-coming wind speed of 6 m/s

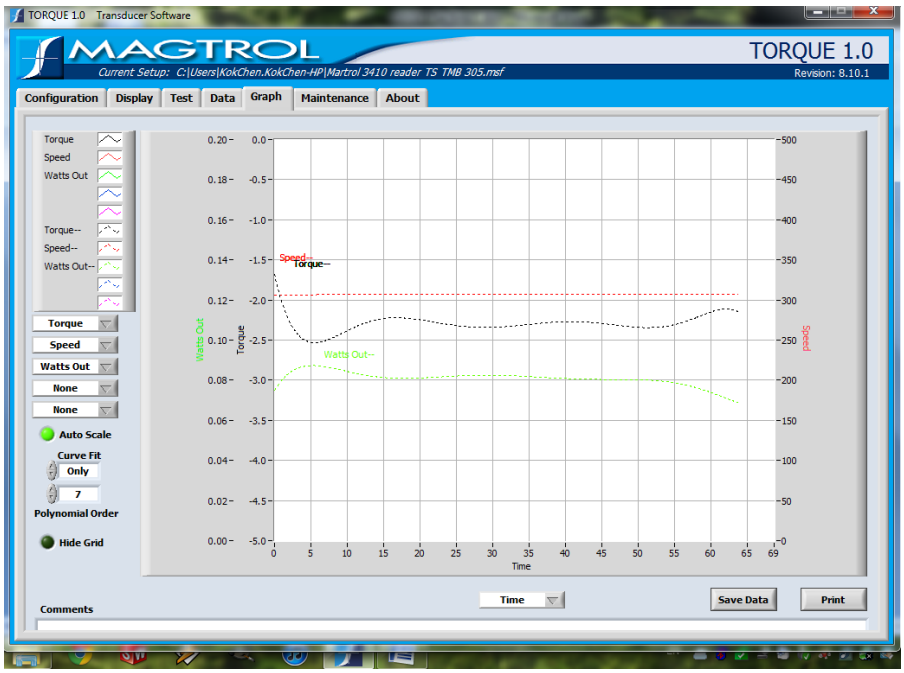

Figure E19: Print screen of the transient torque and power value of the 2 bladed

Savonius VAWT with the ODGV at 307.00 rpm and on-coming wind speed of 6 m/s

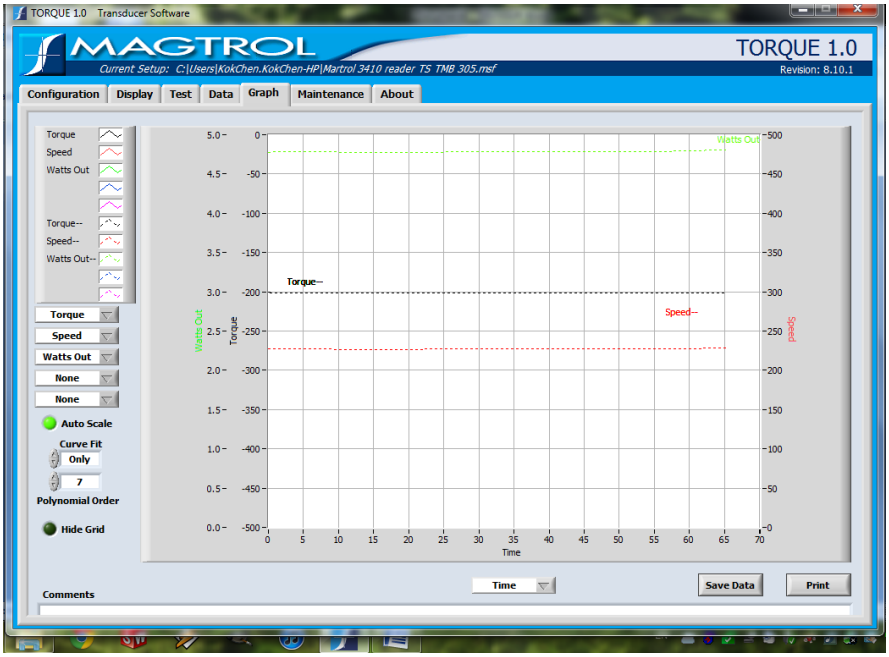

Figure E20: Print screen of the transient torque and power value of the 2 bladed

Savonius VAWT with the ODGV at 227.14 rpm and on-coming wind speed of 7.5 m/s

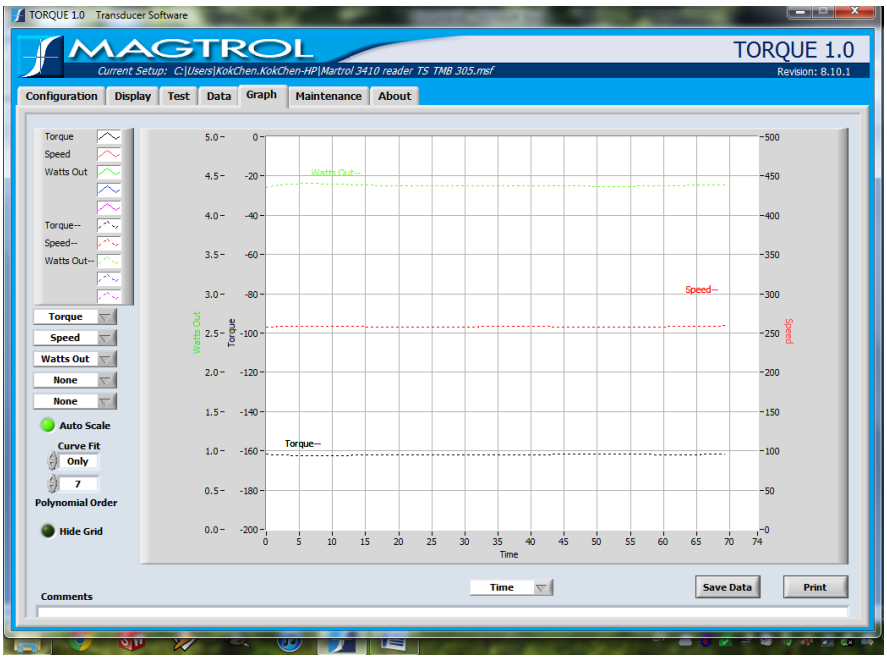

Figure E21: Print screen of the transient torque and power value of the 2 bladed

Savonius VAWT with the ODGV at 258.16 rpm and on-coming wind speed of 7.5 m/s

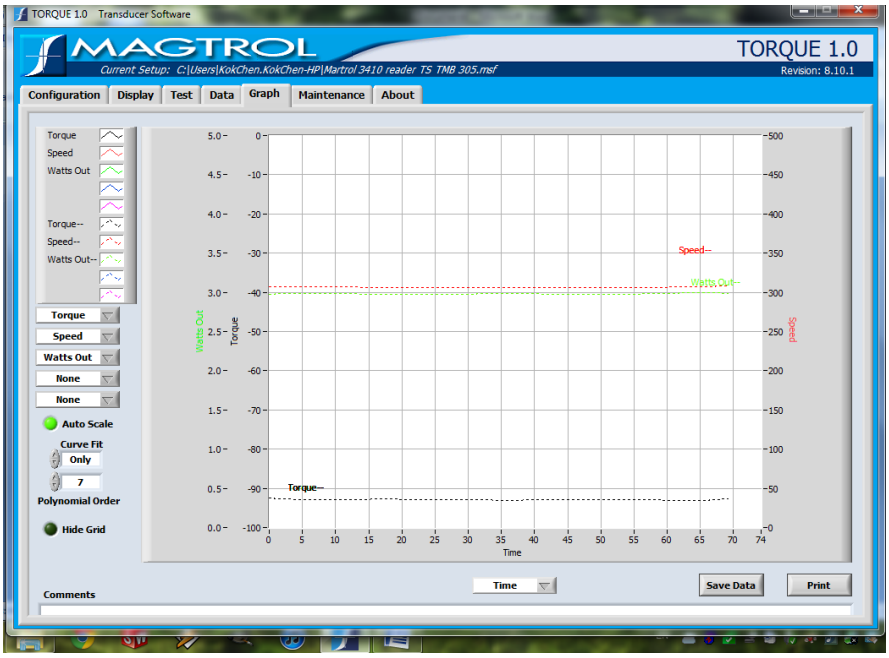

Figure E22: Print screen of the transient torque and power value of the 2 bladed

Savonius VAWT with the ODGV at 306.47 rpm and on-coming wind speed of 7.5 m/s

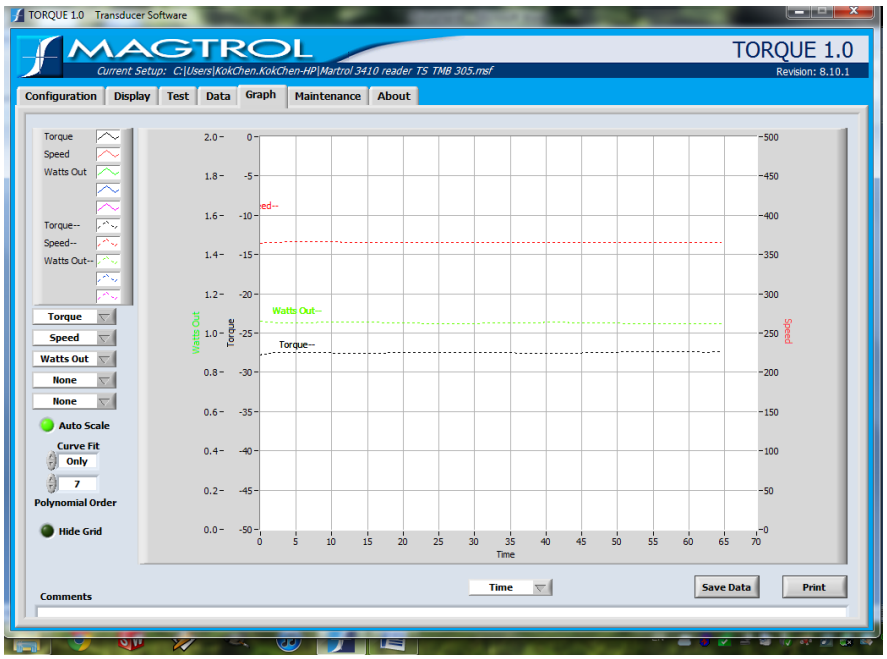

Figure E23: Print screen of the transient torque and power value of the 2 bladed

Savonius VAWT with the ODGV at 365.32 rpm and on-coming wind speed of 7.5 m/s

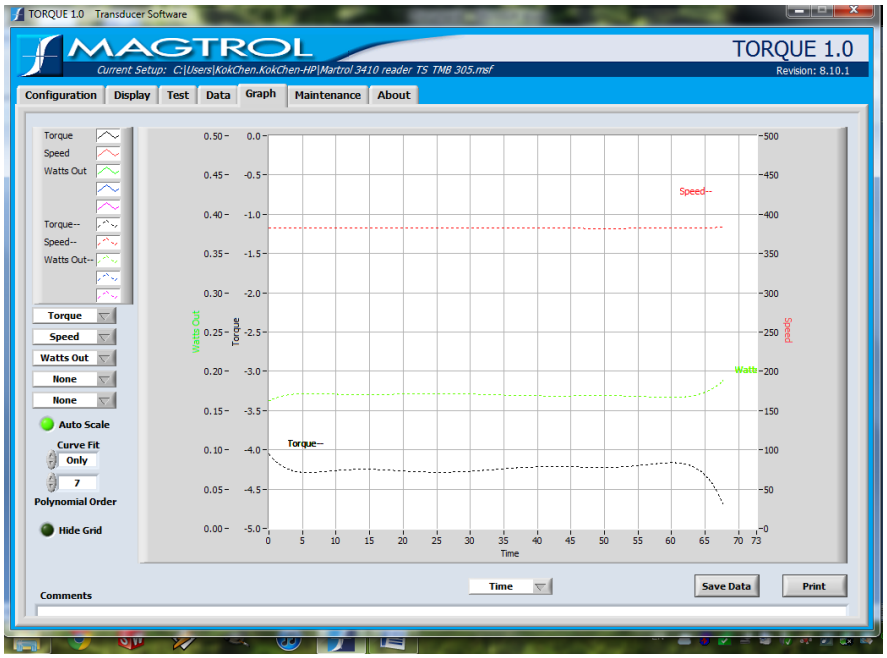

Figure E24: Print screen of the transient torque and power value of the 2 bladed

Savonius VAWT with the ODGV at 382.37 rpm and on-coming wind speed of 7.5 m/s